Cochlear Morphology and Sound-Induced Motion of the Apical Mammalian Inner Ear

by

Scott Lawrence Page

Submitted to the Department of Electrical Engineering and Computer Science
in partial fulfillment of the requirements for the degree of

Doctor of Philosophy

at the

MASSACHUSETTS INSTITUTE OF TECHNOLOGY

February 2016

Signature redacted

Author .....
Department of Electrical Engineering and Computer Science
January 29, 2016

Certified by..... Signature redacted .....
Dennis M. Freeman
Professor
Thesis Supervisor

Accepted by..... Signature redacted .....
Leslie A. Kolodziejski
Chairman, Department Committee on Graduate Theses

Cochlear Morphology and Sound-Induced Motion of the Apical Mammalian Inner Ear

by

Scott Lawrence Page

Submitted to the Department of Electrical Engineering and Computer Science
on January 29, 2016, in partial fulfillment of the
requirements for the degree of
Doctor of Philosophy

Abstract

Extraordinary sensitivity, frequency selectivity, and dynamic range are hallmarks of mammalian hearing. While a variety of cellular and molecular mechanisms are known to be critical to these properties, how the cellular and molecular mechanisms interact to generate the remarkable properties remains unclear. Direct observations of these interacts has proved to be difficult, in large part because the inner ear is fragile and has been difficult to probe with conventional measurement technologies. We have developed an Optical Coherence Tomography (OCT) system to use light to probe both the structure and mechanical responses of the inner ear to sound stimulation. The technique takes advantage of the interference of low coherence sources of light to detect even weakly scattering tissues in the inner ear. By sensing Doppler shifts of light scattered off moving structures in the inner ear, the OCT system can also detect sound-induced motions of cochlear structures with sub-nanometer resolution. This thesis demonstrates the use of the OCT system to study the structure of the inner ears of mice, gerbils, and guinea pigs, as well as the acoustic response of the apical turn of *in vitro* and *in vivo* apical mammalian cochleae to low frequency (100 to 1000 Hz) sounds – frequencies that are critical to our understanding of speech.

Thesis Supervisor: Dennis M. Freeman
Title: Professor

Acknowledgments

I'd like to acknowledge my research group: Denny Freeman, Stan Hong, A. J. Aranyosi, Rooz Ghaffari, Shirin Farrahi, and Jon Sellon for all their help over the years. I'd also like to acknowledge Natasha Guha and Collin Kaufman for their help with experiments and experimental setup. Finally, I'd like to acknowledge everyone that has helped me along the way, including my friends and family.

Contents

List of Figures

List of Tables

Chapter 1

Introduction

The mammalian cochlea is a remarkable sensor. Using neural signals generated by the cochlea, humans can reliably detect sounds that cause motions of the stapes on the order of picometers — i.e., much smaller than the diameter of a hydrogen atom [114, 29]. The cochlea performs high-quality frequency analysis of low-level sounds: $Q_{10dB} > 600$ has been recorded for motions in the saline-filled cochlea of the bat [66, 99]. Furthermore, cochlear signal processing is profoundly nonlinear. One important nonlinearity is compression [101, 97, 20, 77, 88]. Humans detect sounds differing in intensity over a 120 decibel range. This range of intensities is compressed as it is encoded for neurons with considerably smaller (20-50 dB) dynamic ranges. It is now widely accepted that an active mechanical amplification process driven by outer hair cells (OHCs) underlies these remarkable properties.

While information on the cellular and molecular basis of hearing is increasing rapidly [9, 36, 103, 5, 56, 31], there has been substantially less progress in understanding how these components interoperate to generate the remarkable properties of hearing, particularly at low frequencies, which are most relevant to speech signal processing. Currently, there is significant debate about the prevalent modes of motion, compressive non-linearities and tuning responses from the low frequency apical region of the cochlea [19, 62, 121, 95, 5]. In addition to potentially resolving fundamental debates in cochlear mechanics, the cochlear apex also provides several experimental advantages as a measurement target: i) larger cellular structures (e.g. outer hair

cells) relative to the base; ii) larger acellular structures (e.g. tectorial membrane) relative to the base, and iii) time-based synchrony without low-pass filtering effects.

Cochlear mechanical and auditory nerve studies in chinchilla, guinea pig, and cat cochleae have yielded contradictory results with important clues about the presence of new modes of motion in the cochlear apex [19, 62, 121, 80, 70, 49, 48, 47]. Sound-induced motion measurements of the basilar membrane, tectorial membrane and reticular lamina in the apex may therefore further our understanding of low frequency signal processing of sound, and in particular, speech. In this thesis, we measure the cochlear morphology of *in vitro* cochlear preparations with Reissner's membrane intact, we measure absolute axial macromechanical motions of cochlear structures as a function of radial position in the *in vitro* and *in vivo* mammalian apex, and we assess relative cochlear motions of the basilar membrane, the tectorial membrane, and the reticular lamina as a function of intensity and frequency.

1.1 The mammalian cochlea

1.1.1 Cochlear anatomy

The mammalian cochlea, consists of three fluid-filled cavities: scala vestibuli, scala media, and scala tympani which spiral upward from the base of the cochlea toward the apex (figure 1-1). Scala vestibuli and scala tympani are filled with perilymph, a high Na^+, low K^+ fluid, while scala media is filled with endolymph, a high K^+, low Na^+ fluid. Scala media is isolated from scala vestibuli by Reissnert's membrane, a thin layer of epithelial cells, and from scala tympani by the reticular lamina, a system of tight junctions along a surface of the organ of Corti.

The organ of Corti (figure 1-1) consists of a variety of cells including inner and outer hair cells (which are separated radially by pillar cells), supporting cells, and the tunnel of Corti. Each inner and outer hair cell projects stereocilia into the subtectorial space, which lies above the reticular lamina and beneath the gelatinous, acellular structure called the tectorial membrane. There, it is generally believed that the stereocilia of the outer hair cells come into contact with the tectorial membrane (TM).

1.1.2 Effects of sound

Sound travels into the cochlea via the tympanic membrane (eardrum), which excites the three middle ear ossicles: the incus, malleus and stapes, located near the base of the cochlea. As the stapes is displaced, a traveling wave of pressure differentials between the scala vestibuli and scala tympani travels from the base of the cochlea towards the apex. This macromechanical pressure wave causes an axial displacement of the basilar membrane and organ of Corti, which is maximal toward the base for high frequency stimuli and toward the apex for low frequency stimuli (figure 1-1D). This displacement is thought to cause radial shearing of the hair bundles against the tectorial membrane, which allows transduction channels to open and current to flow from scala media to scala tympani via the outer hair cells.

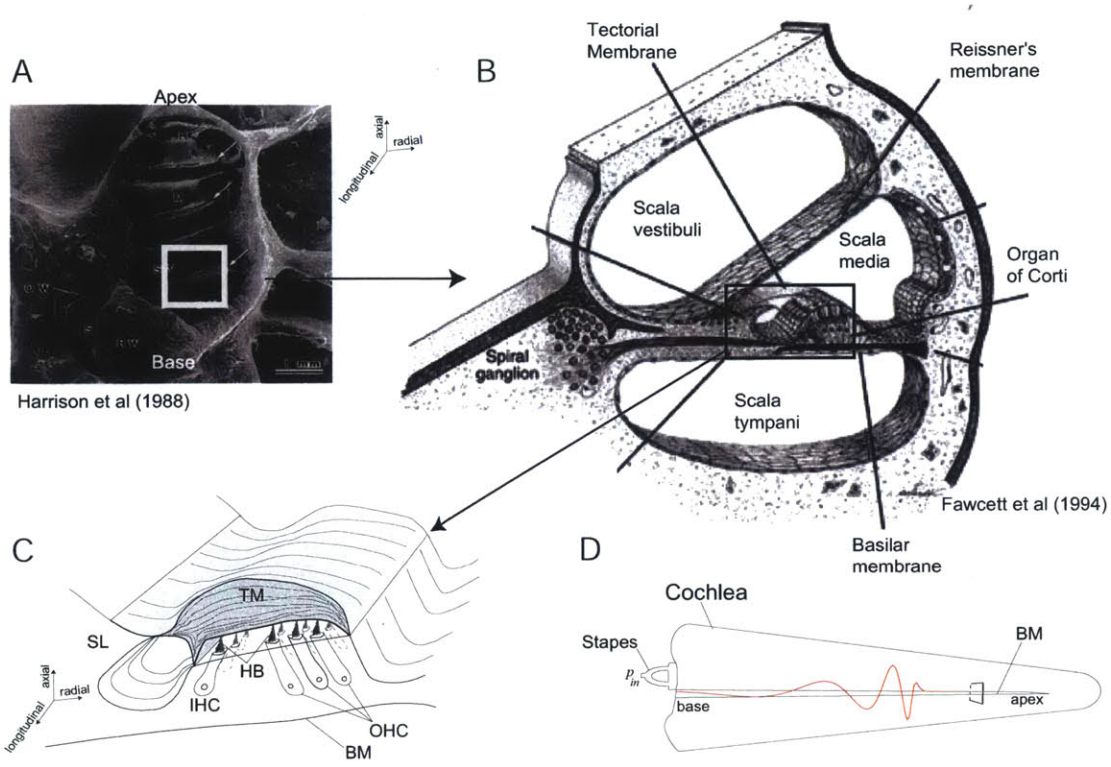

Figure 1-1: (A) The turns of the mammalian inner ear (Image from [51]) with the base and apex of the cochlea labeled. Reference directions are labeled. (B) Cross-section of a single turn [inset of (A)] with labeled fluid spaces: scala vestibuli, scala media, and scala tympani; and labeled structures: Reissner's membrane, the tectorial membrane, the organ of Corti, and the basilar membrane. (C) Drawing of a cross section of the organ of Corti [inset of (B)]. The spiral limbus (SL), tectorial membrane (TM), inner hair cell (IHC), hair bundles (HB), basilar membrane (BM), and outer hair cell (OHC) are labeled. (D) Stapes-induced basilar membrane traveling wave peaking axially near the apex along the stretched out length of the cochlea.

1.1.3 Cochlear amplification and sensitivity

Figure 1-2B illustrates a outer hair cell body with hair bundles protruding from the reticular lamina. Hair bundle deflection causes current from scala media to depolarize the outer hair cell. Outer hair cells respond to the change in transmembrane potential (V_M) by expanding and contracting in length (L) and diameter [9]. The changes in length are thought to contribute to sensitivity increases found in the base of living cochleae by exerting a force on the cochlear partition and causing the hair bundles to deflect even more.

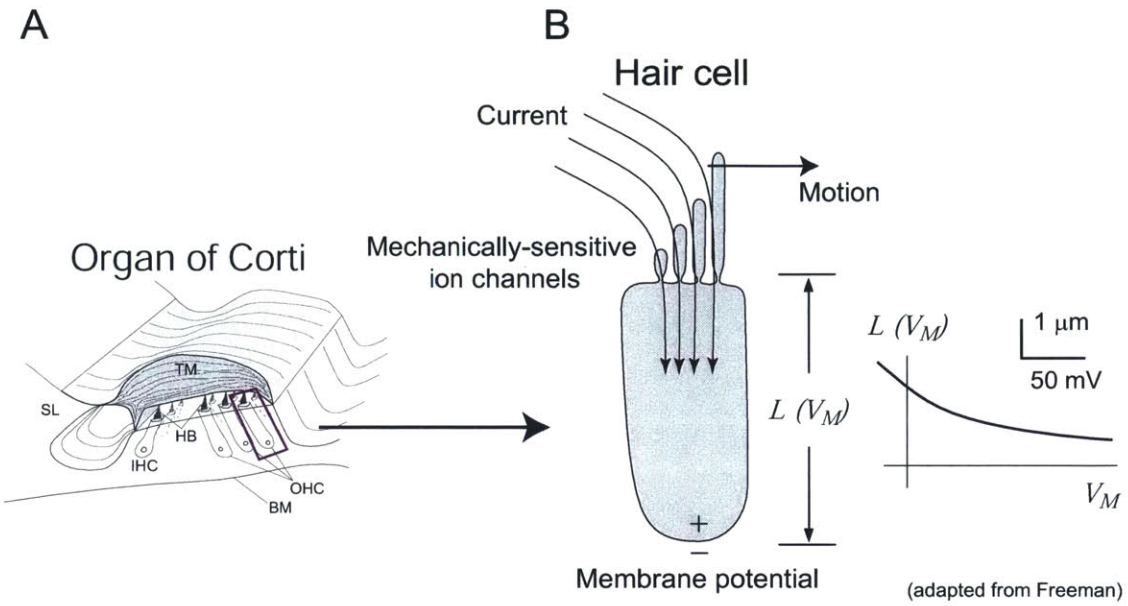

Figure 1-2: (A) Cross-section of the organ of Corti with inset of an outer hair cell (OHC). (B) The length (L) of an outer hair cell body is a function of its membrane potential (V_M). Hair bundle radial deflection causes currents from scala media to depolarize the cell causing an increase in V_M and a subsequent decrease, or contraction, in the length of the hair cell.

In the living cochlea, transduction currents are much larger than a passive cochlea due to factors such as an endocochlear potential. In living mammals, the endocochlear potential is maintained at ~80 millivolts through active processes, and exists in the endolymph filled scala media. Laser Doppler velocimetry experiments done by Ruggero and Rich [96] show that during furosemide administration, which causes a drop in endocochlear potential, the basilar membrane becomes much less sensitive and exhibits a linear input-output relationship in the base of the cochlea (figure 1-3). The apex (1000 Hz stimulus) was affected much less by the drop in endocochlear potential due to furosemide.

The effect of cochlear amplification can be seen by looking at basal sensitivity curves (figure 1-4A), which normalize displacement with that of the stimulus sound pressure. The cochlear base shows a high degree of nonlinear displacement relative to input sound pressure. Low sound pressure stimuli have a higher degree of displacement amplification relative to high sound pressure stimuli. In the apex, sensitivity

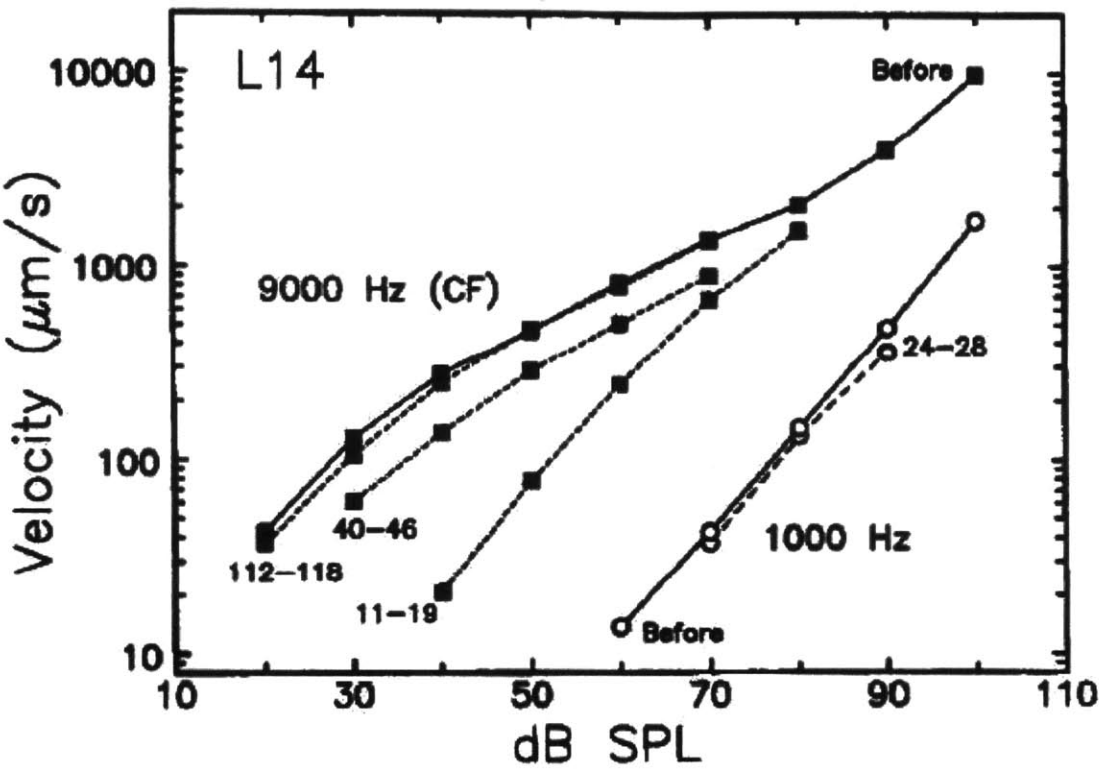

Figure 1-3: Input-output curves for the response of basilar membrane L 14 to tones immediately preceding (solid line) and following (broken lines) an intravenous 50-mg furosemide injection. Responses are shown for a CF tone (9 kHz, squares) and for a 1- kHz tone (circles). The abscissa indicates stimulus intensity (in dB SPL, i.e., referenced to 20 μPa), and the ordinate indicates peak basilar membrane velocity (in μm/sec). The time of data collection, in minutes relative to the furosemide injection, is indicated for each curve. Data were collected by means of laser velocimetry. (Figure and caption from [96])

curves at low characteristic frequencies appear to be linear in comparison with the base.

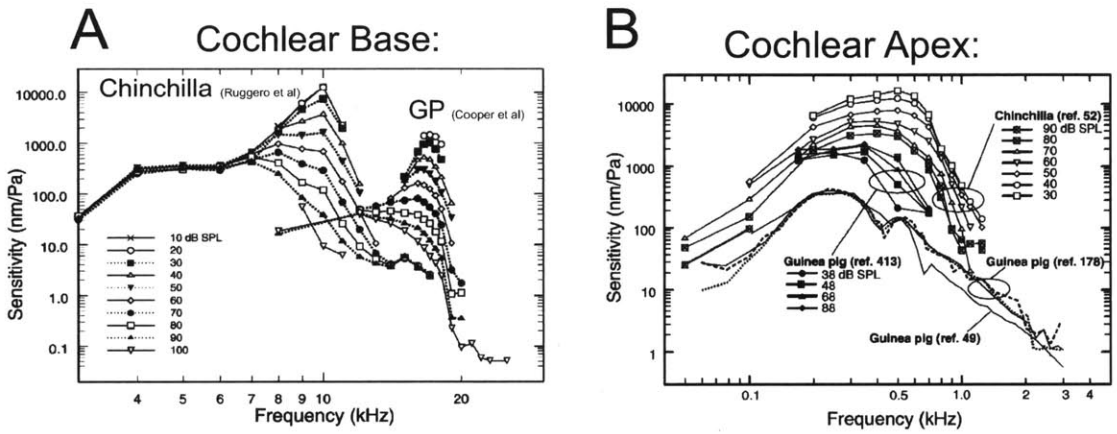

Figure 1-4: (A) Basal sensitivity from the chinchilla [98] and guinea pig [20] as a function of input sound pressure level and frequency. (B) Apical sensitivity of the reticular lamina as a function of input sound pressure level and frequency. Guinea pig (ref. 413) is reference [121] measures the organ of Corti through Reissner's membrane with LDV. Guinea pig (ref. 49) is reference [19], which measures with LDV. Guinea pig (ref. 178) is [63], which measures the reticular lamina with confocal interferometry. (Figures from [95]).

Chapter 2

DOCM/DOCT Methodology

This section is adapted from a paper presented at the Mechanics of Hearing conference in 2015 [83]. Additional system information is available at the following reference [52].

2.1 Introduction

Despite extensive progress in measurements of cochlear mechanics over the past several decades, there are still basic phenomena that are not well understood. One reason for this lack of data has been due to the difficulties in measuring motions of structures within the cochlear partition of intact systems. The history of cochlear mechanics studies shows that new measurement tools lead directly to new discoveries about cochlear function. Stroboscopic microscopy techniques pioneered by von Békésy demonstrated the mechanical frequency separation introduced by the cochlear traveling wave [114]. The later application of Mössbauer methods [90, 104], and subsequent laser Doppler vibrometry (LDV) methods [81, 96], permitted measurements of the sharply-tuned, labile motions of basilar membranes in living cochleae [95]. LDV techniques have further demonstrated the spatial extent of traveling waves on the basilar membrane in living cochleae [101, 89, 95]. Video microscopy and related gradient methods have allowed the observation of three-dimensional motions of multiple cochlear structures [24, 58]. These techniques have been successful in demonstrating the relative motions of structures in the mammalian cochlea. Both LDV and video

microscopy methods are now widely used and continue to provide valuable insights into cochlear function.

Despite their successes, current methods based on LDV and video microscopy have important limitations affecting their ability to study the cochlea as a system. For example, in video microscopy both lateral and axial resolutions are limited by the size of the opening made in the wall of the cochlea. To date, it has been impossible to obtain wide access (for high resolution) without significantly reducing the sensitivity of the cochlea. In LDV, axial resolution is typically limited to single highly reflective targets (either naturally occurring or artificially placed), which greatly complicates characterization of cellular processes in the organ of Corti (figure 2-1A). However, confocal LDV systems reduce the need for an artificially placed reflective target, as the axial depth from which light is collected is confined [80].

As with optical coherence tomography (OCT), images constructed via Doppler optical coherence microscopy (DOCM) and Doppler optical coherence tomography (DOCT) use optical range information and can be acquired using both high (DOCM) and low (DOCT) numerical aperture access [82]. These systems utilize the Doppler shift caused by the motion of scattering structures to measure displacement as a function of depth into the tissue. This novel combination of LDV and OCT measures sub-nanometer displacements of weakly scattering structures within the cochlear partition using fiber-based gradient index (GRIN) lenses, air objectives, and water objectives [117, 118, 52, 16, 13, 37].

2.2 DOCM/DOCT

LDV is built on the principle of the Michelson interferometer (figure 2-1B). Reflected light scattered from a coherent beam incident upon a sample is mixed with a reference beam to produce an interference pattern which can be measured at a photodetector or at a spatial plane. The detected signal consists of constructive and deconstructive interference. With a coherent source, the interferometric pattern sums light scattered from multiple depths (figure 2-1C). Reflective beads are thus typically used as targets

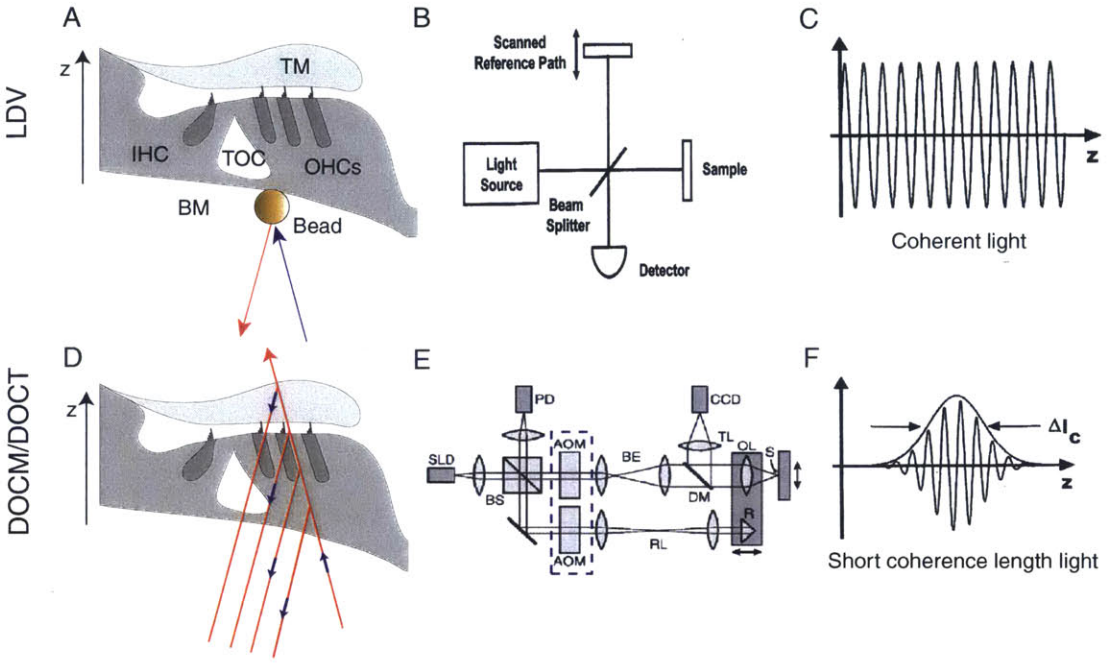

Figure 2-1: Comparison of LDV (A-C) and DOCT/DOCM (D-F) image and motion measurement techniques. (A) In LDV, the target is illuminated with light from a laser source. A reflective bead is often used to ensure a single point of reflection. (B) Schematic diagram of a Michelson interferometry setup showing the source split into a sample and reference path. Motions of the target modulate the optical path length and are measured by recombining the backscattered light with light from a reference path. (C) Interference pattern as a function of axial position (z) for a coherent light source, commonly used in LDV. Abbreviations: IHC = inner hair cell, TM = tectorial membrane, TOC = tunnel of Corti, OHCs = outer hair cells, BM = basilar membrane. (D) In DOCM/DOCT, light with a short coherence length is used to distinguish reflections from different optical depths. This technique renders a cross-sectional image of all visible structures, including cellular and acellular structures. (E) Schematic diagram of heterodyne (dashed box) DOCM/DOCT systems. (F) Interference as a function of the difference in optical path length (z) for a low coherence light source, commonly used in DOCT/DOCM. Δl_c represents the full width at half maximum (FWHM) of the interference signal and defines the coherence gate. Abbreviations: SLD = super luminescent diode, BS = beam splitter, PD = photodetector, AOM = acousto-optic modulator, BE = beam expander, RL = relay lens, DM = dichroic mirror, TL = tube lens, CCD = charge-coupled device, OL = objective lens, R = retroreflector, S = sample.

to isolate the motion measurement to a specific plane.

The DOCM/DOCT system, previously described by Hong, et al. [52], uses a low coherence source to optically section tissue (figure 2-1D) and is based on a Michelson interferometer in a double-pass configuration (figure 2-1E). The source has a center wavelength (λ_0) of 841 nm and a bandwidth ($\Delta\lambda$) of 47.8 nm. Acousto-optic modulators (AOMs) modulate the sample path at 80 MHz and the reference path at 80.25 MHz generating a 500 kHz heterodyne signal which allows for directional phase discrimination. DOCT and DOCM utilize a low coherence source to limit constructive interference to a small matched path length, typically less than 20 μm. An ideal low coherence source with a Gaussian spectrum yields an axial coherence gate (Δl_c), which is defined as the full width at half maximum (FWHM) of the interferometric signal (figure 2-1F), and described by the following:

$$\Delta l_c = \frac{2ln(2)}{\pi} \frac{{\lambda_0}^2}{\Delta\lambda} \tag{2.1}$$

The coherence gate can be used to optically section throughout tissue. Center frequencies of low coherence sources typically range from 800 nm to 1600 nm, while source bandwidth varies from approximately 20 nm to 300 nm.

DOCT utilizes a small numerical aperture (NA) objective or fiber-based GRIN lens to increase the depth of focus, while using the coherence gate to optically section (figure 2-2A). Scattered light is collected throughout the depth of focus, yet only light which matches the path length of the reference arm contributes to the interferometric signal. The interferometric point spread function generated by axially imaging a plane approximates the axial resolution as the FWHM of the convolution of the coherence gate with the plane (figure 2-2B).

In contrast, DOCM uses a high NA objective to confocally restrict the collected scattered light axially within the depth of focus (figure 2-2C). As a result, the point spread function (figure 2-2D) demonstrates a finer axial resolution than that achieved with a low NA coherence gated system. DOCM also has a better lateral resolution when compared to DOCT as a result of its higher NA, according to the following

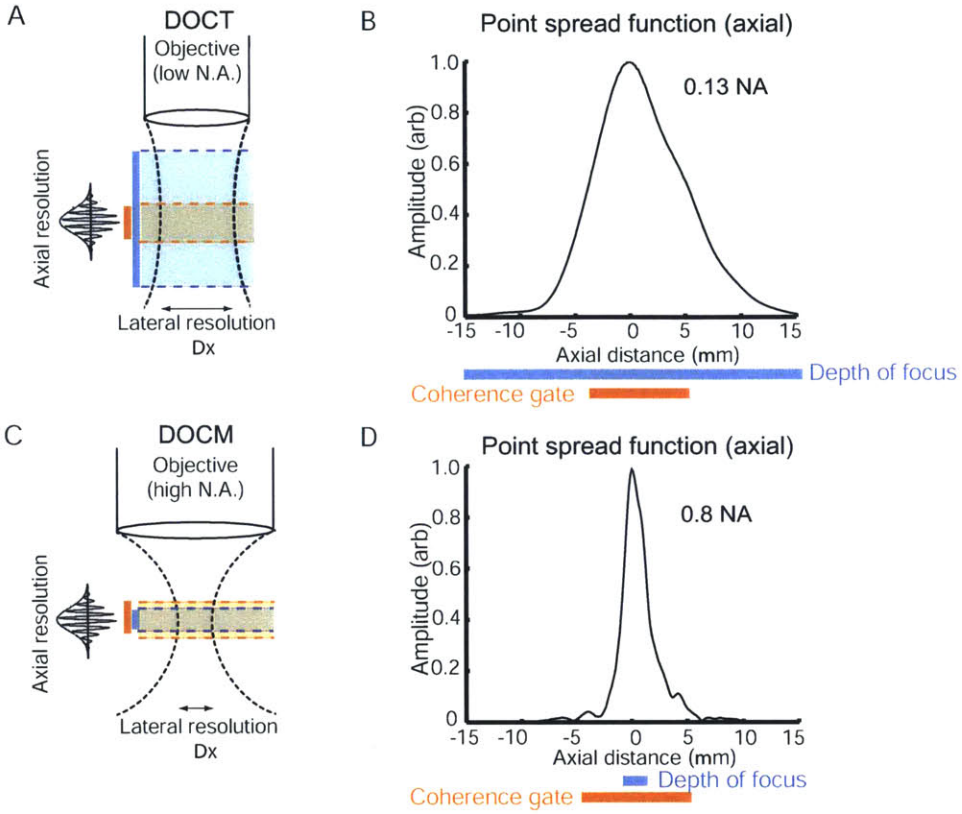

Figure 2-2: (A) Schematic diagram of DOCT setup with low NA objective highlighting large depth of focus (blue), coherence gate (orange), and lateral resolution (arrows). (B) Low NA DOCT axial point spread function determined by coherence gate (orange). (C) Schematic diagram of DOCM setup with high NA objective highlighting small depth of focus (blue), coherence gate (orange), and lateral resolution (arrows) (D) High NA DOCM axial point spread function determined by depth of focus (blue).

relationship:

$$\Delta x = 0.37 \frac{\lambda_0}{NA} \tag{2.2}$$

where Δx is the FWHM of the lateral point spread function, and is inversely proportional to NA.

Although the axial and lateral image resolutions of DOCM are both enhanced with respect to DOCT, the high NA objectives used have comparatively larger diameters and shorter working distances which make it difficult to gain optical access in tight spaces. DOCT systems have longer working distances and smaller fiber/objective diameters, allowing for easier access to the cochlea *in situ*.

Lateral scanning of the target under the sample path is accomplished using linear stepper motor stages, while transverse scanning is more quickly accomplished by moving the sample objective and reference retroreflector together on a piezoelectric scanning stage (Physik Instruments). The sample path contains a beam expander to maximize the area of light incident on the objective, while the reference path utilizes relay lenses to correct for angular dispersion caused by the AOM. The interference signal, as well as a 250 kHz reference signal, is sampled by a 12-bit A/D card at 5 MS/s via a photodetector.

Motion measurements can be obtained by measuring the instantaneous phase of the heterodyne interference signal. This is an indicator of the change in path lengths between the sample and reference arms. The complex axial displacement can be determined by

$$d(n) = \frac{1}{2k\tilde{n}}\phi(n) \tag{2.3}$$

where $k = 2\pi/\lambda$, $\tilde{n}$ is the refractive index, and $\phi(n)$ is the difference in the Hilbert transform of the instantaneous phase from the heterodyne interference and reference signals.

$$\phi(n) = \tan^{-1}\left(\frac{H[V_{het}(n)]}{V_{het}(n)}\right) - 2\tan^{-1}\left(\frac{H[V_{ref}(n)]}{V_{ref}(n)}\right) \tag{2.4}$$

Chapter 3

Tectorial membrane electrokinetics

This chapter is adapted from a published manuscript [44]. My contributions to the published manuscript include the experimental design, measurements, and analysis of results obtained from Doppler optical coherence microscopy.

3.1 Introduction

The mammalian cochlea is a remarkable sensor capable of detecting and analyzing sounds that generate subatomic vibrations [66]. This extraordinary sensing property depends on mechano-electrical transduction of cochlear hair cells [54, 55], which are functionally classified as inner and outer hair cells (OHCs). Both types of hair cells project stereociliary hair bundles from their apical surface towards an overlying extracellular matrix called the tectorial membrane (TM). Because of its strategic position above the hair bundles, the TM is believed to play a critical role in bundle deflection. Recently, genetic studies have confirmed the importance of the TM in hair cell stimulation by highlighting how mutations of TM proteins cause severe hearing deficits, even when the TM and its structural attachments appear to be normal under electron microscopy [68, 69, 100, 107, 75].

Despite significant evidence establishing the importance of the TM in normal cochlear function, relatively little is known about the TM's basic physicochemical properties and mechanistic role. Historically, models of cochlear function have repre-

sented the TM as a stiff lever with a compliant hinge, a resonant mass-spring system, or as an inertial body [25, 21, 7, 78, 79, 1, 123, 72]. However, these models exclude important phenomena, such as longitudinal coupling [122, 42, 76, 43], and assume that only mechanical properties of the TM are important. It is now clear that the TM is a biphasic poro-elastic tissue [74], which manifests longitudinal coupling in the form of traveling waves [42, 76, 43].

Furthermore, TM macromolecules comprise not only mechanical constituents [74, 38, 46, 94, 92, 39] such as collagen fibrils, but also charged constituents such as glycosaminoglycans (GAGs), which could affect mechanical properties (Fig. 3-1) [34, 73, 67, 112, 93, 111, 110, 11, 65]. GAGs in the TM carry sulfate (SO_3^-) and carboxyl (COO^-) charge groups, which are fully ionized at physiological pH and neutralized at acidic pH values (pKs between 2-4) [34]. In contrast, the net charge on TM collagen constituents is small at physiological pH because the net charge of amino (NH_3^+) and carboxyl groups is zero. The density of TM charged macromolecules has been previously inferred from pH dependent volume measurements of the TM [116, 33, 115]. Although consistent with a gel model of the TM, estimates of charge density based on changes in volume are indirect and deviate from model predictions at low pHs [115]. More direct electrical recordings are thus required to determine the net charge of TM constituents and to determine whether this amount of charge is sufficient to generate electromechanical behaviors, of the type reported in other connective tissues, such as cartilage [45, 32, 106].

Fixed charge plays a key role in determining the functional properties of cartilage. For example, nearly half of the load-bearing stiffness of cartilage has been attributed to electrostatic repulsion [11]. In addition, mechanical strain produces electrical responses (e.g., streaming potentials [65]) and electrical stimulation can lead to mechanical deformations by a process referred to as electrokinetics [45, 32]. The similarity between the structure and composition of the TM and those of other connective tissues suggests the possibility that charge could play a similarly important role in the function of the TM [34, 73].

In this study, we developed microfabricated devices that interface with the soft and

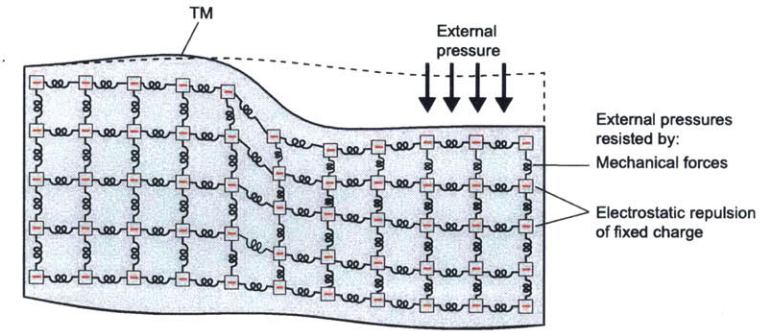

Figure 3-1: Electromechanical properties of the TM. Schematic drawing of the TM showing negative fixed-charge constituents attached to a network of mechanical springs (collagen fibers). In response to external pressure, the negative fixed charge and collagen fibers resist compression through electrostatic repulsion effects and mechanical forces, respectively.

fragile structure of fresh, excised TM segments to i) measure the fixed charge density of the TM, and ii) apply oscillatory electric fields at audio frequencies to the TM. Using these novel methodologies, we demonstrate electrokinetic phenomena elicited by the presence of fixed charge, and suggest implications for hearing mechanisms.

3.2 Results and Discussion

To determine the fixed charge concentration of the TM, we recorded the electrical responses of the TM using a microaperture chamber in a patch clamp configuration (Fig. 3-2; see Materials and Methods). The voltage measured between the baths represents the sum of the junction potentials at two TM surfaces (Fig. 3-2A and B): one bathed in artificial endolymph (AE), and one bathed in a test solution. KCl concentration in the test solution was systematically altered to modulate the adjacent junction potential via changes in charge shielding. The resulting measurements were well fit by a model based on the Donnan relation (see Materials and Methods), and provided an estimate of fixed charge density c_f of –7.1±2.0 mmol/L at physiological pH, and 3.0 mmol/L at pH 3.5 (Fig. 3-2C). These results are consistent with predictions based on biochemical composition studies [34]. The net charge of approximately –7.1 mmol/L at physiological pH is large, representing 1 fixed charge

molecule for every ~25 cations in endolymph.

To determine the mechanical contribution of charge in the TM, we analyzed a macrocontinuum model based on stress-strain relation and Donnan equilibrium [34, 106]. Internal pressures that arise from mechanical and electrostatic mechanisms resist external pressures on the TM (Fig. 3-1). The mechanical component is proportional to changes in TM volume and can be expressed as

$$p_{mech} = \frac{\kappa(V - V_o)}{V_o} \tag{3.1}$$

where p_{mech} is the hydraulic pressure, κ is the bulk modulus, V is TM volume, and Vo is the volume in the absence of a hydraulic pressure. The electrostatic component depends on the concentration of fixed charge in the TM, which tends to concentrate mobile counterions to maintain electroneutrality. This concentration of counterions increases the osmotic pressure (p_{elec}) in the TM and can be expressed as

$$p_{elec} = RT\left(\sqrt{\left(\frac{c_f}{2}\right)^2 + C^2} - C\right) \tag{3.2}$$

where R is the molar gas constant, T is absolute temperature, and C represents the concentration of monovalent ionic species (KCl) in the bath. This model predicts that electrostatic repulsion due to the –7.1 mmol/L of fixed charge density can contribute up to 0.35 kPa to the equilibrium bulk modulus κ, accounting for approximately 70% of compressive rigidity of the TM at equilibrium [74]. Under dynamic conditions, the contribution of charge to mechanical properties is also important. A recent study found that a shift to acidic pHs in the bath causes a ~2–3× reduction in dynamic shear impedance of the TM [27]. The density of charge in the TM is thus sufficient to be the basis of mechanical properties under both static and dynamic conditions, a striking finding, given the fact that the TM is highly hydrated [34, 67, 112].

The presence of charge in the TM suggests the possibility that electrical stimuli could generate a mechanical response [40, 41]. The application of oscillating electric fields at audio frequencies (1–1000 Hz) directed along the transverse axis of the TM in the microaperture chamber (Fig. 3-5A) generated displacements of the TM

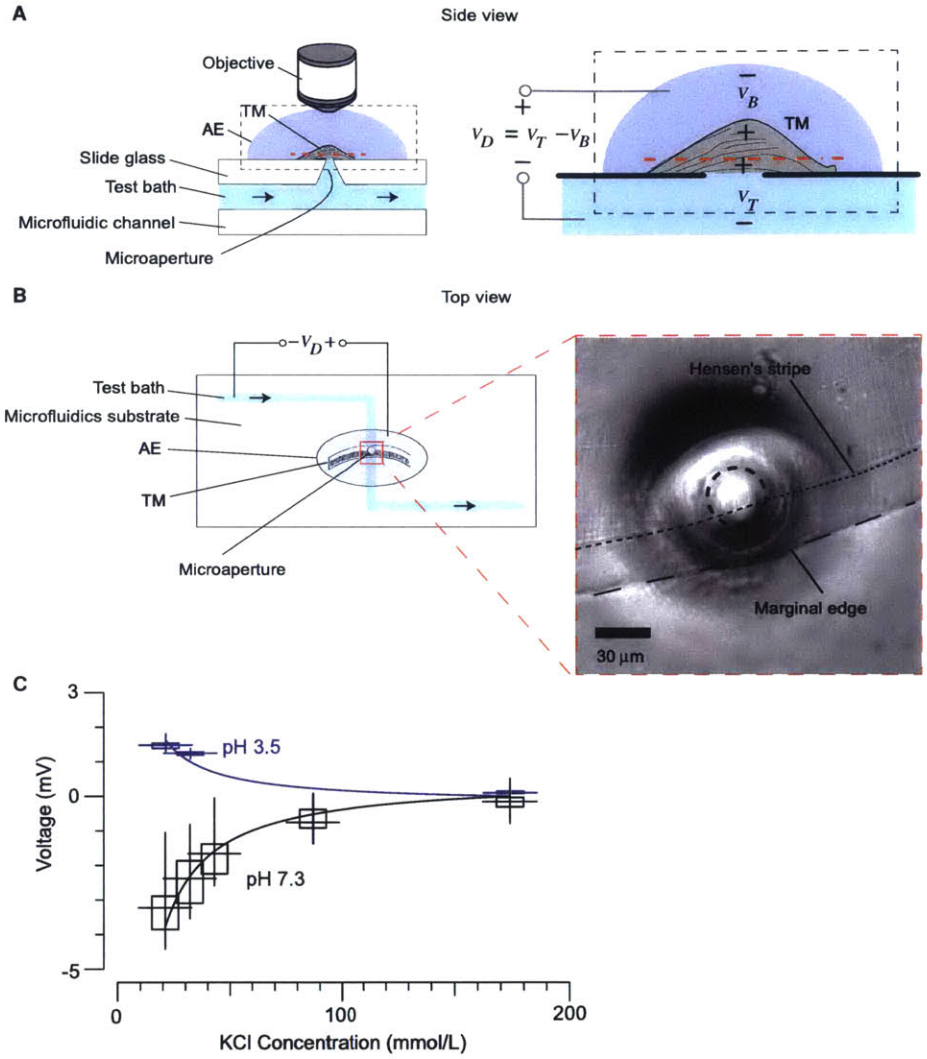

Figure 3-2: Fixed-charge density of the TM. (*A*) Schematic drawing of the microaperture setup showing side views of an isolated TM positioned over a circular microaperture. (*Left*) The microaperture creates a fluid path from the overlying bath of AE to the underlying microfluidics channel (test bath) perfused with AE-like solutions with variable KCl concentrations. (*Right*) The TM acts as an electrochemical barrier between the overlying bath and underlying fluid channel. The potential difference between the baths ($V_D = V_T - V_B$) was recorded with Ag/AgCl electrodes that were placed in contact with the two baths. (*B*) Schematic drawing of the microaperture setup showing the top view of the TM positioned over the microaperture in the region near Hensen's stripe and the marginal zone. (*Inset*) TM segment overlying the microaperture using 40× magnification. (*C*) Voltage was plotted as a function of test bath KCl concentration. Best-fit estimates to the median voltages yielded c_f (–7.1 ± 2.0 mmol/L; $n = 5$ TM preparations). Vertical lines and boxes denote extreme values and the extent of the interquartile range, respectively. Horizontal lines through the boxes denote the median values. Reducing the bath pH from 7.3 to 3.5 caused voltage measurements to change polarity and decrease in magnitude (3.0 mmol/L).

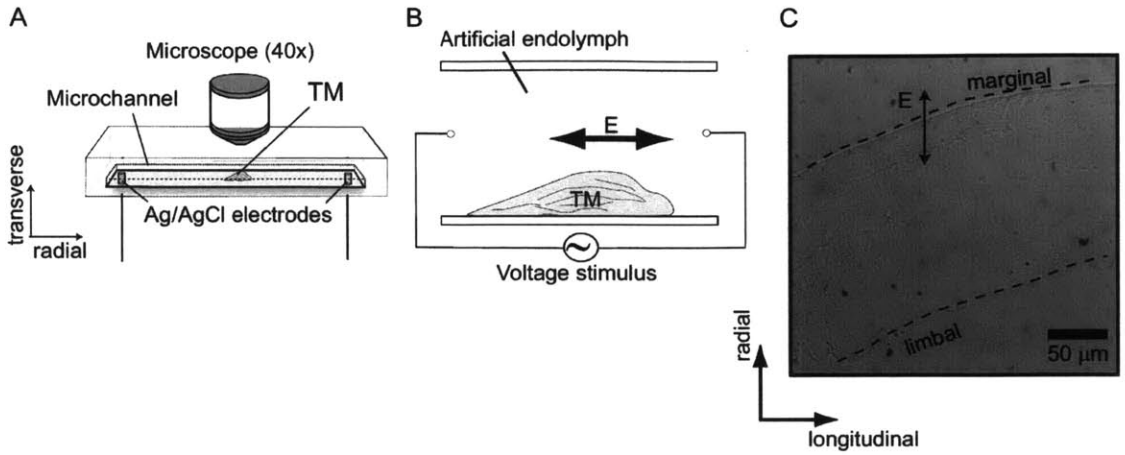

Figure 3-3: Microchannel setup with uniform electric fields applied radially to TM segments. (*A*) The TM was positioned between two application electrodes in the microchannel and observed optically at audio frequencies with stroboscopic illumination. (*B*) Magnified side view of the TM in the microfluidics channel, showing uniform electric fields directed radially. (*C*) Light microscopic image of a TM segment in the microfluidics chamber, highlighting the orientation of the TM marginal and limbal boundaries relative to the applied field.

near the marginal zone and Hensen's stripe (n = 4 TM preparations) (see SI Movie #1). Figure 3-5B shows that TM displacements had peak amplitudes of 50 nm in response to 8 kV/m (at 10 Hz) at a position on the undersurface of the TM above the microaperture. Displacement amplitudes dropped significantly with distance away from the microaperture (Fig. 3-5B), increased with electric field strength (Fig. 3-5C), and decreased as a function of stimulus frequency with the phase angle approaching $-\pi/2$ radians (Fig. 3-5D), consistent with viscous dominated interactions. Similar motion behaviors were reproduced in a microfluidics chamber used to apply radial electric fields (SI Materials and Methods; Movie #2; Fig. 3-3). Using this chamber, we measured the frequency response of the TM at very low frequencies (1–80 Hz) and exposed the TM to different perfusates in the microchannel environment. Perfusion of AE equilibrated at pH 3.5 led to a $\sim\pi$ radians shift in phase angle (Fig. 3-4A), indicating ionization of positively charged collagen groups [115] and neutralization of negatively charged GAGs.

The frequency dependence of TM displacement magnitude and phase (Fig. 3-5D, Fig. 3-4B) suggests an interplay between electrophoretic forces on the solid matrix

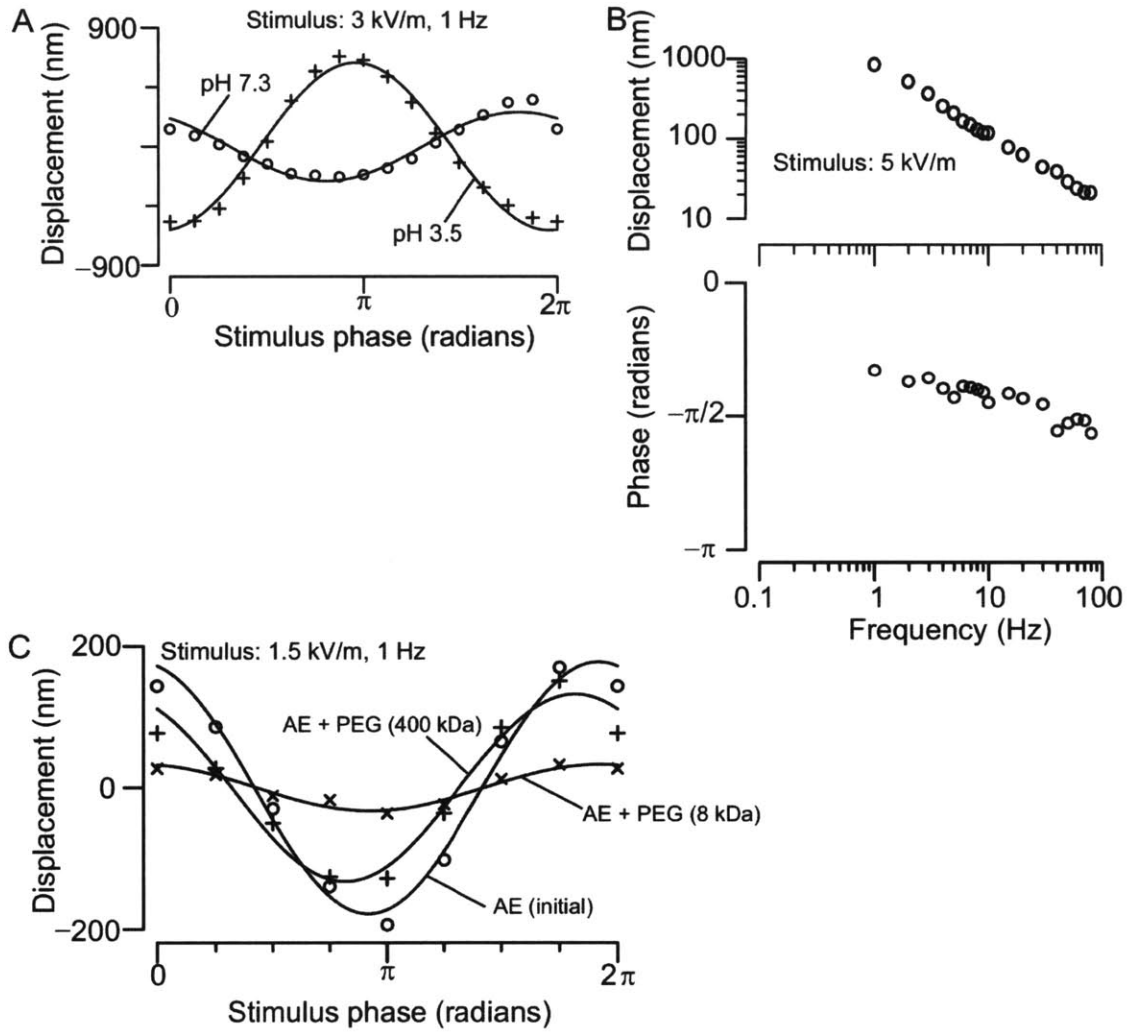

Figure 3-4: TM electrically evoked motion in the microchannel chamber. (*A*) TM motion measured in AE equilibrated at pH 7.3 vs. pH 3.5. (Stimulus: 3 kV/m at 1 Hz.) (*B*) Frequency response of TM motion showing the magnitude decreasing with frequency and phase approaching $-\pi/2$. (*C*) TM motion in the microchannel perfused with AE, AE mixed with small PEG molecules (8 kDa), and AE mixed with large PEG molecules (400 kDa). (Stimulus: 1.5 kV/m at 1 Hz.)

and electro-osmotic forces on interstitial fluid (which carries a charge that is equal in magnitude but opposite in polarity to the fixed charge on TM macromolecules) [32]. At low frequencies, these forces displace the fixed charge groups attached to the elastic matrix of the TM to generate displacements, which scale with field strength and the radius of the microaperture [113]. However, this process is viscosity limited (Fig. 3-5D), due to the small size of the pores [74]. Therefore, as the frequency of the electrical stimulus increases, there is less time per period for fluid motion through the porous matrix, and a proportional reduction in total fluid transport. The result is that electrokinetic displacements of the TM are larger at low frequencies than at high frequencies.

For asymptotically low frequencies, the solid and fluid phases separate, and electrokinetic displacements result from electrical forces acting on fixed charges embedded in the elastic matrix. To estimate the magnitude of these displacements, we modeled the TM as a semi-infinite, isotropic, elastic matrix, which overlies a circular aperture (25 μm diameter) through which current is passed. The mechanical properties of the matrix were represented by Young's modulus (~105 Pa for a basal TM segment) [42, 46]. The matrix was assumed to have a uniform electrical resistivity (0.3 Ωm) and fixed charge density q (~7×105 C/m^3), determined from the measurements in this study (c_f ~7 mmol/L; Fig. 3-2). The equations of motion were solved using finite differences (SI Results), with the result that electric fields of 1 kV/m (generated by ~2 μA of current) produced electrokinetic displacements on the order of 1.5 μm. This motion estimate is based on a quasistatic model of the TM, which is appropriate at asymptotically low frequencies. However, the motion measurements in Fig. 3-5D show strong frequency dependence of motion (with slope of –1) over the measured range of frequencies (which is limited at low frequencies by table vibrations and thermal drift). We expect the trend shown in Fig. 3-5D to continue (to lower frequencies) until the transition to quasistatic behavior occurs, at frequencies that correspond to the poroelastic relaxation time (which is on the order of tens of minutes, based on previous osmotic experiments [74, 34]). Thus the transition frequency is 2–3 orders of magnitude below our lowest measured frequency, and we expect the quasistatic

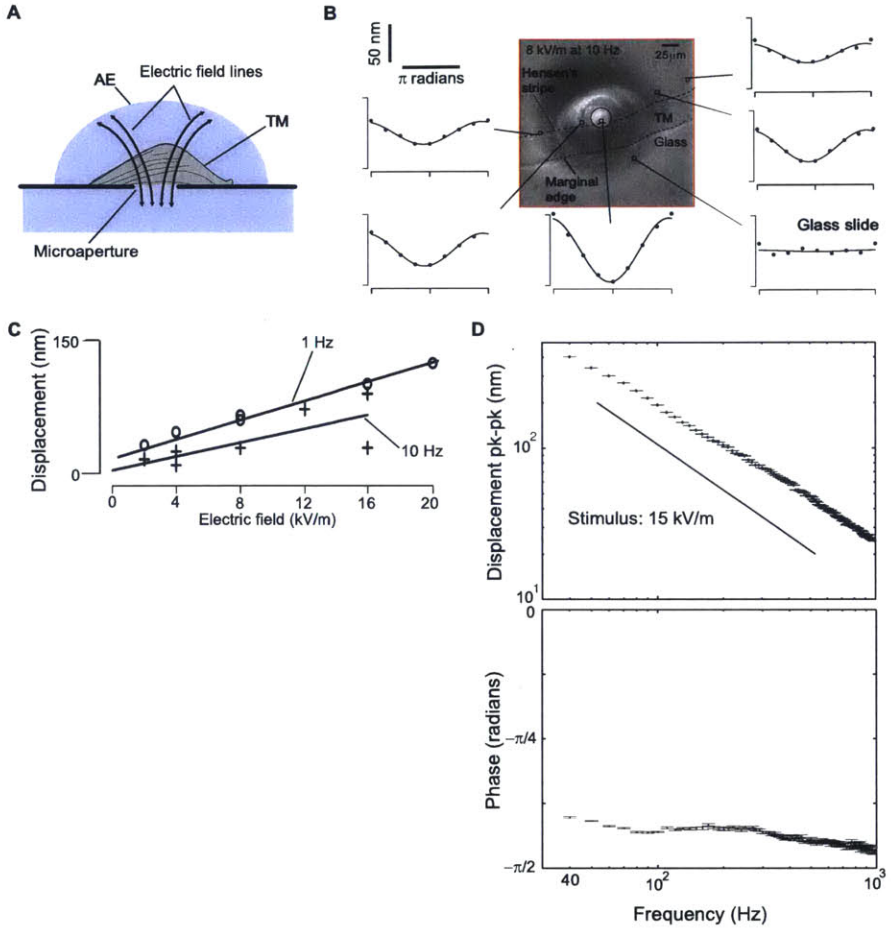

Figure 3-5: TM electrokinetic response. (*A*) The microaperture setup was used to deliver electric fields to the TM with a pair of Ag/AgCl-stimulating electrodes. Electrically evoked displacements were measured using computer microvision and DOCM systems (*Materials and Methods*). Voltages were delivered with Ag/AgCl electrodes positioned in the top bath and in a reservoir connecting to the underlying fluid channel. Electric fields were computed based on the geometry of the microaperture, and electrical current was measured across a resistor that was placed in series with the microaperture chamber during voltage application. (*B*) Transverse displacements were sinusoidal and largest in the regions of the TM directly overlying the microaperture and decreased with radial distance away from the microaperture. A typical TM segment excised from the middle turn exhibited electrically evoked displacements up to ~45 nm in response to electrical stimuli applied in the middle zone region directly overlying the microaperture (10 Hz; 8 kV/m). Motion amplitudes varied depending on whether the TM sample was a basal or an apical segment. (*C*) Displacements scaled linearly with electric field magnitude for TM samples excised from the middle turn of the cochlea (n = 4 TM preparations). (*D*) (*Upper*) Displacement amplitudes decreased with increasing stimulus frequency (40–1,000 Hz) with a slope of –1 (solid line) for a typical apical TM segment. Black dots denote the mean value of TM displacement. (*Lower*) Phase angle of TM displacement as a function of frequency. Vertical lines with horizontal bars denote SEM.

motion estimate to be 2–3 orders of magnitude larger than the measured range of motions.

Under dynamic conditions, viscous forces increasingly couple electro-osmotic and electrophoretic forces, which are equal in magnitude but opposite in direction. To test the effect of pore size and interstitial fluids on TM electrokinetics, we measured TM motion in response to changes in viscosity by introducing different size PEG molecules in AE (SI Results and Materials and Methods). We altered the viscosity of the fluid surrounding the TM by perfusing AE mixed with large PEG molecules (10 μmol/L, 400 kDa), which could not penetrate the TM. To alter internal viscosity of the TM, we perfused AE mixed with small PEG molecules (10 mmol/L, 8 kDa), whose radius of gyration was sufficiently small to enter through TM nanopores [74]. Adding small PEG molecules caused TM motion to decrease by ~6.5×, whereas, adding large PEG molecules caused relatively minor changes in TM motion (Fig. 3-4C). Changing internal viscosity of the TM is functionally equivalent to reducing TM pore size, suggesting a strong dependence of TM electrokinetic interactions on effective porosity and a weak dependence on external viscosity of the surrounding fluid. These results provide a framework for a general poroelastic model of the TM under both quasi-static [74] and dynamic conditions, thereby highlighting the important interplay between fixed charge groups, porosity and the internal water content of the TM at the nanoscale. Electrically-evoked displacements of the TM may have important implications for electrical stimulation of the cochlea [119, 102, 12, 80, 58]. Mechanical responses to electrical stimulation have generally been attributed to OHC somatic and hair bundle motility mechanisms. While exogenous application of electrical currents undoubtedly excites sensory receptor cells, our results suggest that electrically induced TM motions must also be taken into account if electrical currents flow through the TM. Thus, electrically-evoked motions of the cochlear partition may be at least partially stimulated by TM electrokinetics, especially at low audio frequencies. Electrokinetic properties of the TM could interact directly with hair cell ion channels. Although the exact position of hair cell transduction channels relative to the TM remains unclear, it is well known that the undersurface of the TM is in close proximity

(nanometer-scale separation) to the tallest rows of stereocilia [53, 30, 6]. Figure 3-6A and B shows the TM-hair bundle interface and highlights how transduction currents, driven predominantly by potassium and calcium ions, generate electric fields, which in turn, could exert local force on TM macromolecules. Although it is unlikely that transduction currents generate bulk movements of the TM in vivo, it is possible that local electrically induced deformations of the TM could occur near single stereocilia ion channels.

A previous study of electrical recordings from the bullfrog's sacculus found electric field magnitudes of ~1 V/m at distances ~1 μm from the tips of the stereociliary hair bundles containing clusters of ion channels (51). These electric fields depend not only on the magnitude of the current but also on the spatial proximity of the TM relative to the ion channels. If we assume ~20 pA transduction currents through a solitary ion channel [28, 57] and a distance of ~1 μm from the channel opening, the electric fields would be in the range of those measured by Hudspeth (labeled 'Ref. 51' in Fig. 3-6C [53]). However, as the distance to the ion channel is decreased, the field strength increases rapidly. For example, at distances within 7–30 nm of an ion channel, the field strengths are 103–104 V/m, similar to those applied in the microaperture chamber (labeled 'This study' in Fig. 3-6C). Electrically-evoked TM motions and forces produced by transduction electric fields depend on the material properties of the TM as well as the channel geometry. If we assume that a solitary ion channel is modeled as a single nanopore, then we can estimate the magnitude of TM displacements by scaling the measurements in the microaperture setup (Fig. 3-5). TM motion in the microaperture setup under quasistatic conditions (dμ ~1.5 μm) is proportional to the applied electric field strength (E_μ ~103 V/m), where the proportionality constant is the effective charge (q_μ) divided by TM stiffness (k_μ). The stiffness k_μ scales with the radius of the microaperture [113] and is therefore ~104 smaller near an ion channel (~1-nm radius), whereas the quantity of charge q_μ scales with the volume of the TM overlying the microaperture. As a result, the proportionality between dμ and E_μ changes by a factor of 108 for a single ion channel relative to the microaperture. On that basis, we predict TM displacements (d_{ch})

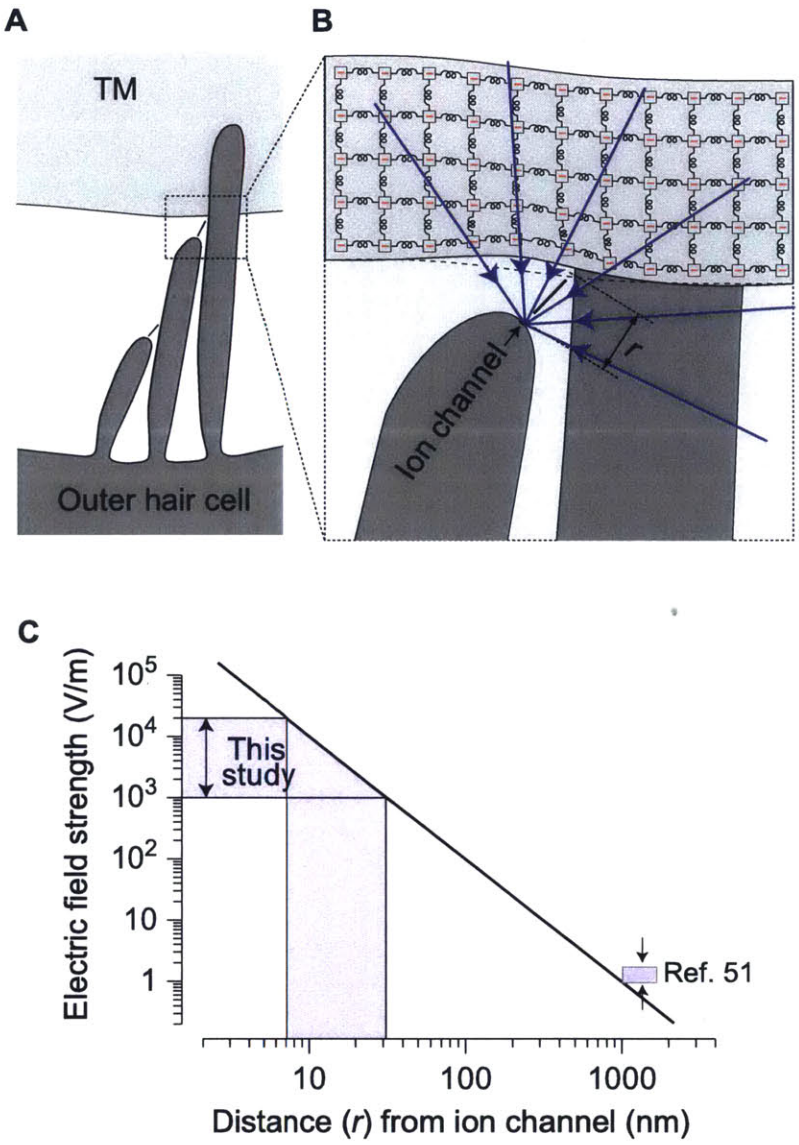

Figure 3-6: TM electrokinetics near hair cell ion channels. (*A*) Schematic drawing of a cochlear partition showing the orientation of the TM relative to OHC stereocilia and tip links. (*B*) *Inset* shows the OHC ion channel as a point source with radial electric fields (blue arrows) acting on TM fixed-charge macromolecules locally over small distances r. (*C*) Model predictions of electric field magnitudes as a function of radial distance r from the opening of the ion channel. Electric fields were estimated based on experimental values for single-channel transduction currents, resistivity of the ionic environment, and the radius of the ion channel from previous data [53, 30, 6, 28, 57]. The shaded region labeled "This study" denotes the range of electric field (10^3–10^4 V/m) magnitudes applied in the microaperture chamber with values corresponding to ~7–30 nm from the ion channel opening. The shaded region labeled "Ref. 51" denotes electric fields (~1 V/m) measured at ~1 μm from the tips of hair bundles in the bullfrog's sacculus [53]. In both cases, radial distances r are significantly larger than the TM's space charge layer thickness [11].

near an ion channel to be ~0.01 nm in response to Ech adjacent to a nanochannel (Fig. 3-6C). Because the electric field strength depends linearly on the number of stereociliary channels, the aggregate TM motion for ~75 channels (d_{hb}) for a given hair bundle would be ~0.75 nm. TM displacements at the ion channel and bundle level scale linearly with electrical current I (SI Results). This linear dependence of TM motion on electrical current is consistent with a finite difference model (SI Results), which predicts TM motion estimates on the order of those based purely on scaling. The total mechanical energy available from TM electrokinetic motions (SI Results) is the product of ${d_{hb}}^2$ and TM stiffness (k_{TM} ~1.33 N/m for a basal TM segment over a 5-μm radius) [42, 46, 113], yielding ~0.75 aJ for basal TM segments and on the order of ~7.5 aJ for apical TM segments with lower stiffness (k_{TM} ~0.13 N/m for an apical TM segment over a 5-μm radius) [42, 46, 113]. These energy estimates are comparable to the amount of work needed to deflect hair bundles during calcium-driven bundle motility (~2 aJ) and are significantly larger than the work performed against viscosity during bundle movements (~0.1 aJ) [15, 8], suggesting that electrically-evoked motions of the TM could interact with mechano-electrical transduction (MET) currents of the hair bundles. The direction of TM motion and the associated feedback mechanism at the level of the hair bundles depend on the location of the MET channels. If the ion channels face towards the inhibitory direction of bundle motion (i.e. if they are on the side that is closest to a shorter stereocilia), the net electric field that is caused by opening the channels will generate a force that will tend to close the channels, consistent with negative feedback. If, on the other hand, the ion channels face towards the tallest stereocilia (as in Fig. 3-6B), the net electric field would force TM negative charge groups in the direction of positive bundle deflection to open more ion channels, as the basis of a positive feedback mechanism for amplification.

Beyond cochlear mechanics, our findings have important implications for all sensory systems, which (with the exception of a few species of lizards) all contain accessory gelatinous structures overlying hair cells. Gels, like the cupulae and otolithic membranes found in the vestibular system, and those covering electrosensory hair cells

on the skin of aquatic vertebrates play a key role in hair cell stimulation [35, 10, 85]. Much like the TM, these gels are poised to undergo deformations in response to transduction currents. The effect of electrokinetics may be even greater in these sensory systems because their mechano-electrical transduction channels operate at significantly lower frequencies than those in the cochlea.

3.3 Conclusions

Results reported in this study show that the TM contains a high density of fixed charge that contributes to the compressive stiffness of the TM and can generate electrokinetic phenomena. Electrical stimuli applied to the TM evoke nanometer-scale displacements at audio frequencies by exerting force on the solid matrix (fixed charge macromolecules) and fluid phase of the TM. This motion is directly related to the density of fixed charge inside the TM and may have important implications for cochlear mechanisms. Although the exact proximity of hair cell ion channels relative to the TM is not well known, the electric fields generated by mechano-electrical transduction are large near the undersurface of the TM and can thus generate local nanometer-scale deformations of the TM in vivo. TM electrokinetic properties may thus play an important role in the deflection of cochlear hair bundles, suggesting, more broadly, that electrokinetic mechanisms may control the interaction of overlying gels and hair bundles in all sensory systems.

3.4 Materials and Methods

3.4.1 Isolated TM Preparation

TM segments were excised from the cochleae of adult male mice (strain CD-1, 4–8 weeks old, Taconic) using a previously published surgical technique [105]. The cochlea was surgically removed and placed in an artificial endolymph (AE) bath containing 174 mM KCl, 5 mM Hepes, 3 mM dextrose, 2 mM NaCl, and 0.02 mM CaCl2. The bath was equilibrated at pH 7.3 at room temperature. The bone casing of the cochlea

was gently chipped away until the organ of Corti was exposed. A combination of bright and dark-field illumination with a dissection microscope (Zeiss) provided visual access to the TM above the organ of Corti. A sterilized eyelash was used to gently lift the TM from the cochlea. TM segments (typically 0.5–1 mm in length) were isolated from the organ and placed in a fresh artificial endolymph (AE) bath. The care and use of animals in this study (NIH Grant R01 DC00238) were approved by the Massachusetts Institute of Technology Committee on Animal Care.

3.4.2 Microaperture Chamber

The microaperture chamber contained a glass-drilled microaperture (12.5 μm radius) (Lenox Laser, MD) connecting two fluid-filled compartments in the form of a microchannel and an overlying bath (Fig. 3-2A). The underlying microchannel was cast in a transparent elastomer called poly(dimethylsiloxane) (PDMS; Sylgard 184, Dow Corning) by applying a standard soft lithography technique [2], in which a PDMS replica of the underlying channel was cured and subsequently sealed to a glass slide containing the microaperture. For fixed charge density measurements, the top bath was perfused with artificial endolymph (AE) and the microchannel was perfused with AE-like solutions in which the KCl concentration and pH were varied. KCl concentrations of 21 mM, 32 mM, 43 mM, 87 mM, and 174 mM were used at pH 7.3 and 3.5. Each test bath was perfused twice to test for repeatability. For electrokinetics measurements, the top bath and microchannel were both perfused with AE.

3.4.3 Measuring Fixed Charge Density c_f

Isolated TM segments were mounted in the microaperture chamber so that an electrochemical barrier separating the solutions in the two compartments was formed (Fig. 3-2A). The DC voltage difference (VD) between the two compartments was measured with Ag/AgCl microelectrodes (AM Systems) housed in large tip micropipettes containing 3 M KCl solution and solidified in agarose. The electrodes were positioned in the top bath and in the reservoir connecting to the microchannel. This configuration

allowed uniform electric fields to be delivered in the regions of the TM directly overlying the microaperture. The electrodes were coupled through an amplifier (DAM60-G Differential Amplifier, World Precision Instruments) and a multimeter (TX3 True RMS Multimeter, Tektronix) connected to a computer. DC potentials were stored in the computer at 2 s intervals. The DC potential difference between the two baths depends on the ionic concentration of the two baths and on TM fixed charge density in this configuration. Therefore, by measuring the electric potential difference across the TM, we can estimate TM fixed charge density. The potential difference arises primarily from Donnan potentials that form between each bath and the TM, due to the presence of fixed charge. The potential between each bath and the TM is

$$V = \frac{RT}{F}\left(\sqrt{\left(\frac{c_f}{2C_\Sigma}\right)^2 + 1} + \frac{c_f}{2C_\Sigma}\right) \tag{3.3}$$

where V is the potential of the TM relative to the bath, R is the molar gas constant, T is absolute temperature, F is Faraday's constant, c_f is the concentration of fixed charge within the TM, which can be either a positive or negative quantity, and $C_\Sigma = (1/2)\Sigma_{ci}$ is one half the sum of the concentrations ci of each ion in the bath. Since the bath consisted mainly of KCl, we estimated $C_\Sigma = (1/2)(c_K + c_{Cl})$. If the two baths have identical compositions, the Donnan potential between the TM and each bath is identical, so the net potential difference between baths is zero. If one bath has a lower ionic concentration, the magnitude of the Donnan potential increases, so the potential difference between baths deviates from zero in a manner that depends on c_f within the TM. When the two baths have dissimilar ionic strengths, in addition to the Donnan potential, a liquid junction potential (LJP) can arise between the baths. To accurately measure the Donnan potential, it is important to minimize and measure the LJP. In this respect it is convenient that the TM normally resides in AE, which consists primarily of K^+ and Cl^-. Since these two ions have similar mobilities, the junction potential resulting from a concentration difference between baths is minimized.

3.4.4 Measuring Electrokinetic Motion of the TM

The microaperture setup was also used to apply voltages to TM segments. Isolated TM segments were placed over a ~12.5 μm radius microaperture and both compartments were perfused with AE. Sinusoidal voltages applied between the compartments generated electric fields in the middle and marginal zones of the TM covering the aperture (Fig. 3-5A and B). Displacements were visualized in the transverse direction across multiple focal planes within the bulk of the TM using a computer vision technique and a Doppler optical coherence microscopy (DOCM) technique [42, 52].

We also developed a microfluidics chamber (Fig. 3-3) used to apply electric fields to the TM in the radial (in plane) direction (SI Materials and Methods) [41]. Fluids were perfused through the microfluidics chamber, allowing equilibration of AE at different pHs and with polyethylene glycol (PEG) (Fig. 3-4A and C) for TM motion amplitude, phase and polarity studies.

3.4.5 Motion Analysis with Computer Vision System

Images of the TM were collected optically with a 40× water immersion objective (0.8 N.A., Zeiss Axioplan) and a transmitted light condenser (0.8 N.A.). TM motion was measured with a 12 bit, 1024 by 1024 pixel CCD camera (CAD7-1024A; Dalsa Inc.) by strobing the light emitting diode (LED). The TM segment was illuminated at 16 evenly spaced stimulus phases (over a stimulus cycle) at multiple optical planes separated by 1 μm. The collected images were then analyzed to determine the first 8 harmonics of the periodic motion. We computed the magnitude and phase of radial displacement from the series of collected images by using previously published motion-tracking algorithms [42, 43].

3.4.6 Motion Analysis with Doppler Optical Coherence Microscopy

TM electrically evoked motions in the microaperture chamber were confirmed using a previously published Doppler optical coherence microscopy (DOCM) system, which

reconstructs motion from weakly scattering light reflected from multiple axial depths through the TM [52]. The DOCM system has sub-nanometer resolution and was used to characterize TM motion as a function of stimulus frequencies.

3.5 Supplemental DOCM results

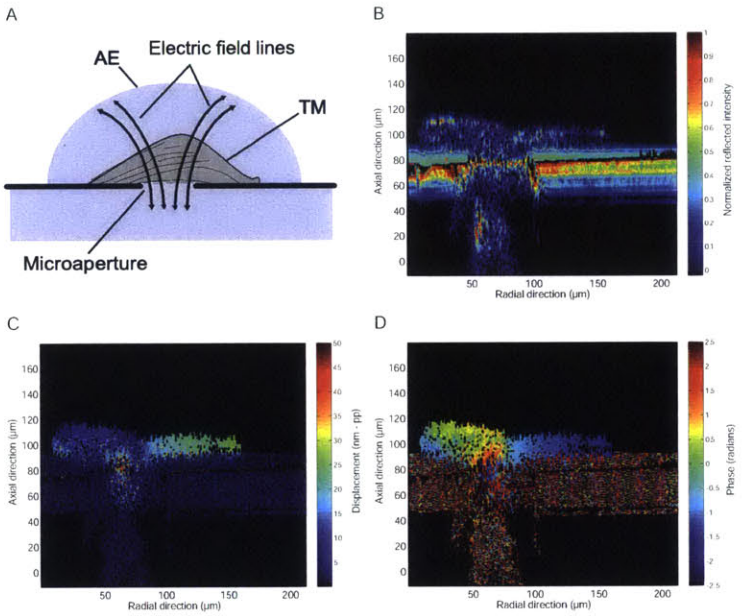

Figure 3-7: TM electrokinetic response with 50 Hz sinusoidal electric field at 1 kV/m. (*A*) The microaperture setup was used to deliver electric fields to the TM with a pair of Ag/AgCl-stimulating electrodes. Electrically evoked displacements were measured using computer microvision and DOCM systems (*Materials and Methods*). Voltages were delivered with Ag/AgCl electrodes positioned in the top bath and in a reservoir connecting to the underlying fluid channel. Electric fields were computed based on the geometry of the microaperture, and electrical current was measured across a resistor that was placed in series with the microaperture chamber during voltage application. (*B*) DOCM 1 μm$\times$ 1μm resolution image of a TM segment across the microaperature setup. (*C*) Displacement (nm_{pp}) and (*D*) phase (radians) maps in response to a 50 Hz sinusoidal electric field at 1 kV/m.

Chapter 4

Cochlear morphology

In this chapter we describe methods to acquire images using optical coherence microscopy/tomography and apply those methods to characterize cochlear morphologies in three species: Mice, guinea pigs, and Mongolian gerbils.

4.1 Methods

4.1.1 *In situ* preparation

4.1.1.1 Animal preparation

Cochleae were excised from guinea pigs, gerbils (figure 5-1), and mice. The animals were euthanized via CO_2 and decapitated. The bulla containing the cochlea was isolated and opened. Care was taken to preserve the stapes so that the cochlea could be stimulated by vibrating the stapes. The stapedius and tensor tympani tendons were precisely cut to avoid stapes damage upon incudo-stapedial joint and middle ear separation. The isolated cochlea, was fixed to a Petri dish using two-part dental cement (Durelon, ESPE Dental-Medizin GmbH) and bathed in a low Ca, low Cl, artificial perilymph with a pH of 7.30. A small hole (approximately 0.5 mm^2) was made in the temporal bone above the apical turn to allow for 841 nm superluminescent diode (SLD) optical access. The care and use of animals in this study were approved by the Massachusetts Institute of Technology Committee on Animal Care.

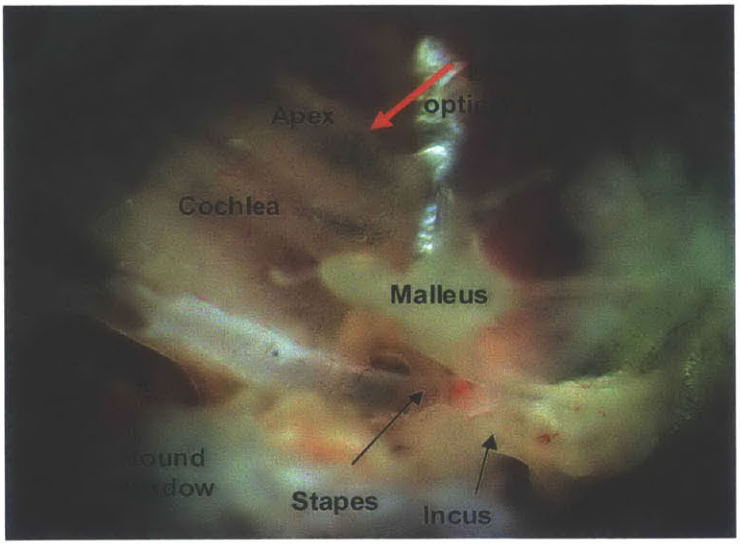

Figure 4-1: Inner ear of the Mongolian gerbil as seen through the opened bulla. The desired apical optical access is denoted with a red arrow. The three middle ear bones are labeled: Malleus, incus, and stapes.

4.1.1.2 Health

In vitro preparations are monitored for hair cell blebbing [3]. Isolated cochleae are bathed in an artificial perilymph solution with low calcium and chloride content to reduce hair cell blebbing. The pH of the artificial perilymph was maintained at 7.30 to match biological pH and consisted of 7 mM sodium chloride (NaCl), 163.4 mM sodium gluconate ($C_6H_{11}NaO_7$), 3 mM potassium chloride (KCl), 0.1 mM calcium chloride dihydrate ($CaCl_2{\cdot}2H_2O$), 0.1 mM magnesium chloride ($MgCl_2$), 2 mM sodium sulfate (Na_2SO_4), 0.5 mM sodium dihydrogen phosphate (NaH_2PO_4), 5 mM HEPES ($C_8H_{18}N_2O_4S$), 5 mM dextrose ($C_6H_{12}O_6$), and 4 mM L-glutamine ($H_2NCOCH_2CH_2CH(NH_2)CO_2H$).

4.1.1.3 DOCM optical methods

Axial measurements were performed using DOCM previously described in Chapter 2. Isolated cochleae were placed under a 40× water immersion objective (figure 5-3) on a lateral-axes motor driven scanning stage. The objective was mounted to a piezo electric driven axial stage. Together, these stages allowed for axial motions to be

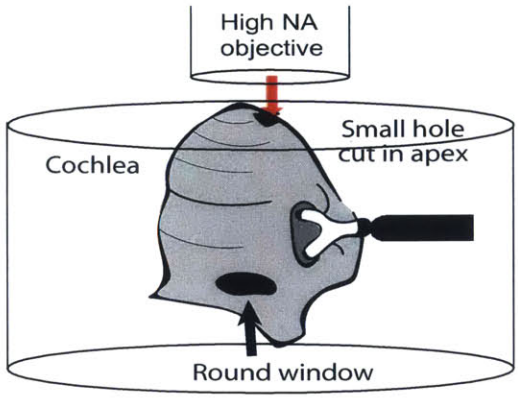

Figure 4-2: *In vitro* preparation. Cochleae are affixed using dental cement to a Petri dish. A high numerical aperture (NA) objective focuses through an approximate 0.5 mm apical hole. A piezoelectric titanium transducer creates sinusoidal stapes-induced cochlear excitation.

measured at each point throughout the isolated preparation. Cross-sectional scans are acquired by first moving the piezo driven axial stage (A-scan), followed by an increment in the lateral motor stages (B-scan), then repeating the process.

Light from the sample path of the DOCM system exits the objective and converges toward its focal point. As the objective moves axially (during the A-scan), the reference path moves with it, maintaining equal sample and reference path lengths. This allows continuous depth sectioning at the focal point of the objective. Since the depth of focus for the 40x water immersion objective is smaller than that of the interferometric coherence gate, optical transverse sectioning resolution is limited by the point spread function of the objective at approximately 2 μm. Depth sectioning is performed by passing the output sample path light through a hole made in the apical temporal bone. The light is scattered by Reissner's membrane and subsequent deeper tissues, a portion of which is recollected by the objective and mixed with the reference signal. This heterodyned interferometric signal is used to determine how much light is scattered at a given depth, as well as the direction and magnitude of motion.

4.1.2 Image intensity resolution

As described in chapter 2, one of the hallmarks of OCT is the enormous range of detectable backscattered light intensities. Our system is capable of detecting light with reflectivities as low as 10^{-7}. The final stage in the process is a 12-bit analog to digital converter. This limits the range of image light intensity information to 4096 quantization levels or ~$10^{3.6}$, which can be adjusted through a variable gain photodetector.

Figure 4-3A shows a representation of the normalized reflected light scattered from a cross-section of the *in vitro* guinea pig cochlea. Three structures are labeled in both figures: Reissner's membrane, the tectorial membrane, and the reticular lamina. Many structures are quite bright, but most of the image is faint, including the tectorial membrane. A line plot of reflectivities along a single radial position (white line) is shown in figure 4-3B and it can be seen that fewer than 5% of the pixels are above half maximum. In fact, ~16% of line reflectivity fall between 1 and 10^{-1}, while ~31.5% fall between 10^{-1} and 10^{-2} and ~52.5% fall between 10^{-2} and 10^{-3}.

To better represent faint structures, and preserve bright structures, we can replot the same data on a logarithmic scale as shown in figure 4-3C. Unlike the figure 4-3A, which was mostly blue, i.e. mostly below the midpoint, figure 4-3C compresses reflectivities into a smaller range, allowing structures that weakly scatter to appear alongside those with high reflectivity. Logarithmic compression is demonstrated by comparing the logarithmic line plot in figure 4-3D to that of the linear line plot in figure 4-3B, it can be seen that logarithmic plotting brought the peak TM reflectivity much closer to that of the RM and RL.

Noise rejection can further enhance the appearance of the image. Figure 4-3E and F show the image map and line plot with a threshold of $10^{-1.8}$ (black line in figure 4-3D). Reflectivities falling below the threshold are ignored, and the color map range is is adjusted to represent the smaller dynamic range. Noise rejection thresholds vary depending on alignment factors and are generally calibrated for each image.

One side effect of logarithmic compression is a widening in axial thickness of struc-

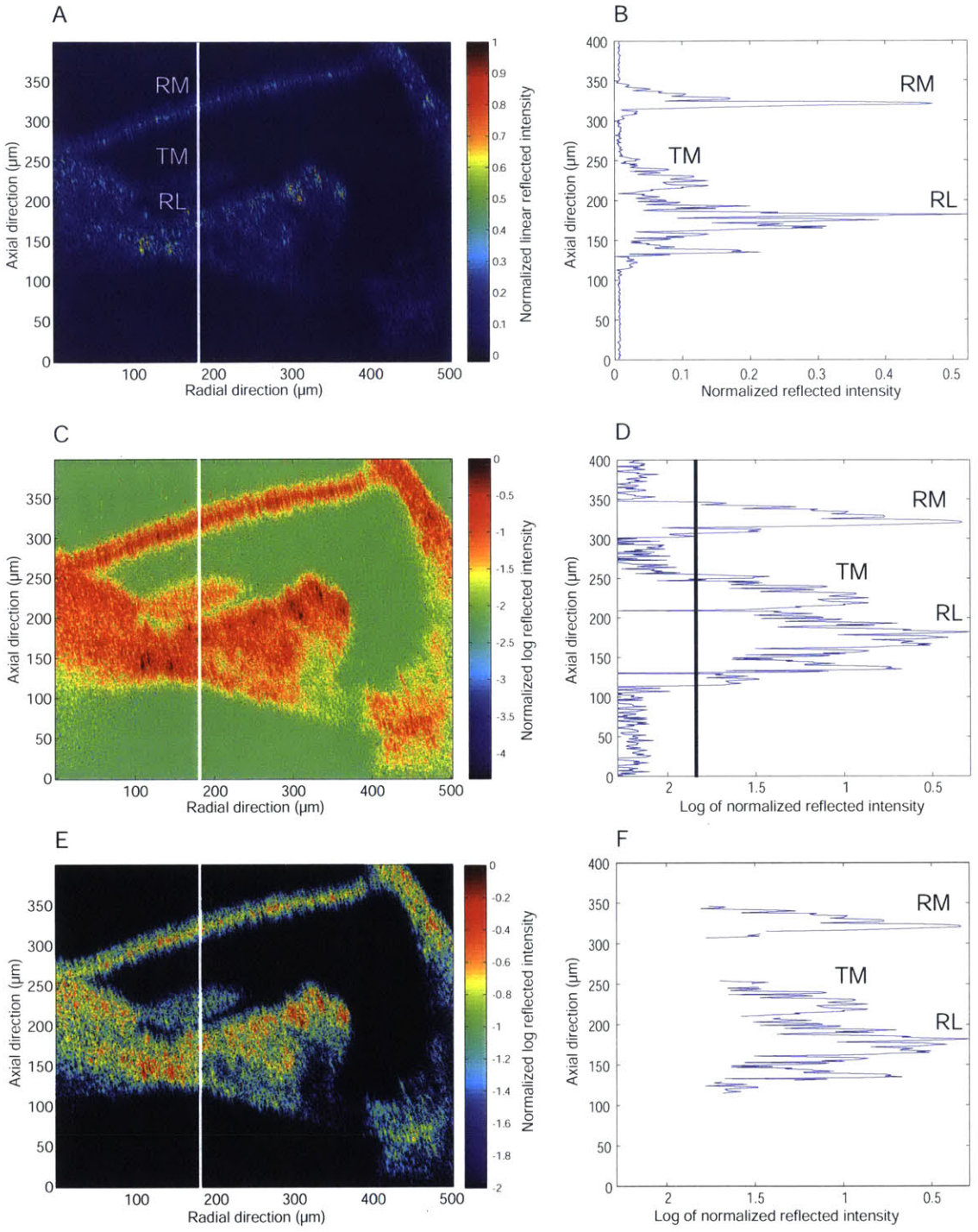

Figure 4-3: Cross-section of the organ of Corti in the apical turn of the *in situ* guinea pig cochlea. (A) Linear representation of the normalized reflected intensity. (B) Plot of linear reflected intensity at one radial position (182 μm, denoted by white line). (C) Logarithmic representation of the normalized reflected intensity. (D) Plot of logarithmic reflected intensity at above radial position. (E) Logarithmic normalized reflected intensity after noise reduction (Rejection for normalized intensity < 0.015). (F) Logarithmic reflected intensity with noise rejected.

tures. The full width at half maximum axial thickness for the linear representation of Reissner's membrane (figure 4-3B) is ~5 μm while the full width at half maximum value for the logarithmic representation of Reissner's membrane (figure 4-3D) is ~20 μm. In this case, Reissner's membrane increased in apparent axial thickness by ~4×.

Not all structures within the same image have the same apparent thickness increase. For example the full width at half maximum axial thickness for the linear representation of the tectorial membrane (figure 4-3B) is ~27 μm while the full width at half maximum value for the logarithmic representation of Reissner's membrane (figure 4-3D) is ~42 μm. In this case, Reissner's membrane increased in apparent axial thickness by ~1.5×. Thinner structures have the largest apparent axial thickness increase under logarithmic compression.

4.1.3 Image spatial resolution

As described in chapter 2, a number of factors limit the spatial resolution including the point spread function of the microscope, the coherence gate of the interferometric system, and the spatial resolution of the scanning apparatus.

4.1.3.1 Scanning apparatus radial and axial spatial resolution

Operationally, we first perform a low resolution image acquisition to locate and orient the structures of interest. Time domain optical coherence tomography improves motion measurement resolution at low frequencies at the expense of scanning time. Low resolution scans are used to determine a coordinate system to locate regions of interest. With a rough idea of where structures are, the acquisition of fast per pixel measurements or slow high resolution single frequency and level motion and phase maps can be performed.

Figure 4-4 illustrates the effect of the spatial resolution selection of the scanning apparatus. Figure 4-4A shows a axial and radial step size of 5 μm, while figure 4-4B was performed with a higher resolution axial and radial step size of 1 μm. The higher resolution looks much better but has the disadvantage of having taken 30 × longer to

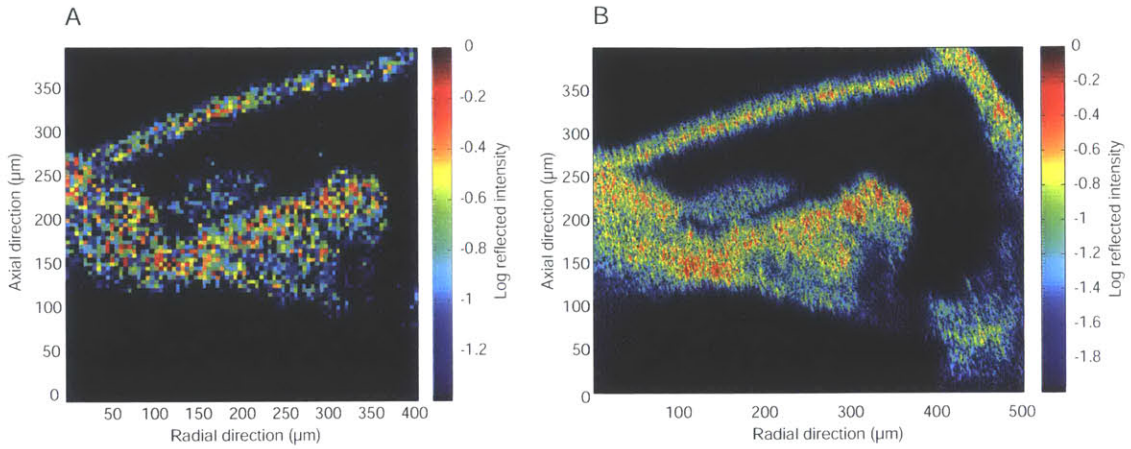

Figure 4-4: Low and high resolution cross-sectional images of an apical turn of the *in situ* guinea pig cochlea. Both images were acquired using the same 40X water objective and same preparation. (A) 5 μm $\times$ 5 μm low resolution image. Area of 400 μm $\times$ 400 μm. (B) 1 μm $\times$ 1 μm high resolution image. Area of 500 μm $\times$ 400 μm.

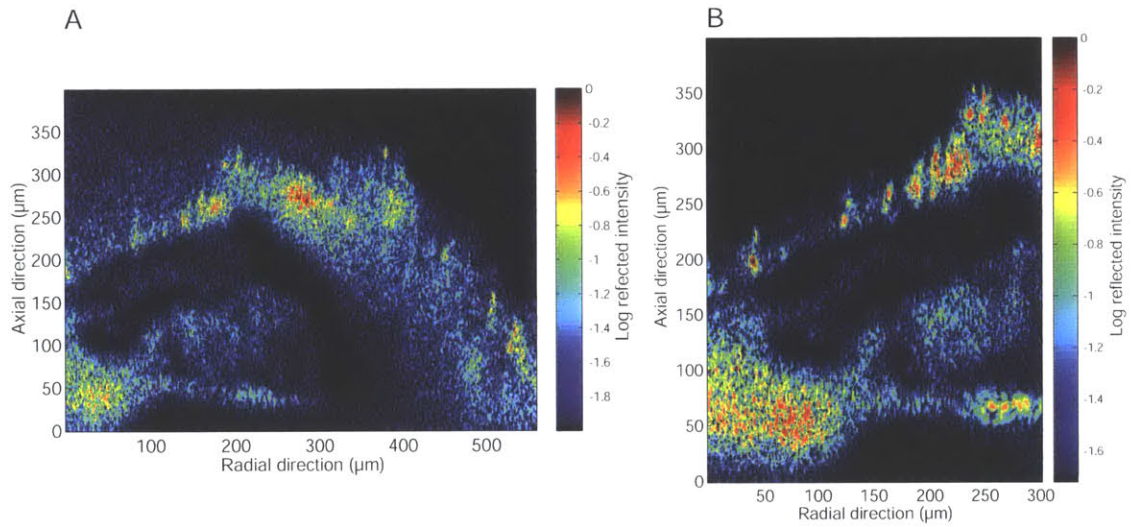

Figure 4-5: Cross-section of an apical turn of the *in situ* Mongolian gerbil cochlea. Both images are taken from the same preparation. (*A*) Wide view of an entire turn, 559 μm $\times$ 400 μm with a resolution of 1 μm $\times$ 1 μm. (*B*) View of the organ of Corti only, 300 μm $\times$ 400 μm with a resolution of 1 μm $\times$ 1 μm.

image. In total figure 4-4A took ~10 minutes to acquire an area of 400 μm $\times$ 400 μm, while figure 4-4B took 5 hours to acquire a slightly larger area of 500 μm $\times$ 400 μm.

Due to the potentially long scanning times for motion and phase maps, it is important to limit the scope of acquisition to structures of interest. To do this, we

generally limit the field of view to the organ of Corti. Figure 4-5A is an example of an atypical extremely wide area scan. This scan took ~8 hours to acquire an area of 559 μm $\times$ 400 μm with a resolution of 1 μm $\times$ 1 μm. In this image, a large area of the apical temporal bone, as well as the organ of Corti can be seen.

Figure 4-5B tightens the focus of the same preparation to an area of 300 μm $\times$ 400 μm with the same resolution of 1 μm $\times$ 1 μm and a lower acquisition time of ~3 hours, a reduction of more than half in time. Acquiring images of just the organ of Corti is a technique used throughout this thesis to minimize time when producing high resolution motion and phase maps.

4.1.3.2 Optical axial spatial resolution

As described in chapter 2, the optical axial resolution of the system is limited by the smaller of either the depth of focus of the microscope objective or the coherence gating function defined by properties of the broadband light source. For the system utilized throughout this thesis, the full width at half maximum coherence gate depth is ~2 μm. Generally, high numerical aperture objectives with short working distances can be used in both *in vitro* and *in situ* experiments. However, *in vivo* experiments generally require longer working distances and smaller diameter objectives.

Figures 4-6A–C describe the image acquisition of an *in situ* guinea pig preparation. A high numerical aperture (0.8 NA) 40$\times$ water immersion objective with a working distance of ~2 mm focuses and collects light at a depth of focus of ~2 μm full width at half maximum depth. The objective is the limiting factor and the axial resolution is effectively ~2 μm.

Figures 4-6D–F describe the image acquisition of an *in vivo* guinea pig preparation. A low numerical aperture (0.13 NA) 10$\times$ air objective focuses and collects light. In this case, the depth of focus of the objective is much greater than the coherence gate, and the axial resolution is effectively limited by the coherence gate.

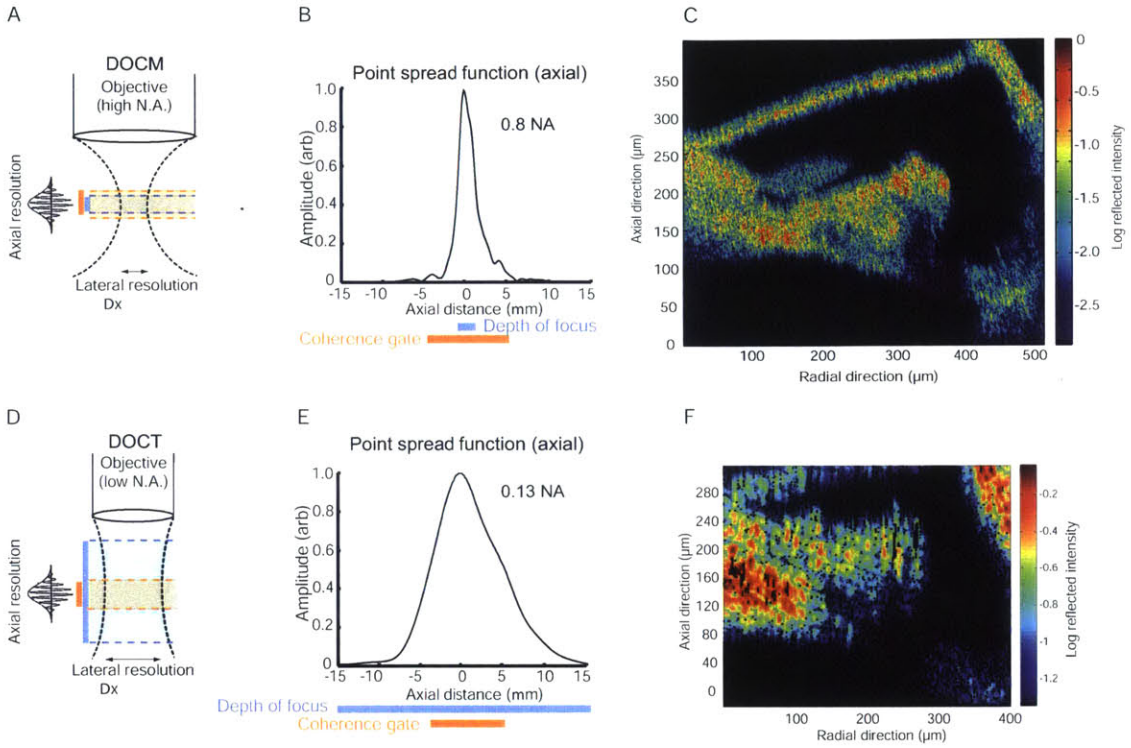

Figure 4-6: Low NA 10*times* air objective imaging vs High NA 40 × water immersion objective imaging. (A) Schematic diagram of DOCM setup with high NA objective highlighting small depth of focus (blue), coherence gate (orange), and lateral resolution (arrows) (B) High NA DOCM axial point spread function determined by depth of focus (blue). (C) *In situ* guinea pig apical scan with 1 μm × 1 μm resolution using a 40× water immersion objective. (D) Schematic diagram of DOCM setup with low NA objective highlighting large depth of focus (blue), coherence gate (orange), and lateral resolution (arrows). (E) Low NA DOCT axial point spread function determined by coherence gate (orange).(F) *In vivo* guinea pig (different preparation than A) apical scan with 2 μm × 2 μm resolution using a 10× air objective.

4.2 Results and Discussion

4.2.1 *In situ* apical Mongolian gerbil

Six Mongolian gerbil preparations are shown here to point out similarities and differences across preparations.

Three representative preparations (G330, G331, and G333) are shown in figure 4-7 along with identifying outlines and labels. Structural landmarks include Reissner's membrane, the tectorial membrane, three prominent outer hair cells, and the basilar

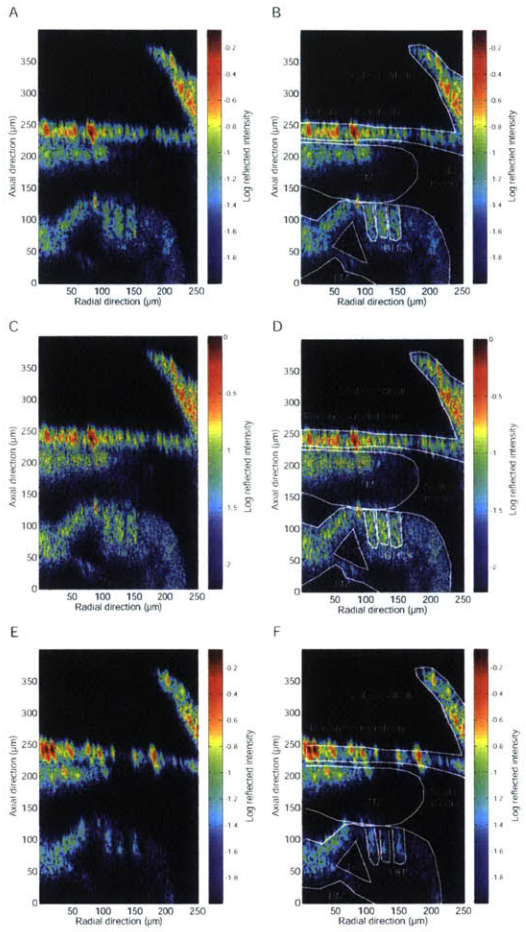

Figure 4-7: Three *in situ* Mongolian gerbil apical cross-sections and identifying labels and outlines taken with a 40× water immersion objective with 1 μm×1 μm resolution. Visible structures include Reissner's membrane, the tectorial membrane (TM), three prominent outer hair cells (OHCs), and the basilar membrane (BM). Fluid spaces include scala vestibuli, scala media, and the tunnel of Corti. (A–B) G330 (C–D) G333 (E–F) G331.

membrane. The fluid spaces of scala vestibuli, scala media, scala tympani, and the tunnel of Corti are discernable. Reissner's membrane, which provides a barrier between the high sodium concentration perilymph in scala vestibuli and high potassium concentration endolymph in scala media, appears to be intact. The tectorial membrane appears to occupy a large area from just under Reissner's membrane down to the reticular lamina.

Figure 4-8 shows two preparations (G518 and G6624) in which Reissner's membrane does not appear to stretch across to the lateral bony wall. Both preparations

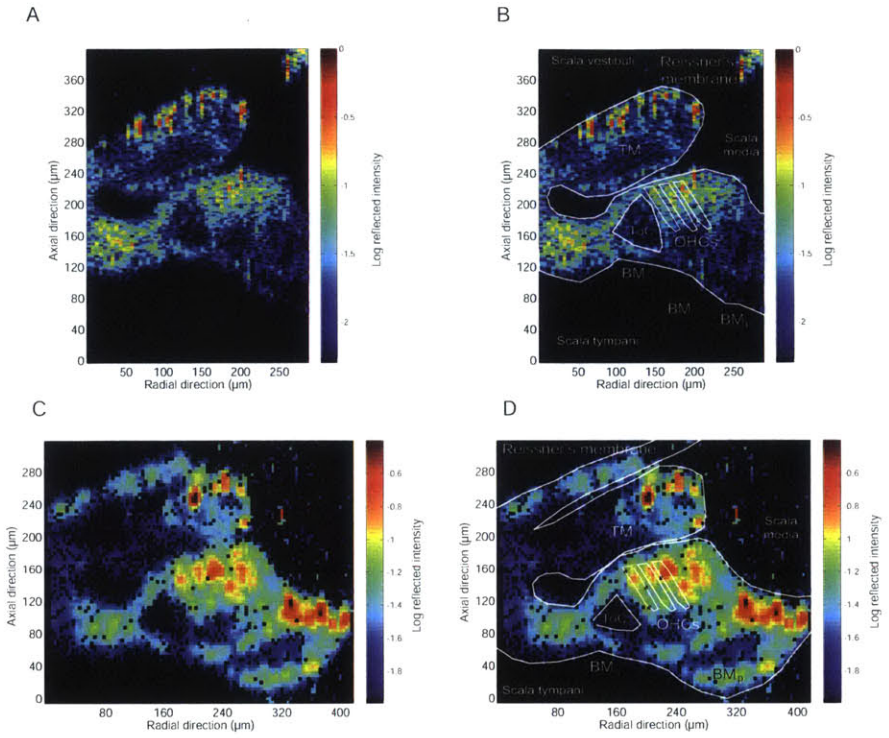

Figure 4-8: Two *in situ* Mongolian gerbil apical cross-sections with damaged Reissner's membranes. Both preparations have identifying labels and outlines, and were taken with a 40× water immersion objective. Visible structures include Reissner's membrane, the tectorial membrane (TM), three prominent outer hair cells (OHCs), and the basilar membrane (BM). The arcuate (BM_a) and pectinate (BM_p) zones of the basilar membrane are visibile in these preparations. Fluid spaces include scala vestibuli, scala media, scala tympani, and the tunnel of Corti. (A–B) G518 taken with 5 μm×2 μm resolution (C–D) G6624 taken with 4 μm×4 μm resolution

exhibit an abnormal brightness on the top and marginal edge of the tectorial membrane (10× brighter than other preps), suggesting that perhaps Reissner's membrane has torn, and is draped along the top edge of the tectorial membrane. The tectorial membrane shown in figure 4-8A has a large void in its center. In figure 4-8C & D, the pectinate zone of the basilar membrane is visible. There is a large void in the center of the pectinate zone of the basilar membrane.

Figure 4-9 shows low and high resolution images of a single gerbil preparation (G6039). The low resolution image took ~9 minutes to acquire, while the high resolution image took ~4.5 hours. In this preparation, Reissner's membrane appears to be intact, and the pectinate region of the basilar membrane is visible. Each has a large

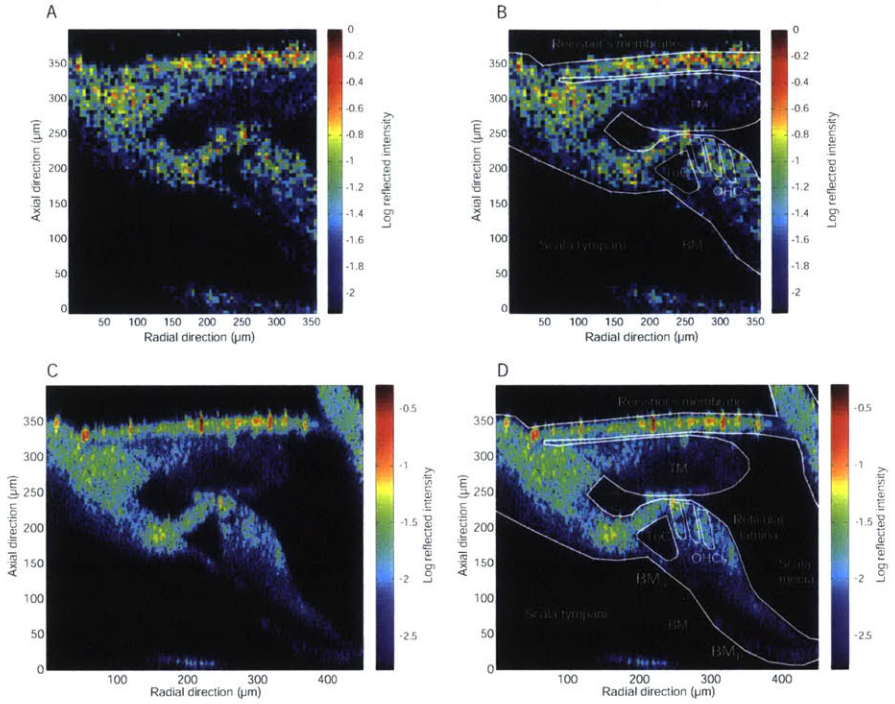

Figure 4-9: Low and high resolution *In situ* Mongolian gerbil apical cross-section (G6039) and identifying labels and outlines taken with a 40× water immersion objective. Visible structures include Reissner's membrane, the tectorial membrane (TM), three prominent outer hair cells (OHCs), and the basilar membrane (BM). The arcuate (BM_a) and pectinate (BM_p) zones of the basilar membrane are visibile in these preparations. Fluid spaces include the inner sulcus, scala vestibuli, scala media, scala tympani, and the tunnel of Corti.(A–B) Low resolution image: 5 μm×5 μm resolution (C–D) High resolution image: 1 μm×1 μm resolution

void in the center as seen in previous preparations. In this preparation, the tectorial membrane and reticular lamina do not appear to be in as close contact as those from previous preparations.

In all preparations, the fluid spaces including the tunnel of Corti and the inner sulcus are easily identified. In 5 of the 6 preparations shown here, the regions of the IHC and OHCs scatter more than the basilar membrane. In all images where the basilar membrane region is included, the arcuate and pectinate regions are easily discernable. The center of the pectinate zone shows less scattering than its surface. This could represent light scattering from structural collagen fibers near its surface.

Similarly, the center of the tectorial membrane has less scattering than its surface. This could represent scattering from a structural element about its surface such as

Distance from base	This study (G6039) 10±0.25 mm	Edge et.al. (9.8 - 10.8 mm)
Area (μm^2)		
BM (A)	6803	8225±537
TM (B)	15221	10160±573
OC (C)	14729	19733±1487
Distance (μm)		
BM (radial) (a)	227.8	207.3±2.5
TM (radial) (b)	231.3	213.7±5.1
IP (height) (c)	64.1	76.3±2.5
OP (height) (d)	84.3	110.3±0.6
ISS (height) (e)	41.9	53±4.6
Thickness (μm)		
BM (f)	46.0	55.3±3.2
TM (g)	80.5	49.7±6.6
Angles (°)		
TM/OP (α)	83.9	110±5
RL/BM (β)	1.21	21±6
RM/TM (γ)	Parallel	9.3±5.1

Table 4.1: Mongolian gerbil (G6039) apical measurements compared to Edge et. al. [26]. Measured structures include the basilar membrane (BM), the tectorial membrane (TM), organ of Corti (OP), inner pillar (IP) and outer pillar (OP) cells, inner sulcus (ISS) region, and reticular lamina (RL).

the covering net and dense fibrillar structure. The center of the TM is striated sheet matrix (Richardson) which could appear as a void of light scatterers to this reflected scattered light measurement technique.

Table 4.1 compares apical cochlear areas and dimensions from this study (G6039) to those taken by Edge et. al. [26]. Figure 4-10A shows an image of an apical section of a hemicochlea preparation from Edge et. al. This preparation is 9.8–10.8 mm from the base and is bathed in high sodium, low calcium artificial perilymph.

Location along the apex, as well as animal specific differences can contribute to general size differences in cross-sectional measurements. What is interesting in this comparison is that the tectorial membrane from this study has a much larger area when compared with [26], while the organ of Corti and associated dimensions (inner and outer pillar cell heights, etc.) are smaller. Additionally, the pectinate region of

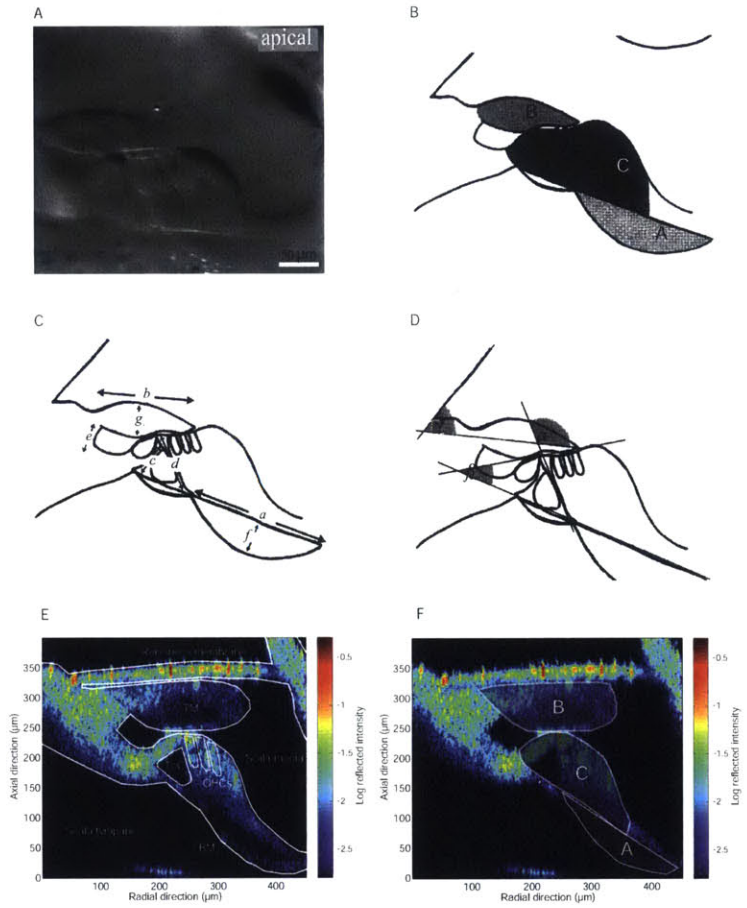

Figure 4-10: Comparison of anatomy in the *in situ* Mongolian gerbil apex. (A) Cross-section of the apical Mongolian gerbil hemi-cochlea from Edge et. al (9.8–10.8mm from the base) [26]. (B) Diagram of structures for which area is calculated (A: basilar membrane, B: tectorial membrane, C: organ of Corti). [26] (C). Diagram of widths, lengths, and thicknesses (a:basilar membrane (radial), b: tectorial membrane (radial), c: inner pillar (height), d: outer pillar (height), e: inner sulcus (height), f: basilar membrane (height), g: tectorial membrane (height)). [26] (D) Diagram of angles (α: tectorial membrane to outer pillar, β: reticular lamina to basilar membrane, γ: Reissner's membrane to the tectorial membrane). [26] (E) G6039 (10 ± 0.25 mm from the base) with identifying labels (F) Areas used for comparison in table 4.1.

the basilar membrane from this study is longer and thinner than that of [26], and has an ultimately smaller area.

The fact that the tectorial membrane is bigger in this study, could be related to the perfusate of the experiments. This study used a high sodium, 100 μM Ca concentration perilymph bath to perfuse the temporal bone with the most immediate access through the optical access hole connecting to scala vestibuli. Reissner's membrane was never intentionally broken. Edge et. al. used a more physiological compatible 20 μM concentration of Ca, but the high sodium perfusate had direct access to all fluid regions. However, guinea pig and mice hemicochlear preparations shown below had similar measurements to those in this study, and perfusates were unchanged.

4.2.2 *In situ* apical mouse

Figures 4-11A–D show two apical *in situ* mouse preparations (M509 and M7407) and identifying labels. In each preparation, Reissner's membrane appears to be intact. The tectorial membrane appears to slope downward from Reissner's membrane to the reticular lamina. Hensen's cells appear to be adjacent to the bony wall, without a gap. Figure 4-11E is a basal and 4-11F apical turn in a mouse hemicochlea preparation from Keiler et. al. The basal hemicochlear turn shows the angle at which the mouse tectorial membrane slopes downwards towards the reticular lamina. The apical hemicochlear tectorial membrane image also is sloping downwards at a similar angle, but the image is rotated counter-clockwise as seen in the angle of the reticular lamina.

Table 4.2 compares mouse apical cross-sectional areas and dimensions from this study (M7407, figure 4-11D) to hemicochlear mouse measurements by Keiler et. al. [59] Figure 4-11F shows an image of an apical section of a hemicochlea preparation from Keiler et. al. This preparation is 0.97 mm from the apex and is bathed in high sodium, low calcium artificial perilymph. Measurements shown in table 4.2 have comparable values to apical mouse structural measurements made by [59].

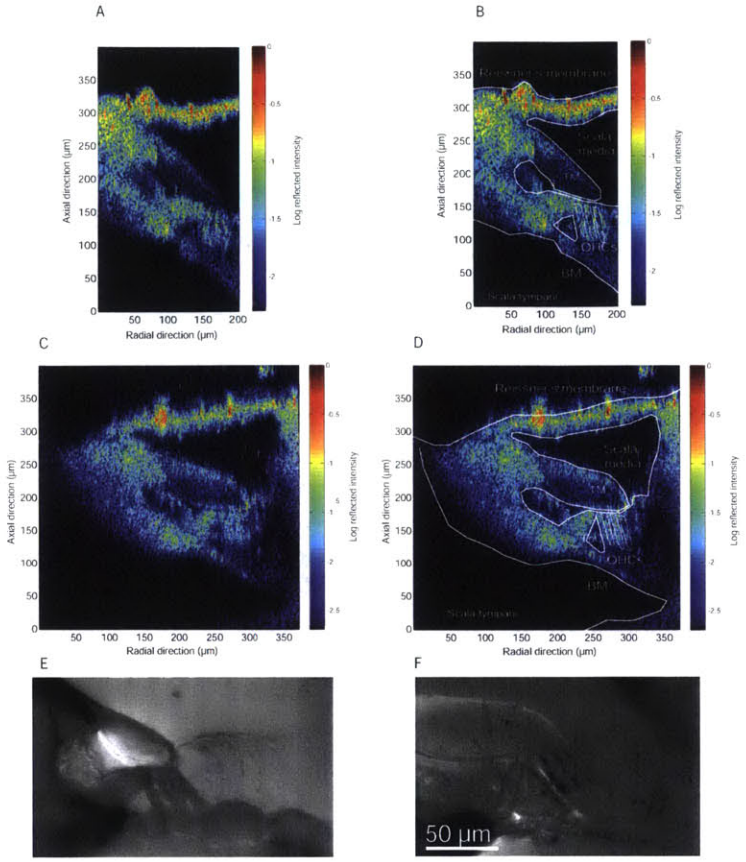

Figure 4-11: *In situ* mouse structural comparison. (A–B) 1 μm$\times$1 μm resolution image and labeling of M509 (0.9$\pm$0.25 mm from the apex). (C) 1 μm$\times$1 μm resolution image and labeling of M7407 (1.3$\pm$0.25 mm from the apex). Mice hemicochlea images from Keiler et. al. [59] in a (E) basal turn, and (F) apical turn.

4.2.3 *In situ* apical guinea pig

Figures 4-12A shows an *in situ* guinea pig preparation (GP6144) and 4-12B shows identifying labels. This is quite different than the gerbil and mouse *in situ* preparations shown earlier. The tectorial membrane appears to be quite distant from Reissner's membrane, and be parallel to the reticular lamina. Hensen's cells are much more prominent. The tunnel of Corti is not as easily discernable as that of the gerbil. The outer hair cells appear as one large mass as opposed to individual hair cell bodies. Figure 4-12C shows a guinea pig apical hemicochlear preparation from Teudt et. al. [109] for structural comparison.

Table 4.3 compares guinea pig apical cross-sectional areas and dimensions from

mm from apex	This study B6129F1/J 1.3±0.25	Keiler et.al. CBA/CaJ 0.97	Keiler et.al. C57BL/6J 0.97	Keiler et.al. 129/CD1 0.97	Keiler et.al. 129/SvEv 0.97
Width (μm)					
BM (az)	52.1	55.1±2.6	54.7±2.7	58.4±1.9	53.5±0.9
BM (pz)	110.8	108.5±7.1	118.0±8.1	115.2±2.1	110.5±2.5
TM	158.8	184.2±4.4	183.0±6.2	170.8±13.8	188.5±41.5
Height (μm)					
IP cell	49.0	49.2±1.9	50.5±1.5	45.3±0.8	50.8±1.0
OP cell	62.4	53.4±2.4	61.8±1.8	64.7±0.5	65.2±2.3
Thickness (μm)					
TM	58.2	54.3±4.0	50.0±2.3	45.3±3.1	49.8±5.0
Area (μm^2)					
TM	6275	6622±413.3	6164±321.5	5422.5±447.1	7075.5±1160.5
OC	4185	3448±404.5	5065±791.1	3573.0±101.9	4172.0±286.9
ToC	828.6	801±149.5	939±51.0	631.5±42.5	833.3±95.8
Angle (°)					
RL/OP	72.7	63.0±3.9	58.3±0.6	53.3±6.7	69.5±2.4
OP/BM	51.4	66.8±3.7	51.6±0.7	48.0±2.0	50.5±0.9
IP/BM	86.9	59.0±6.5	68.8±5.0	83.3±3.3	72.8±4.3

Table 4.2: Mouse apical measurements (M7407) compared to Keiler et. al. [59]. Measured structures include the arcuate zone (az) and pectinate zone (pz) of the basilar membrane (BM), the tectorial membrane (TM), inner pillar (IP) and outer pillar (OP) cells, organ of Corti (OP), tunnel of Corti (ToC), and reticular lamina (RL).

this study (GP6144) to hemicochlear guinea pig measurements by Teudt et. al. Measurements from this study have comparable values to apical structural measurements made by [109] with the tectorial membrane exhibiting a very slightly larger area as measured by this study.

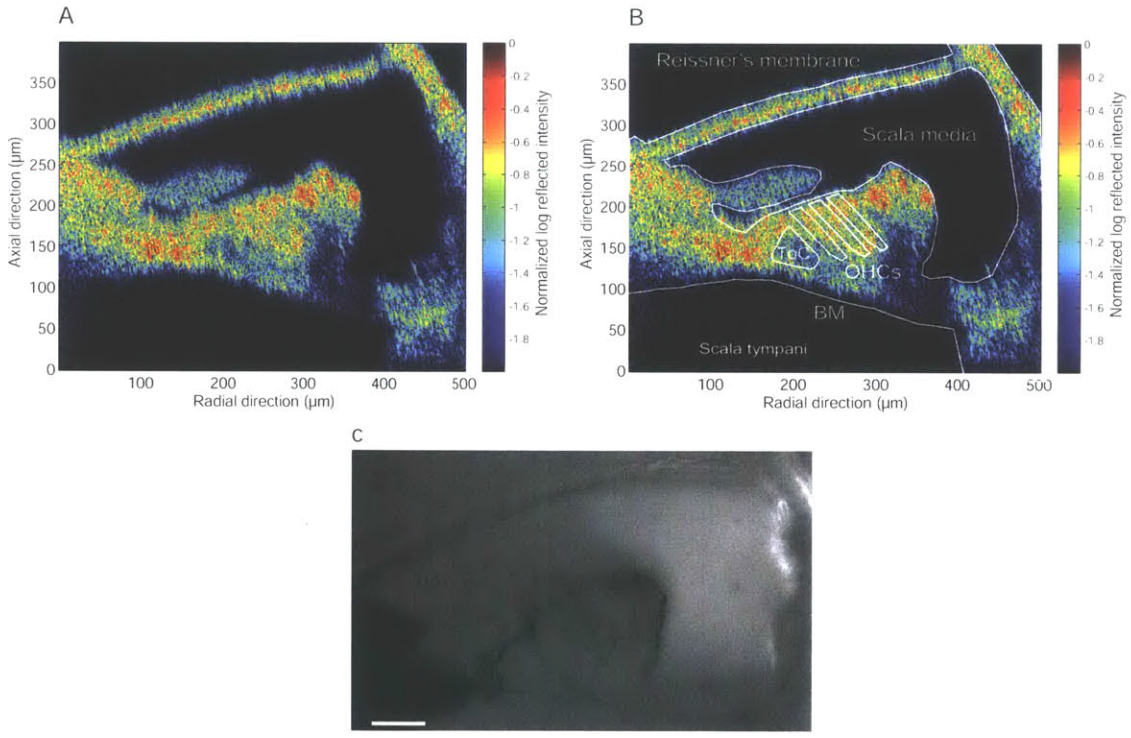

Figure 4-12: *In situ* guinea pig structural comparison. (A–B) 1 μm$\times$1 μm resolution image and labeling of GP6144 (0.8$\pm$0.2 mm from the apex). (C) Guinea pig apical hemicochlea image from Teudt et. al. [109]

	This study	Teudt et.al.	Teudt et.al.
mm from apex	0.8±0.2	0.89±0.02	2.35±0.09
Width (μm)			
Basilar membrane (az)	86	96±2.24	91±3.31
Basilar membrane (pz)	157	159±4.68	155±8.44
Basilar membrane (total)	243	255	247
Tectorial membrane	143	142±4.82	145±2.84
Height (μm)			
Inner pillar cell	62	66±1.96	65±1.71
Outer pillar cell	89	100±2.17	94±1.92
Thickness (μm)			
Tectorial membrane	35	34±1.27	34±0.80
Area (μm^2)			
Tectorial membrane	4246	3727±329	3858±98
Organ of Corti	21113	20941±854	21145±1077
Tunnel of Corti	1301	1534±164	1333±74

Table 4.3: Guinea pig apical measurements (GP6144) compared to Teudt et. al. [109]. Measured structures include the arcuate zone (az) and pectinate zone (pz) of the basilar membrane (BM), the tectorial membrane (TM), inner pillar (IP) and outer pillar (OP) cells, organ of Corti (OP), and the tunnel of Corti (ToC).

Chapter 5

Sound-induced axial motion in the apex of the mammalian inner ear

This chapter describes *in vivo* measurements of the axial component of acoustically driven motions of the apical region of the organ of Corti. Motions from *in vitro* preparations are used as a basis to understand the effect of active processes within the *in vivo* organ of Corti. *In vitro* experiments utilize Mongolian gerbils due to relative ease of access to the stapes, while *in vivo* experiments utilize guinea pigs due to relative ease of access to the apical turn. Axial displacement and phase maps are measured at or below the best frequency. Differential analysis allows for measurement of relative displacements and phase, internal to structures such as the organ of Corti.

5.1 Methods

5.1.1 *In vitro* preparation

5.1.1.1 Animal preparation

Cochleae were excised from guinea pigs, and gerbils. The animals were euthanized via CO_2 and decapitated. The bulla containing the cochlea was isolated and opened. Care was taken to preserve the stapes so that the cochlea could be stimulated by vibrating the stapes. The stapedius and tensor tympani tendons were precisely cut

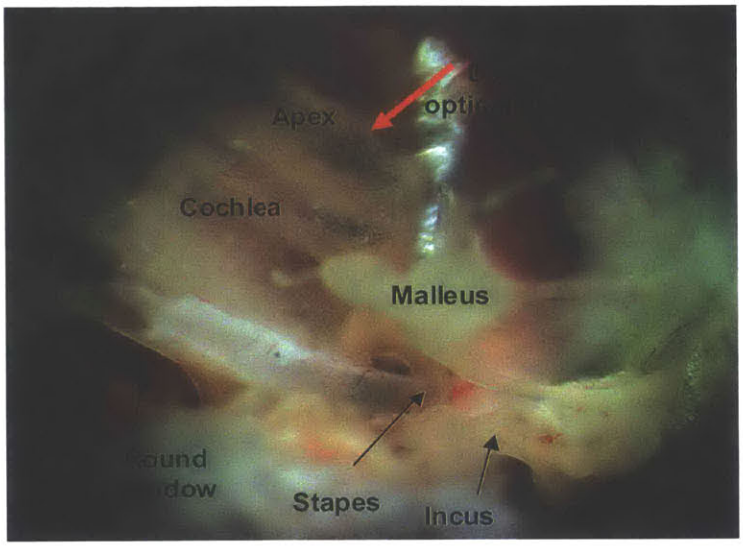

Figure 5-1: Inner ear of the Mongolian gerbil as seen through the opened bulla. The desired apical optical access is denoted with a red arrow. The three middle ear bones are labeled: malleus, incus, and stapes.

to avoid stapes damage upon incudo-stapedial joint and middle ear separation. The isolated cochlea, was fixed to a Petri dish using two-part dental cement (Durelon, ESPE Dental-Medizin GmbH) and bathed in a low Ca, low Cl, artificial perilymph (see sec. 5.1.1.2 for composition) with a pH of 7.30. A small hole (approximately 0.5 mm^2) was made in the temporal bone (figure 5-1) above the apical turn to allow for optical access. The care and use of animals in this study were approved by the Massachusetts Institute of Technology Committee on Animal Care.

5.1.1.2 Health

In vitro preparations are monitored for hair cell blebbing [3]. Isolated cochleae are bathed in an artificial perilymph solution with low calcium and chloride content to reduce hair cell blebbing. The pH of the artificial perilymph was maintained at 7.30 to match biological pH and consisted of 7 mM sodium chloride (NaCl), 163.4 mM sodium gluconate ($C_6H_{11}NaO_7$), 3 mM potassium chloride (KCl), 0.1 mM calcium chloride dihydrate ($CaCl_2{\cdot}2H_2O$), 0.1 mM magnesium chloride ($MgCl_2$), 2 mM sodium sulfate (Na_2SO_4), 0.5 mM sodium dihydrogen phosphate (NaH_2PO_4), 5 mM HEPES ($C_8H_{18}N_2O_4S$), 5 mM dextrose ($C_6H_{12}O_6$), and 4 mM L-glutamine ($H_2NCOCH_2CH_2CH(NH_2)CO_2H$).

5.1.1.3 Stapes-driven excitation

The oval window membrane and stapes footplate were visually verified to be intact after incudo-stapedial joint and middle ear separation. A piezoelectric driver consisting of a micromanipulator coupled to a titanium probe was used to deliver sinusoidal mechanical stimuli to the stapes. The tip of the probe was coated with dental cement and brought into gentle contact with the stapes as shown in figure 5-2. Voltages applied to the piezo were transduced to create piston-like motion of the stapes. The presence of pure stapes driven motion is verified using stroboscopic illumination under a computer microvision system. Voltages were adjusted for constant displacement as a function of frequency by recursive adjustment to output piezo voltage, while monitoring the displacement of the stapes. The resulting preparation is shown in figure 5-3.

Computer microvision combines video microscopy, stroboscopic illumination and computer vision algorithms to allow measurement of nanometer-scale motions of microscopic structures at audio frequencies [24, 4]. The system consists of a microscope (Zeiss Axioplan), digital camera (Dalsa CA-D7-1024A) and a custom built stimulus generator. Cochleae were imaged with a $40\times$, 0.8 NA water-immersion objective.

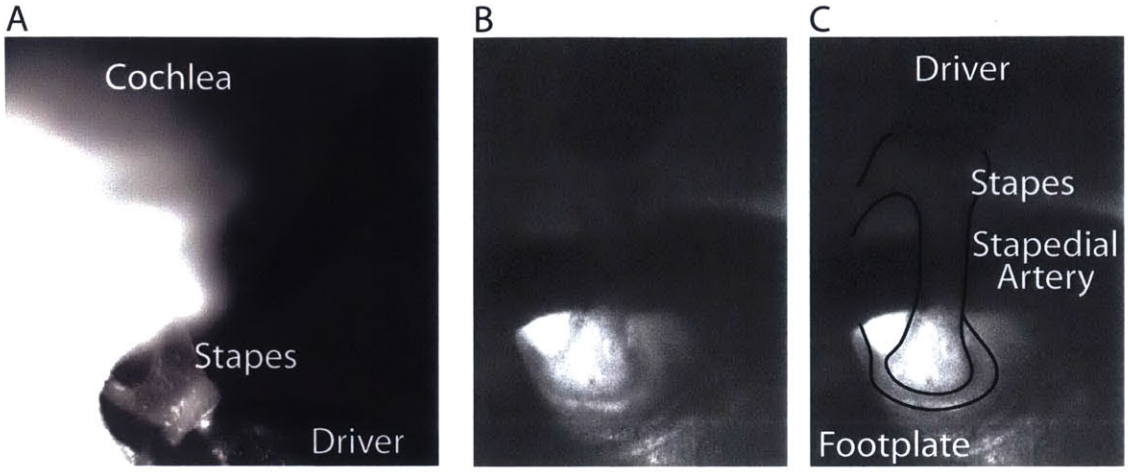

Figure 5-2: Stapes-driven *in vitro* stimulation. (A) Image of titanium driver in contact with the stapes. (B) A close view and (C) labeled view show the footplate and oval window membrane, as well as the quality of contact of the titanium driver with the stapes. The stapedial artery can be seen running through the center of the stapes.

5.1.1.4 DOCM optical methods

Axial measurements were performed using DOCM previously described in Chapter 2. Isolated cochleae were placed under a 40× water immersion objective (figure 5-3) on a lateral-axes motor driven scanning stage. The objective was mounted to a piezo electric driven axial stage. Together, these stages allowed for axial motions to be measured at each point throughout the isolated preparation. Cross-sectional scans are acquired by first moving the piezo driven axial stage (A-scan), followed by an increment in the lateral motor stages (B-scan), then repeating the process.

Light from the sample path of the DOCM system exits the objective and converges toward its focal point. As the objective moves axially (during the A-scan), the reference path moves with it, maintaining equal sample and reference path lengths. This allows continuous depth sectioning at the focal point of the objective. Since the depth of focus for the 40x water immersion objective is smaller than that of the interferometric coherence gate, optical transverse sectioning resolution is limited by the point spread function of the objective at approximately 2 μm. Depth sectioning is performed by passing the output sample path light through a hole made in the apical temporal bone. The light is scattered by Reissner's membrane and subsequent

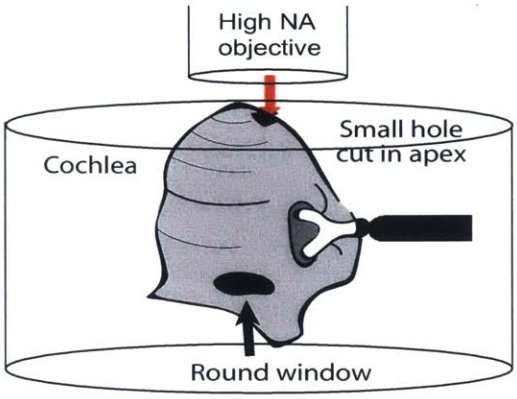

Figure 5-3: *In vitro* preparation. Cochleae are affixed using dental cement to a Petri dish. A high numerical aperture (NA) objective focuses through an approximate 0.5 mm apical hole. A piezoelectric titanium transducer creates sinusoidal stapes-induced cochlear excitation.

deeper tissues, a portion of which is recollected by the objective and mixed with the reference signal. This heterodyned interferometric signal is used to determine how much light is scattered at a given depth, as well as the direction and magnitude of motion.

5.1.2 *In vivo* preparation

5.1.2.1 Animal preparation

Anesthetized guinea pigs are prepared for *in vivo* measurements using procedures adapted from previous work [18, 91]. Guinea pigs are anesthetized using urethane or a combination of ketamine and sodium pentobarbital (initial dose of urethane 1.2g/kg or initial dose of ketamine at 40 mg/kg followed with sodium pentobarbital at 60 mg/kg) administered by intraperitoneal injection. Temperature is monitored via a rectal probe and maintained at 38° Celsius via a heating pad. Anesthetic depth is monitored via heart rate electrodes, respiratory rate, and periodic toe pinches to test for pedal withdrawal. Additional doses of urethane or sodium pentobarbital (0.6 g/kg or 10 mg/kg, respectively) are administered if anesthetic depth is determined to be insufficient. Lactated Ringer's solution (5 mL/kg) is administered subcutaneously every thirty minutes. A tracheotomy is performed, and the animal is artificially respirated

using a custom-built respirator. End-tidal CO_2 levels are monitored and maintained at a steady concentration by controlling respiration rate and intake volume.

After anesthetic induction, the dorsal skull is immobilized onto a location adjustable head holder. The pinna of one ear is removed and a wide area caudal to the pinna is shaved. Under a dissection microscope, the external carotid artery, internal carotid artery, sublingual artery, and lower alveolar artery are sutured on the side of the cochlea being measured. Figure 5-4 shows the preparation after the bulla is exposed. To provide DOCT optical access to the bulla for a large diameter conventional objective (figure 5-5), all blood flow in the area is stopped and half of the lower jaw is removed. Optical access to the apical turn is achieved by shaving the bone enclosing the bulla with a #15 scalpel blade. A small hole is made in the apical temporal bone using a #11 scalpel blade. The overall health of the cochlea is assessed using an ASSR protocol (section 5.1.2.4). At the end of the experiment, the animal is euthanized by anesthetic overdose (2.4 g/kg urethane or 120 mg/kg sodium pentobarbital).

5.1.2.2 DOCT Optical alignment

The animal is moved to the lateral motor driven stage for measurements. A $10\times$ 0.13 numerical aperture air objective is roughly positioned over the inner ear. Light from an optical fiber is brought in from the side to illuminate the organ of Corti. Visualization of the SLD focal point is achieved via a Charge-coupled device (CCD) camera (AVT Dolphin F145b 1938) coupled to the sample path using a dichroic mirror. The preparation is positioned under the focal point and the motors programmed to scan through the cross-section of interest (see chapter 2).

5.1.2.3 Acoustic sound delivery and calibration

Experiments are performed in a vibration and acoustic isolation chamber (Integrated Dynamics Engineering, Inc.) on an actively-stabilized vibration isolation table (Technical Manufacturing Corp.).

An acoustic delivery system [87] has been developed in consultation with John J. Rosowski and Michael Ravicz of the Eaton Peabody Laboratory at the Mas-

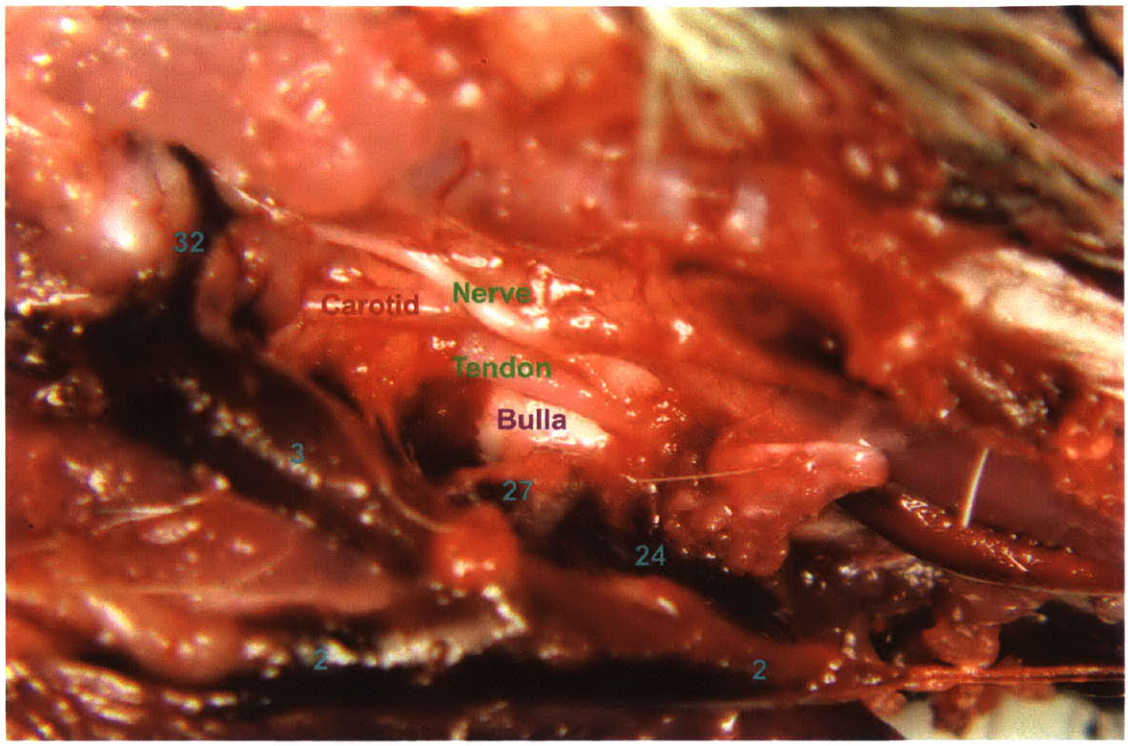

Figure 5-4: *In vivo* view of the bulla before surgical jaw removal. Labeled veins are the (2) linguofacial, (3) lingual, (24) masseteric, (27) communicating branch, and (32) lower alveolar veins. Identification of veins aided by [84]

sachusetts Eye and Ear Infirmary. The sound system consists of a signal processing unit (Tucker Davis Technologies), which includes a speaker driver and a multi-field magnetic speaker. Pure tone signals are delivered to the speaker using a waveform generator (Hewlett Packard 33120A). Tone pips for ASSR recordings are generated using a digital to analog converter PCI card (Interface Corporation PCI-3525). We developed a custom-made programmable passive attenuator to lower the amplitude of signals from the waveform generator by 20 or 40 dB, as necessary. The sound source is coupled to the ear canal using a brass tube secured using cyanoacrylate. A notch in the brass tube allows placement of a probe tube microphone to within 1 mm of the umbo. The probe tube microphone is custom-built using a microelectromechanical (MEMs) microphone (Knowles Acoustics, SPM0204UD5) coupled to a 10 mm tube using a plastic cone that minimizes reflections. The probe tube microphone is calibrated using a chamber that mimics the volume of the guinea pig middle ear space as

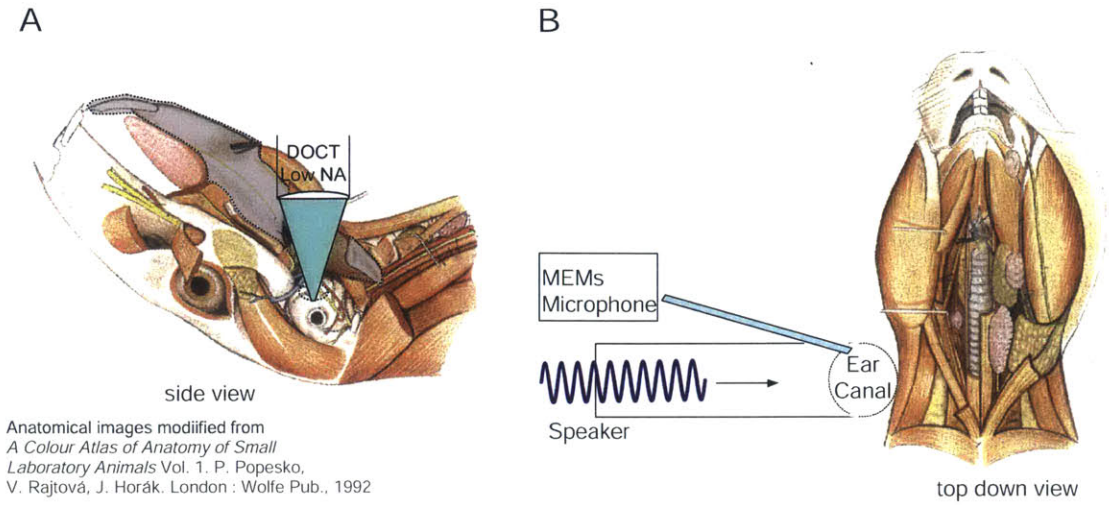

Figure 5-5: (A) A portion of the inferior mandible of the *in vivo* guinea pig is removed (grayed-out area) to provide anterior apical cochlear optical access for a low numerical aperture objective. (B) A Tygon tube is affixed to the outer ear canal for acoustic delivery. The sound pressure magnitude and phase at the tympanic membrane is monitored via a microelectromechanical microphone. Images modified from [84]

described in [87]. After positioning the probe tube close to the umbo, the hole in the brass tube is sealed off with petroleum jelly, and the stimulus is calibrated to produce constant sound pressures as a function of frequency near the ear canal. The probe tube microphone is then secured in this position to assess sound pressures during the experiment.

5.1.2.4 Health/Viability

Air in the acoustic isolation chamber is maintained at 37° Celsius to help stabilize body and bulla temperature (monitored with a rectal thermometer). The middle ear is periodically sprayed with saline to avoid drying out and changing the middle-ear response over the course of the experiment.

To monitor cochlear health in the apex, we generate an acoustic steady state response (ASSR) from the inferior colliculus by 40 Hz amplitude modulation of low frequency stimuli delivered into the ear canal. Neural response is recorded via differential auditory brainstem response needle electrodes placed at the vertex, ear and tail. The stimulus is delivered with a large repetition rate (typically 10 acquisitions

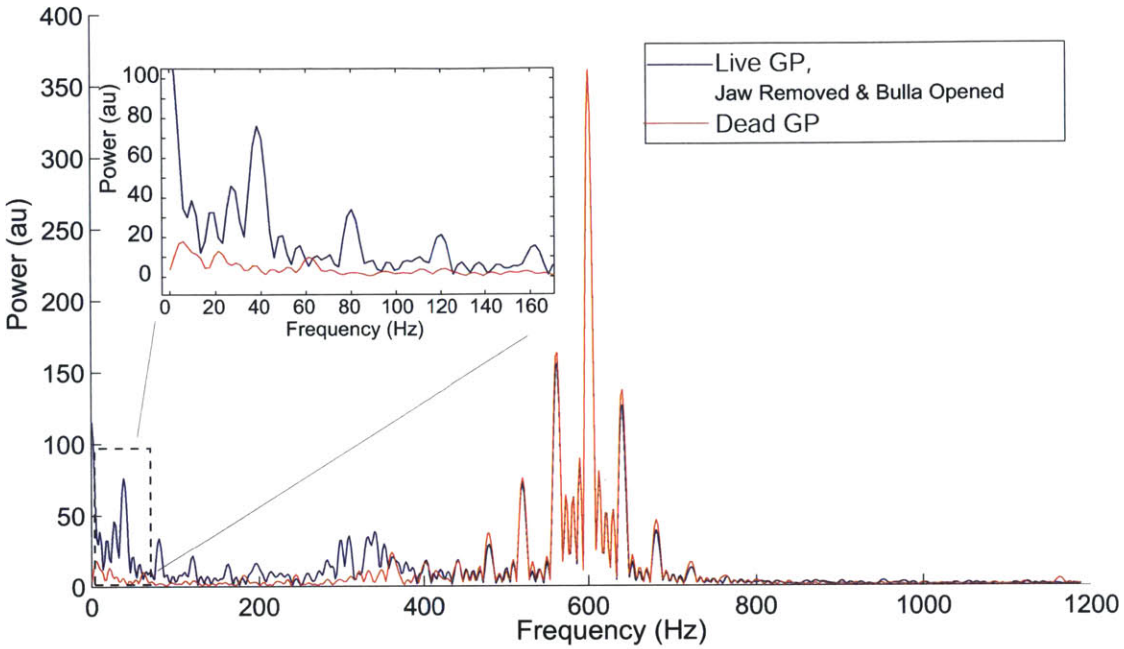

Figure 5-6: Example *in vivo* and post-mortem ASSR responses. Health of the cochlea was assessed with ASSR at low frequencies once the bulla was opened (blue) and upon euthanization (red). Neural responses were recorded in response to input stimulus tones at delivered at 600 Hz with 40 Hz modulations. Auditory brainstem ASSR responses occur at the modulation frequency region (see inset).

per second) and spectrally averaged over several acquisitions (typically $>$ 1500 sets). Figure 5-6 shows an example set of ASSR measurements. In healthy cochleae, the response contains a significant spectral component at the modulation frequency [108], which is absent or greatly diminished in animals with damaged hearing. ASSR measurements are typically conducted at the beginning, middle, and end of study (post-euthanasia). ASSR responses are very sensitive to even small changes in cochlear sensitivity. We found that altering the chamber temperature by as little as a few degrees changes the ASSR by more than a factor of 2. The ASSR has been particularly useful for monitoring cochlear sensitivity during the most invasive surgical procedures (e.g., opening the bulla and removing the lower jaw bone).

5.2 Results

5.2.1 *In vitro* stapes induced apical mechanics

5.2.1.1 DOCM imaging and axial motion analysis

In vitro isolated cochleae placed under a 40× water immersion objective are first aligned via a low resolution scan. Figure 5-7A shows a low resolution 5 μm motor/piezo step size DOCM image of a 350 μm × 400 μm apical cochlear cross-section in a Mongolian gerbil. This low resolution scan took ~9 minutes to perform. Once desired positioning has been achieved, higher resolution scans can be performed. Figures 5-7B & C show high resolution 1 μm motor/piezo step size DOCM image and axial motion map of a 450 μm × 400 μm apical cross-section. The high resolution scan took approximately 4.5 hours to acquire.

The images shown in figure 5-7, are generated by processing the interferometric signal obtained at each point throughout the cross-section. Figure 5-8A is an unprocessed digitized interferometric signal acquired at a single point. For this particular experimental set, the analog interferometric signal was digitized by capturing 2^{17} samples at a rate of 5 Msamples/sec with a quantization step of 0.488 mV. An FFT of this signal, figure 5-8B, shows the 500 kHz interferometric signal as well as 500 kHz ± 450 Hz (stimulation frequency) sidebands (blue circles on x-axis denote 500 kHz ± 450 Hz). The height of the 500 kHz component is a measure of the intensity of reflected light and is used to build the images, while the sidebands contain information used to estimate the magnitude and phase of axial motion. The solid blue line in figure 5-9F is an extraction of the magnitude of axial motion obtained by demodulating the interferometric signal using a Hilbert transform and adjusting for the indices of refraction. The dashed red line is the sinusoidal motion fit obtained by performing a least squares fit on each cycle of the stimulation frequency and determining the complex average. The standard deviations of magnitude and phase can be computed using this method.

Through interferometric signal processing, the magnitude and phase of axial cochlear

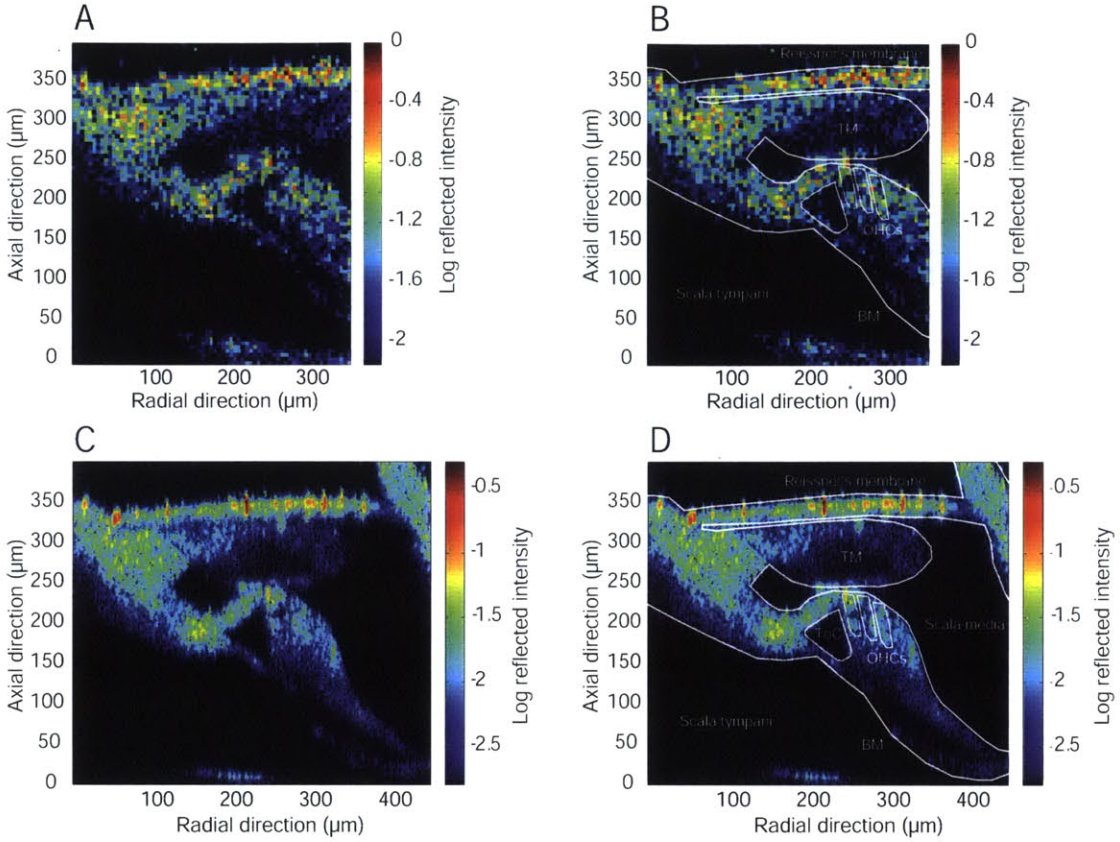

Figure 5-7: DOCM low resolution and high resolution images of an em in vitro Mongolian gerbil (G6039) on a logarithmic intensity scale. DOCM (40×, 0.8 NA) (A) low resolution 5 μm × 5 μm image and (C) high resolution 1 μm × 1 μm image, with (B & D) labels of structures and fluid spaces of the organ of Corti. TM = tectorial membrane, OHCs = outer hair cells, BM = basilar membrane.

motion relative to stapes stimulation can be characterized at each point throughout the cochlear cross-section. Figure 5-9 shows an *in vitro* DOCM image, axial motion, and stimulus-referenced phase map of an apical cross-section of the *in vitro* Mongolian gerbil cochlear partition (460 Hz characteristic place) in response to 450 Hz stapes stimulation at ~90 dB equivalent sound pressure level (SPL). The magnitude represented by the color bar in figure 5-9B describes the average peak-to-peak axial motion of an area set by the lateral and axial resolution limits (described in Chapter 2). When measured axial motion magnitudes are low, phase measurements appear random as seen in the left half of figure 5-9C. Increasing phase indicates a phase lead, while decreasing phase indicates a phase lag.

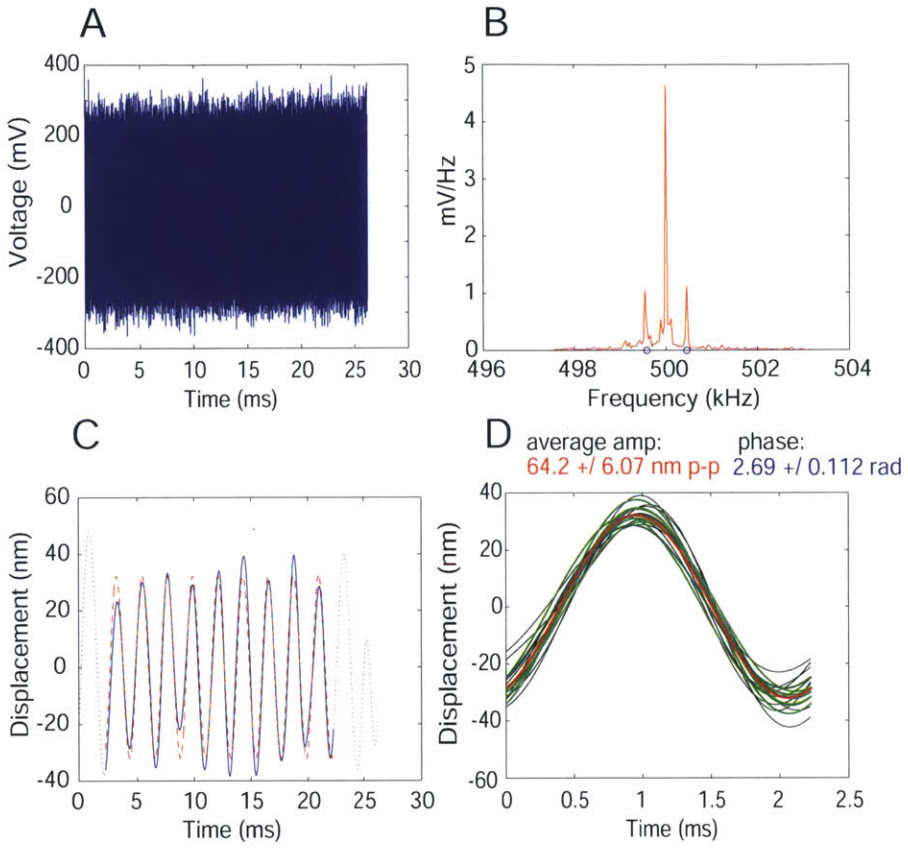

Figure 5-8: DOCM interferometric signal processing in the *in vitro* Mongolian gerbil (G6039) with ~90 dB equivalent sound pressure level (SPL) sinusoidal stapes stimulation at 450 Hz. (A) Photodetector interferometric signal acquired from 1 point (shown in next figure). (B) Spectral content of interferometric signal. (C) Axial motion (solid blue line) and fitted sinusoid (red dashed line) after Hilbert transform demodulation and signal processing. (D) Comparison of curve fitting across cycles. Measurement point illustrated in figure 5-9.

Figures 5-10, 5-11, and 5-12 show that axial motion magnitudes of the cochlear partition appear to increase and then decrease along the radial axis. Motion magnitudes go from near zero at modiolus to ~50 nm pk-pk near the third row of outer hair cells. The tectorial membrane also exhibits axial motion, but with smaller axial motion magnitudes (~25 nm pk-pk). Phase decreases as a function of outward radial position. An approximate $\frac{\pi}{4}$ axial phase lag of the TM referenced to the organ of Corti over the Hensen's cell region is observed.

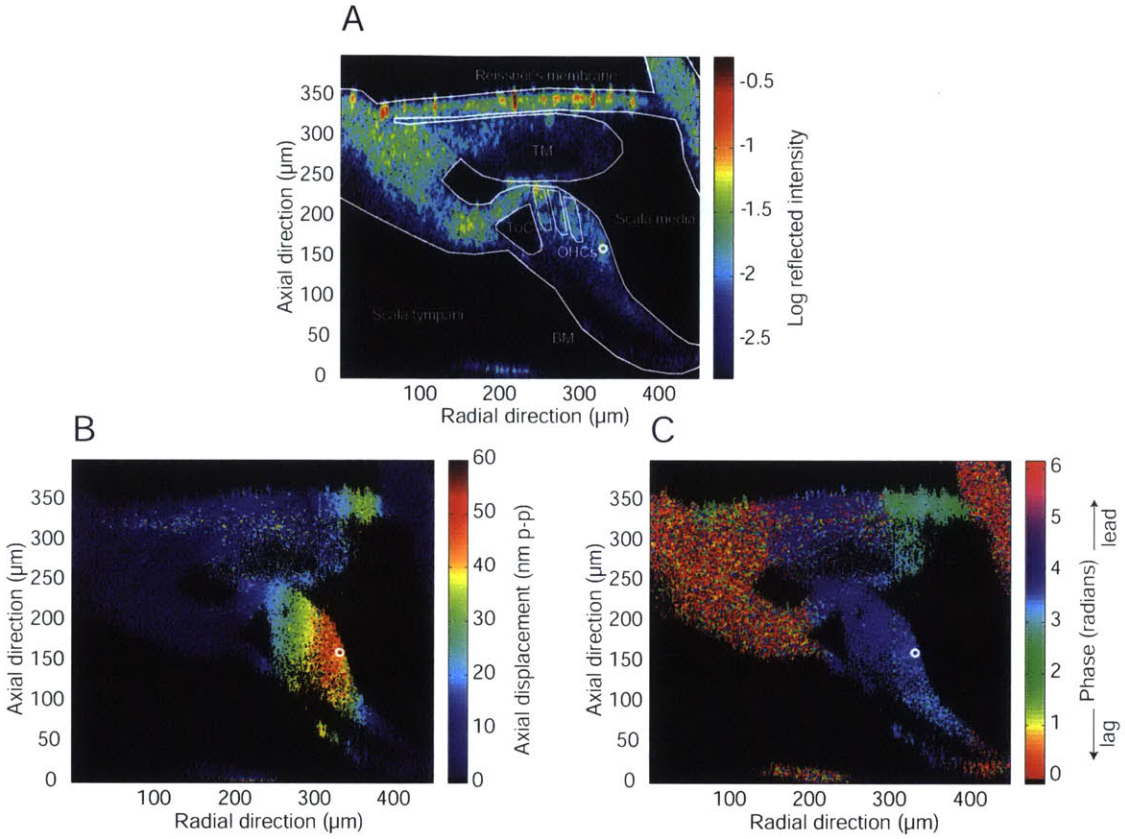

Figure 5-9: DOCM (A) image, (B) magnitude of axial motion map (peak-to-peak motion), and (C) stimulus-referenced phase map of an apical cross-section (460 Hz characteristic place) of the *in vitro* Mongolian gerbil (G6039) cochlear partition in response to ~90 dB equivalent sound pressure level (SPL) stapes stimulation at 450 Hz. Increasing phase indicates a phase lead, while decreasing phase indicates a phase lag. White circles denote location of interferometric signal acquisition shown in figure 5-8.

5.2.1.2 Differential analysis

Relative axial motion within the cochlear partition can be determined by referencing the complex magnitude and phase of measured absolute axial motion to that of a specific region. OHC somatic motility, if present, can be measured by referencing axial motion within the OHC region to that of a region of the organ of Corti beneath the OHC region along the long axis of the OHCs. In this study, the long axis of the OHCs is assumed to be parallel to the outer pillar cells, which is easily discernable along the lateral side of the tunnel of Corti. Relative complex motions of the OHC region referenced to the motion of the organ of Corti beneath the OHC region (along

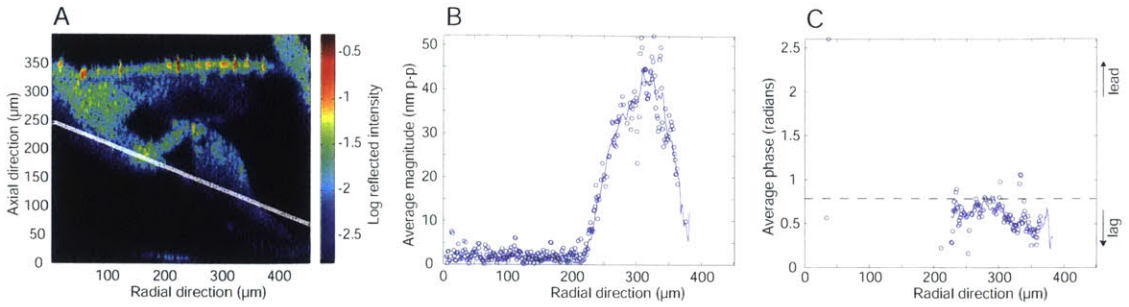

Figure 5-10: Apical cross-section (460 Hz characteristic place) of an *in vitro* Mongolian gerbil (G6039) cochlear partition with ~90 dB equivalent sound pressure level (SPL) sinusoidal stapes stimulation at 450 Hz. (A) A line running through the Deiter's cells is chosen as a function of radial distance and the (B) magnitude of axial motion and (C) stimulus-referenced phase profiles measured along that line. Increasing phase indicates a phase lead, while decreasing phase indicates a phase lag. Dashed line is at $\pi/4$ for reference.

the axis of the outer pillar cells) is referred to in this document as the *differential* magnitude and phase of axial motion.

Figure 5-13A and B show the measured absolute axial magnitude and phase of motion (seen previously in figure 5-9) of the apical turn of an *in vitro* Mongolian gerbil (G6039, ~460 Hz characteristic frequency) in response to ~90 dB equivalent SPL sinusoidal stapes stimulation at 450 Hz, below the characteristic frequency. To measure relative motion within the organ of Corti, a line that runs through the organ of Corti beneath the OHCs is chosen as a differential reference (white line in figure 5-13C), while an axis parallel to the outer pillar cells is selected as the axis of differential motion (red arrows in figure 5-13C). The magnitude of absolute axial motion along the reference line is shown in figure 5-13D, while the magnitude of the 6-point complex moving average is shown as a solid blue line. Figures 5-13E and F show the differential magnitude and phase of axial motion referenced to the 6-point complex average motion along the white line in figure 5-13C. Differential motion within the organ of Corti appears to be much smaller than absolute motion (figure 5-13E vs. A) when viewed on a similarly ranged axial displacement colorbar.

Reducing the range of the colorbar representing differential axial motion to 0–10 nm reveals relative motion within the organ of Corti, including the OHC region

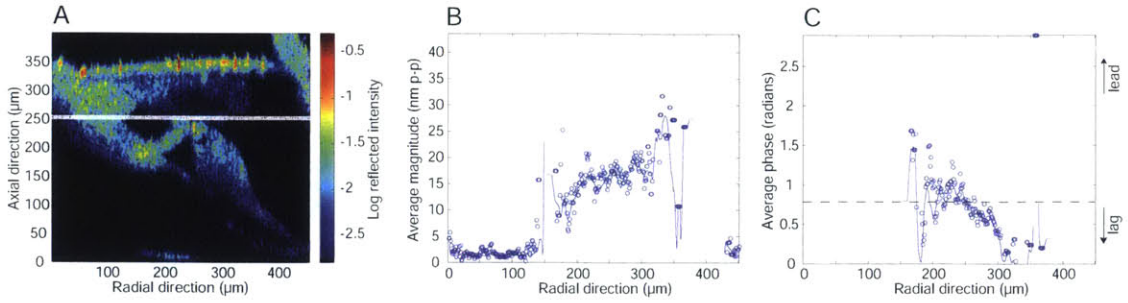

Figure 5-11: Apical cross-section (460 Hz characteristic place) of an *in vitro* Mongolian gerbil (G6039) cochlear partition with ~90 dB equivalent sound pressure level (SPL) sinusoidal stapes stimulation at 450 Hz. (A) A line running through the tectorial membrane is chosen as a function of radial distance and the (B) magnitude of axial motion and (C) stimulus-referenced phase profiles generated along that line. Increasing phase indicates a phase lead, while decreasing phase indicates a phase lag. Dashed line is at $\pi/4$ for reference.

(marked by a white outline in figure 5-14A, and a black outline in 5-14B). Relative motions of the OHC region are largest near the reticular lamina and reduce in magnitude downwards toward the reference point along the OHC long axis. A histogram of the magnitude of differential motion within the OHC region (figure 5-14C) shows a mean differential magnitude of ~5.6±1.9 nm p-p. Absolute motion in the OHC region had a mean of ~31.2±5.5 nm p-p. The ratio of differential motion to absolute motion of the organ of Corti is ~$\frac{1}{6}$. A histogram of differential phase within the OHC region is plotted in figure 5-14D and has a mean of ~3.0±0.28 radians. This represents counterphasic motion of the OHC region relative to the organ of Corti beneath the OHC region along the axis of the OHCs.

In an absolute reference frame, as the area of the organ of Corti beneath the OHC region moved upwards, the OHC region also moved upwards, but with less magnitude. Differential referencing of axial motion to the region of the organ of Corti beneath the OHC region, shows that as the area of the organ of Corti beneath the OHC region moved upwards, the OHC region moved downwards with the largest magnitude of contraction occurring at the reticular lamina in an *in vitro* preparation.

Figure 5-15 shows a different non-representative *in vitro* Mongolian gerbil preparation stimulated at the characteristic frequency. This preparation was unique to this

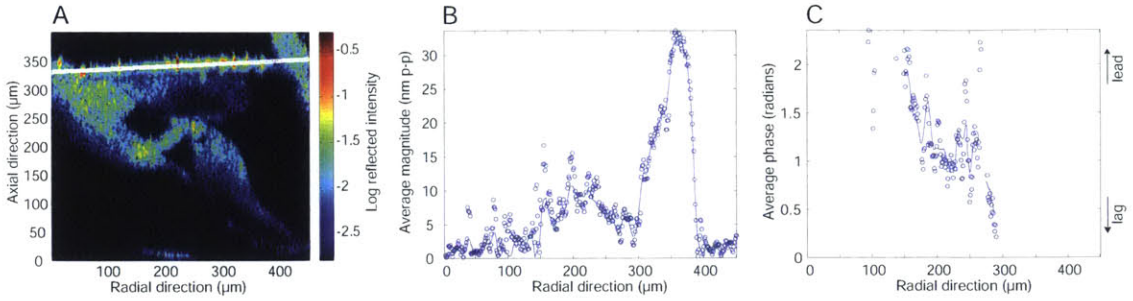

Figure 5-12: Apical cross-section (460 Hz characteristic place) of an *in vitro* Mongolian gerbil (G6039) cochlear partition with ~90 dB equivalent sound pressure level (SPL) sinusoidal stapes stimulation at 450 Hz. (A) A line running through the Reissner's membrane is chosen as a function of radial distance and the (B) magnitude of axial motion and (C) stimulus-referenced phase profiles generated along that line. Increasing phase indicates a phase lead, while decreasing phase indicates a phase lag.

study in that it appears that Reissner's membrane has torn and may have fallen onto the tectorial membrane. Additionally, the pectinate zone of the basilar membrane is parallel to the reticular lamina and Reissner's membrane, and does not show increasing axial motion as a function of radial position (figure 5-15B). Differential motion of the OHC region is not referenced to the basilar membrane, but to the region of the organ of Corti just beneath the OHC region in order to remove the pivot motion of the organ of Corti. Resulting differential motion has a mean of ~10.8±6.0 nm p-p compared to the mean absolute axial motion of ~95.0±23 nm p-p for a ratio of ~$\frac{1}{9}$ (figure 5-15G). The OHC region does not appear to be moving with a uniform differential phase (figure 5-15H). It should be noted that the image resolution was lower than the previously shown *in vitro* preparation (figure 5-13).

5.2.2 *In vivo* sound-induced apical mechanics

5.2.2.1 DOCT imaging and axial motion analysis

Objectives with long working distances and small diameters (i.e. low numerical aperture objectives) are necessary to measure within small spaces *in vivo*. As a result, *in vivo* image and axial motion maps have poorer axial resolution than those possible *in vitro*. Figure 5-16 contrasts a high resolution *in vitro* guinea pig image obtained

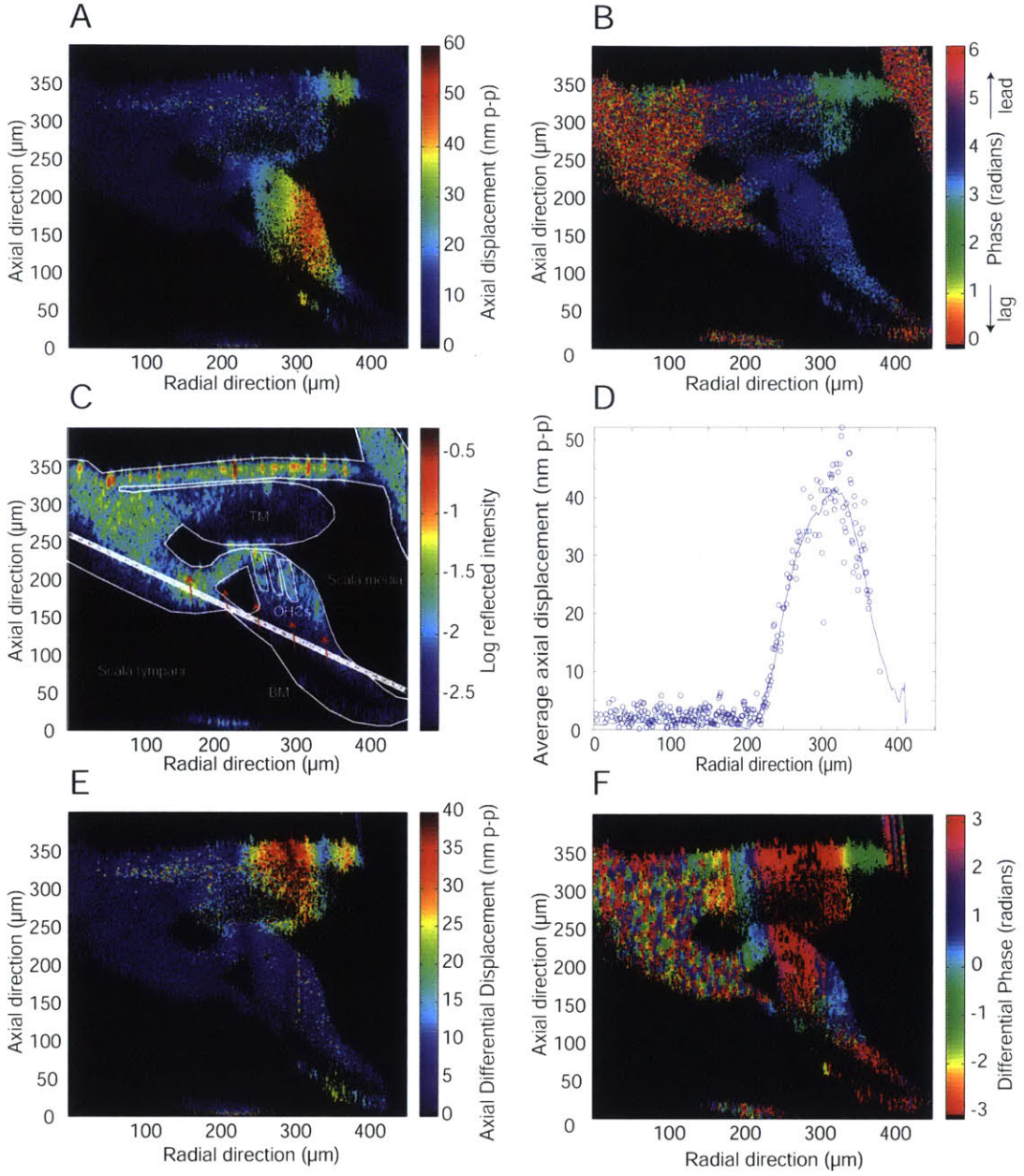

Figure 5-13: DOCM (40 ×, 0.8 NA, 1μm× 1μm resolution) (A) magnitude of axial motion map, (B) stimulus-referenced phase map, and (C) image in the apex (460 Hz characteristic frequency) of an *in vitro* Mongolian gerbil (G6039) in response to ~90 dB equivalent SPL sinusoidal stapes stimulation at 450 Hz. Differential complex axial motion, referenced to the average complex motion along the lower portion of the organ of Corti [white line in (C)], is found by subtracting that motion along lines that parallel the outer pillar cells (red arrows). (D) Magnitude of the complex axial motion along the reference line. The solid blue line represents the magnitude of a 6-point running complex average. (E) Magnitude of axial differential motion referenced to the lower portion of the organ of Corti [white line from (C)] with colorbar range of 0–40 nm p-p. (F) Axial differential phase referenced to the lower portion of the organ of Corti [white line from (C)]

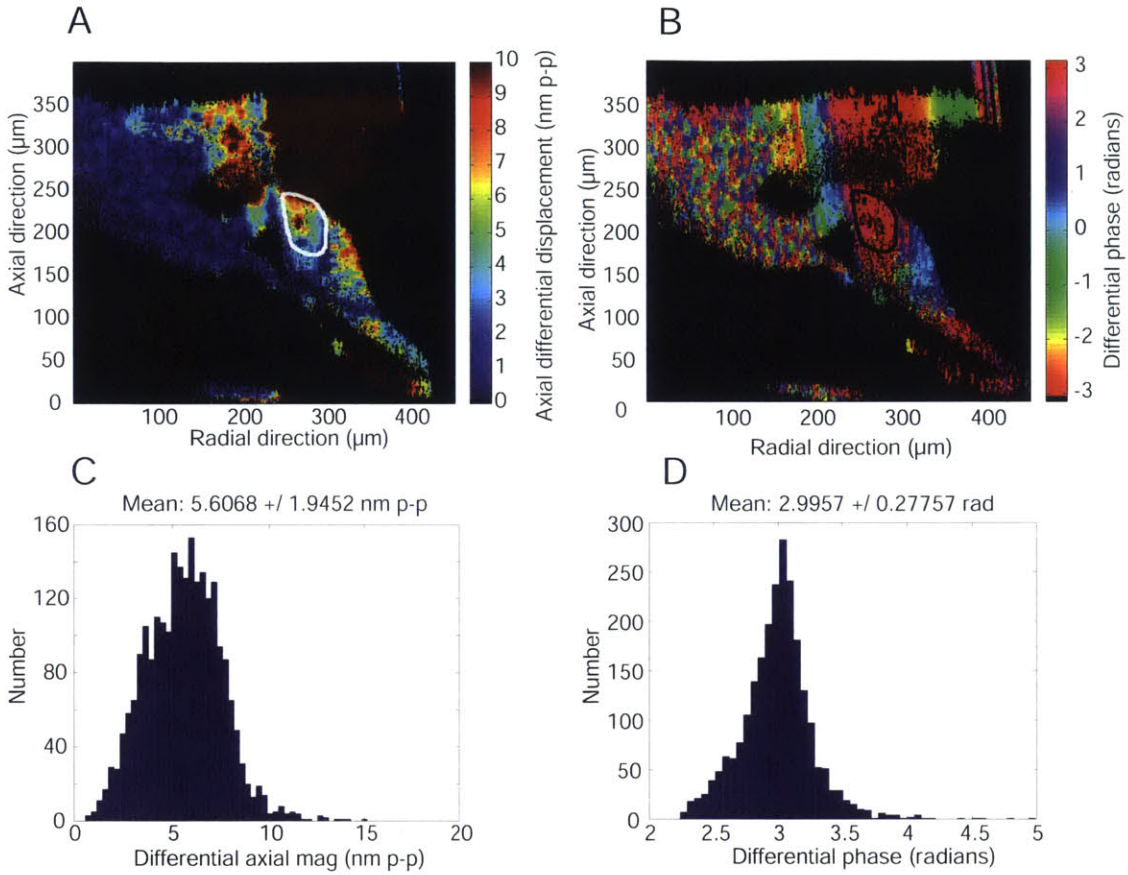

Figure 5-14: DOCM (40 ×, 0.8 NA, 1μm× 1μm resolution) measurements of an *in vitro* Mongolian gerbil (G6039) in response to ~90 dB equivalent SPL sinusoidal stapes stimulation at 450 Hz. (A) Magnitude of axial differential motion with colormap range of 0–10 nm p-p and (B) differential phase referenced to the lower portion of the organ of Corti [white line from figure 5-13(C)]. OHC region denoted by white and black circles in (A) and (B) respectively. (C) Histogram of differential magnitude of motion and (D) histogram of differential phase.

with DOCM (GP6144) to that of an *in vivo* guinea pig image obtained with DOCT (GP6756). The high resolution *in vitro* image has easily identifiable structures include Reissner's membrane, the tectorial membrane (TM), the outer hair cell (OHC) region, the basilar membrane (BM), the tunnel of Corti (ToC), and the Hensen's cells. The high resolution image serves as an anatomical atlas for identification of structures within the low resolution *in vivo* image (figure 5-16B).

A cross-sectional image of the apical turn (characteristic frequency ~200 Hz) of an *in vivo* guinea pig acoustically driven at the characteristic frequency with a ~70

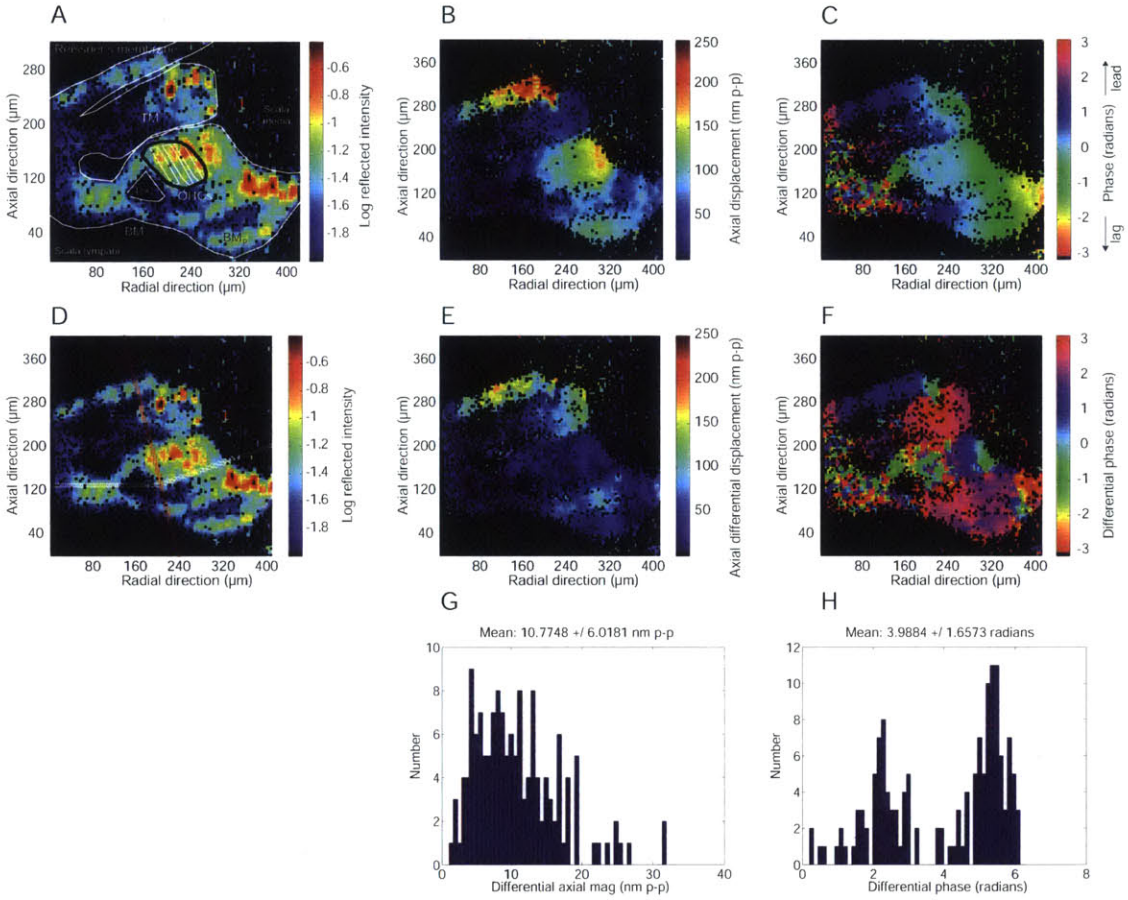

Figure 5-15: DOCM (40 ×, 0.8 NA, 4μm× 4μm resolution) (A) Image, (B) magnitude of axial motion map, (C) stimulus-referenced phase map in the apex (450 Hz characteristic frequency) of an *in vitro* Mongolian gerbil (G6627) in response to ~78 dB equivalent SPL sinusoidal stapes stimulation at 450 Hz. Differential motion is referenced to the average complex motion along the (D) lower portion of the organ of Corti (white line) along lines that parallel the outer pillar cells (red line). (E) Magnitude and (F) phase of axial differential motion referenced to the lower portion of the organ of Corti [white line from (D)]. Histograms in the region of the OHCs [black outline in (A)] of (G) differential magnitude of axial motion and (H) differential phase.

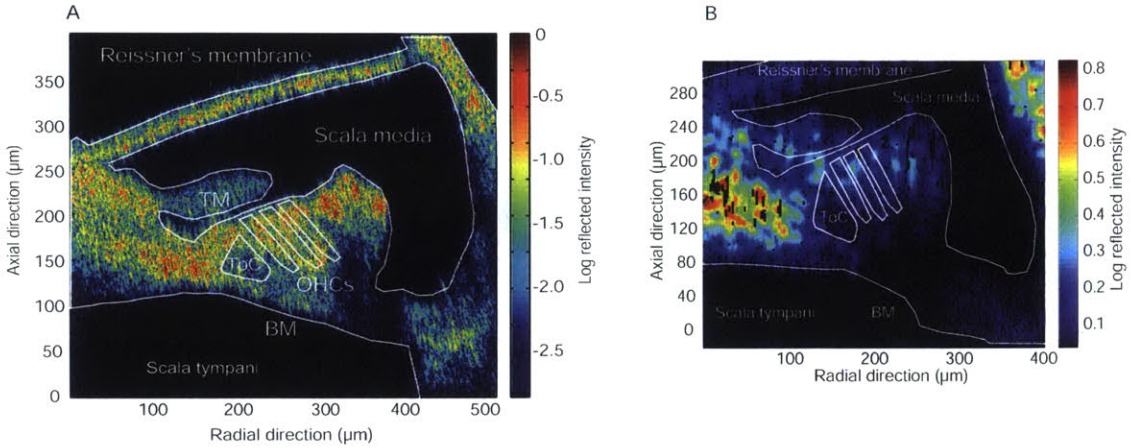

Figure 5-16: Comparison of high numerical aperture (NA) DOCM *in vitro* and low NA DOCT *in vivo* images of the apical organ of Corti in guinea pig. (A) 1 μm$\times$ 1μm DOCM image of the apical turn of an *in vitro* guinea pig (GP6144) acquired with a 40$\times$, 0.8 NA water immersion objective. (B) 2 μm$\times$ 2μm DOCT image of the apical turn (characteristic frequency ~200 Hz) of an *in vivo* guinea pig (GP6756) acquired with a 10$\times$, 0.13 NA air objective. Visible structures include Reissner's membrane, the tectorial membrane (TM), the outer hair cell (OHC) region, the basilar membrane (BM), and the tunnel of Corti (ToC).

dB SPL 200 Hz pure tone is shown in figure 5-17A. The image was acquired with a 0.13 numerical aperture air objective through a hole in the apical temporal bone. The axial motion magnitude increases and then decreases as a function of radial position. The cochlear partition exhibits uniform directionality of motion as shown by its near constant phase.

Image and motion maps are derived from signal processing the interferometric signal at each pixel. Figure 5-18 shows the interferometric signal (blue circles on x-axis denote 500 kHz $\pm$ 200 Hz), spectral content, axial motion and fit, and curve fitting for the 200 Hz stimulation frequency. Longer sampling times can improve motion resolution at low frequencies by capturing more displacement cycles.

5.2.2.2 Frequency-dependent motion analysis

Figure 5-19 shows the magnitude and phase of axial motion at three locations along the reticular lamina as a function of frequency in the *in vivo* guinea pig apex. The locations are labeled as 1, 2, and 3 in figure 5-17 and increase as a function of radial

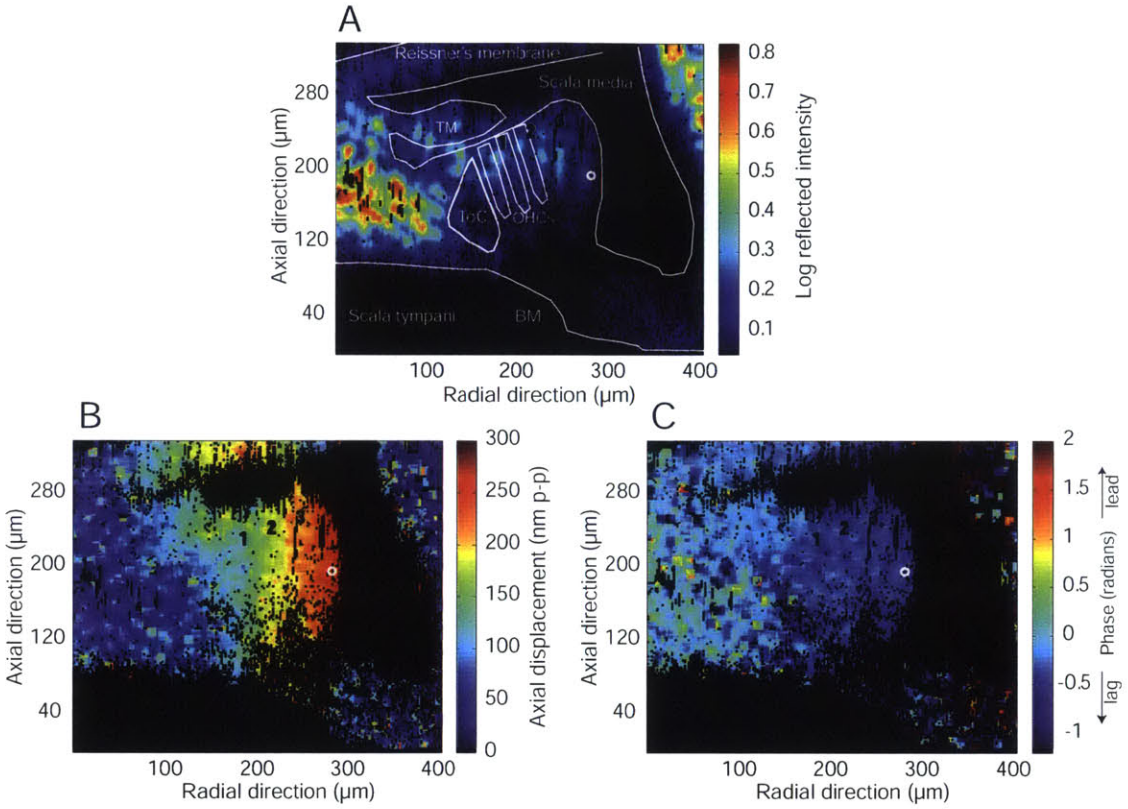

Figure 5-17: DOCT axial motion and stimulus-referenced phase maps of the apical turn (characteristic frequency ~200 Hz) of an *in vivo* guinea pig (GP6756). (A) OCT image of cochlear partition shows identifiable anatomical features: Reissner's membrane, tectorial membrane, basilar membrane (BM), outer hair cells (OHCs), and tunnel of Corti (ToC). (B) Magnitude of axial motion and (C) stimulus-referenced phase maps show relative motions of these cochlear structures in response to acoustic stimuli (~70 dB SPL at 200 Hz).

position from the modiolus. The sound level at the tympanic membrane is maintained at ~70 dB SPL as the frequency of stimulation is varied from 100 Hz to 1 kHz. The magnitude of axial motion increases as a function of radial position. At all radial positions the magnitude of axial motion peaks at ~200 Hz. This represents the best frequency for the apical cochlear cross-section location under test. The phase remains consistent for all three radial locations as a function of frequency.

Figure 5-20A shows the magnitude of axial motion at one position near the reticular lamina (labeled as location #1 in figure 5-17) as a function of sound pressure level. The sound level at the tympanic membrane was varied from 58 dB to 70 dB as the

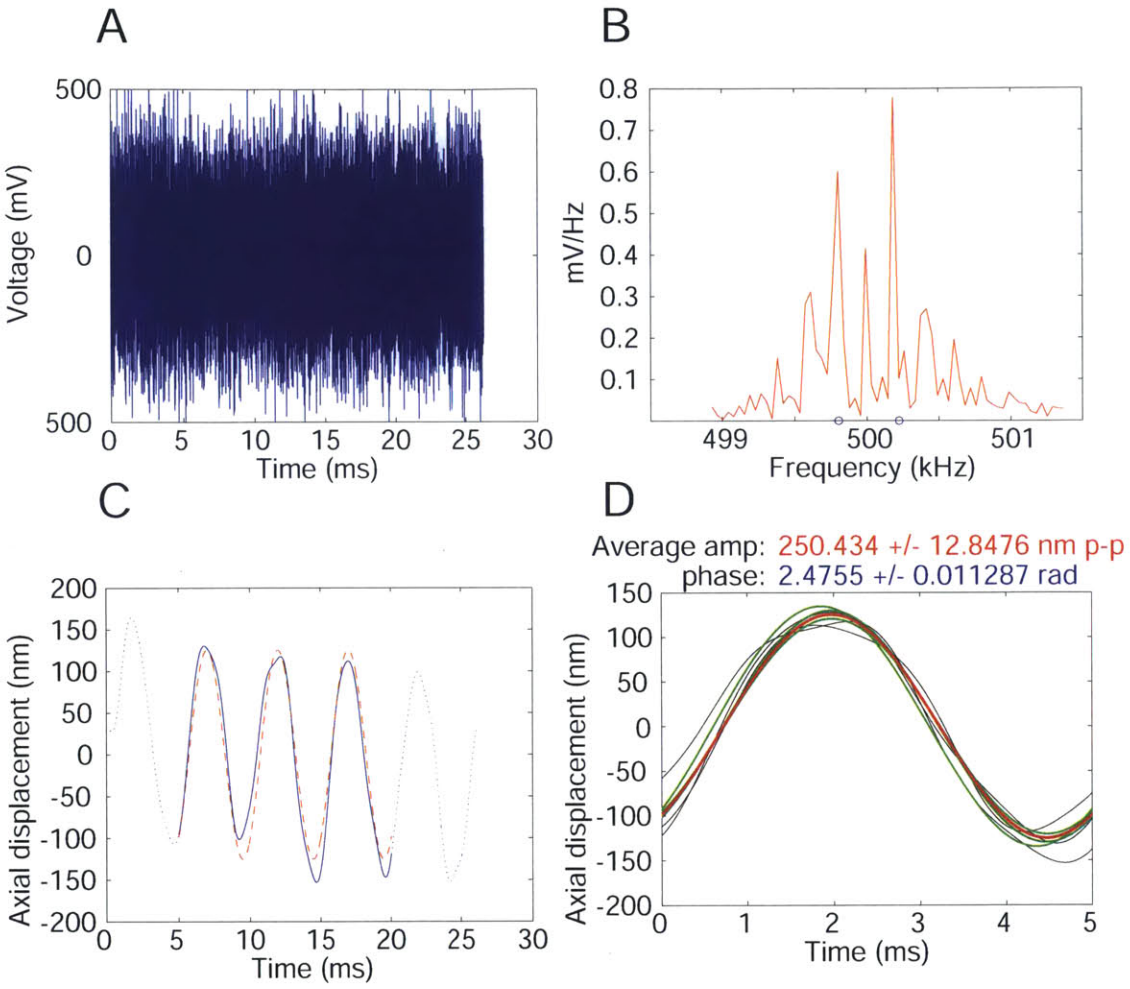

Figure 5-18: DOCM interferometric signal processing in the *in vivo* guinea pig (GP6756) with ~70 dB equivalent sound pressure level (SPL) sinusoidal stapes stimulation at 200 Hz. (A) Photodetector interferometric signal acquired from 1 point (shown in previous figure 5-17). (B) Spectral content of interferometric signal. Blue dots on x-axis denote 500 kHz ± 200 Hz. (C) Axial motion (solid blue line) and fitted sinusoid (red dashed line) after Hilbert transform demodulation and signal processing. (D) Cycle by cycle curve fitting (green curves) used to estimate magnitude and phase of axial sinusoidal motion (red curve) and associated error.

frequency of stimulation was varied from 100 Hz to 1 kHz. The magnitude of axial motion decreased with sound pressure level with peaks occurring at ~200 Hz. The phase as a function of frequency remains consistent with changes in sound pressure level.

Axial motions are scaled by sound pressure level to determine sensitivity and phase

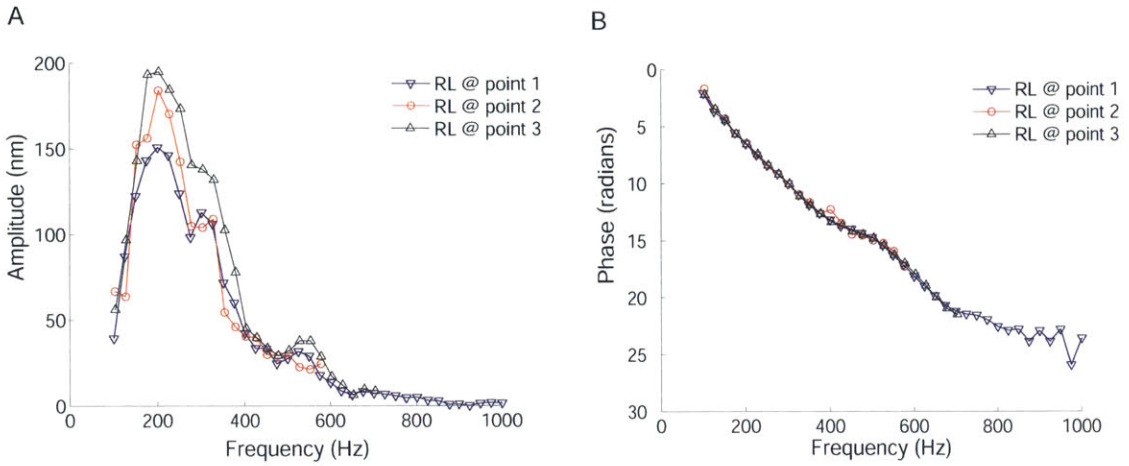

Figure 5-19: (A) Magnitude and (B) stimulus-referenced phase of axial motion as a function of frequency in the *in vivo* guinea pig (GP6756) apex (~200 Hz characteristic frequency) in response to ~70 dB equivalent sound pressure level (SPL) sinusoidal acoustic stimulation at 3 radially separated positions along reticular lamina. Positions are numbered in figure 5-17.

as a function of frequency in figure 5-21. Delivered sound pressures ranged from 58 dB to 70 dB SPL and peak sensitivity occurs at the best frequency, 200 Hz. There is a secondary maxima at ~525 Hz. Phase rolloff is constant with sound pressure level change.

5.2.2.3 Differential analysis

A line that runs through the lower portion of the organ of Corti is chosen as a differential reference (white line in figure 5-22C), while a line parallel to the outer pillar cells is selected as the axis of differential motion (red arrows in figure 5-22C). Figures 5-22A and B show the measured absolute magnitude and phase of axial motion. The magnitude of axial motion along the reference line is shown in figure 5-22D, and the solid blue line shows the magnitude of the 6-point complex moving average. Figures 5-13E and F show the differential motion and phase referenced to the complex axial motion along the white line in part (C).

Relative axial motions of up to ~60 nm are observed in the outer hair cell region referenced to the region of the organ of Corti beneath the OHCs (figure 5-23A. Mean differential OHC motion is 29.4±13.7 nm p-p compared to a mean of absolute motion

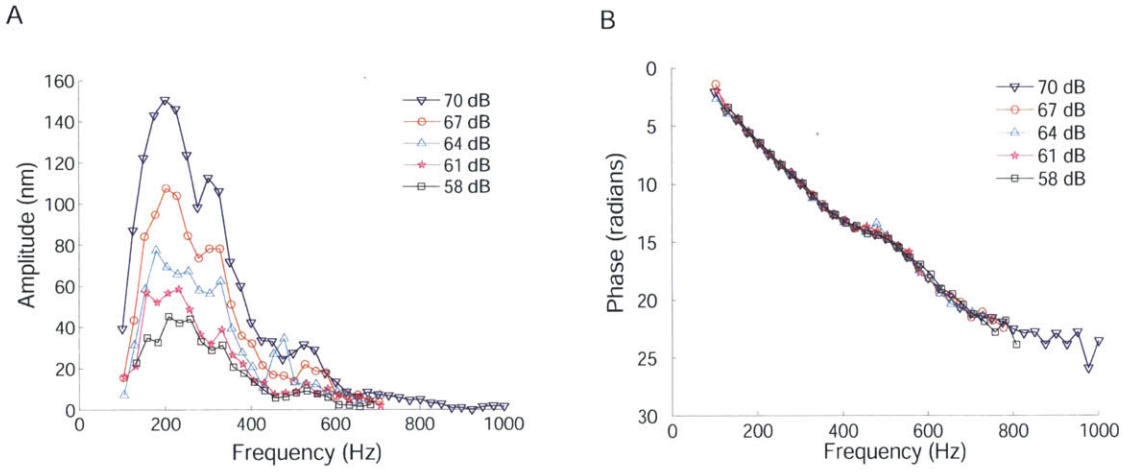

Figure 5-20: (A) Magnitude and (B) stimulus-referenced phase of axial motion as a function of frequency in the *in vivo* guinea pig (GP6756) apex (~200 Hz characteristic frequency) in response to ~70 dB equivalent sound pressure level (SPL) sinusoidal acoustic stimulation at one point near the reticular lamina (labeled as #1 in figure 5-17.

of 131.0±15.0 nm p-p for a ratio of differential motion to absolute motion of ~$\frac{1}{4}$. Phase of the axial differential motion of the OHC region had a mean of ~2.94±0.39 radians, indicating counterphasic motion of the OHC region relative to the organ of Corti beneath the OHC region along the axis of the OHCs.

In an absolute reference frame, as the area of the organ of Corti beneath the OHC region moved upwards, the OHC region also moved upwards, but with less magnitude. Differential referencing of axial motion to the region of the organ of Corti beneath the OHC region, shows that as the area of the organ of Corti beneath the OHC region moved upwards, the OHC region moved downwards with the largest magnitude of contraction occurring at the reticular lamina in an *in vitro* preparation.

5.2.2.4 Post-mortem axial motion and differential analysis

Figures 5-24A-C show image, magnitude of axial motion, and phase maps for the same *in vivo* guinea pig preparation as seen in figure 5-17, but stimulated at a level 9 dB lower. The acquisition of figure 5-24 started 9 minutes after the completed acquisition seen in figure 5-17. The heart rate of the animal gradually decreased and death occurred 36 minutes into acquisition. The scan was allowed to continue and

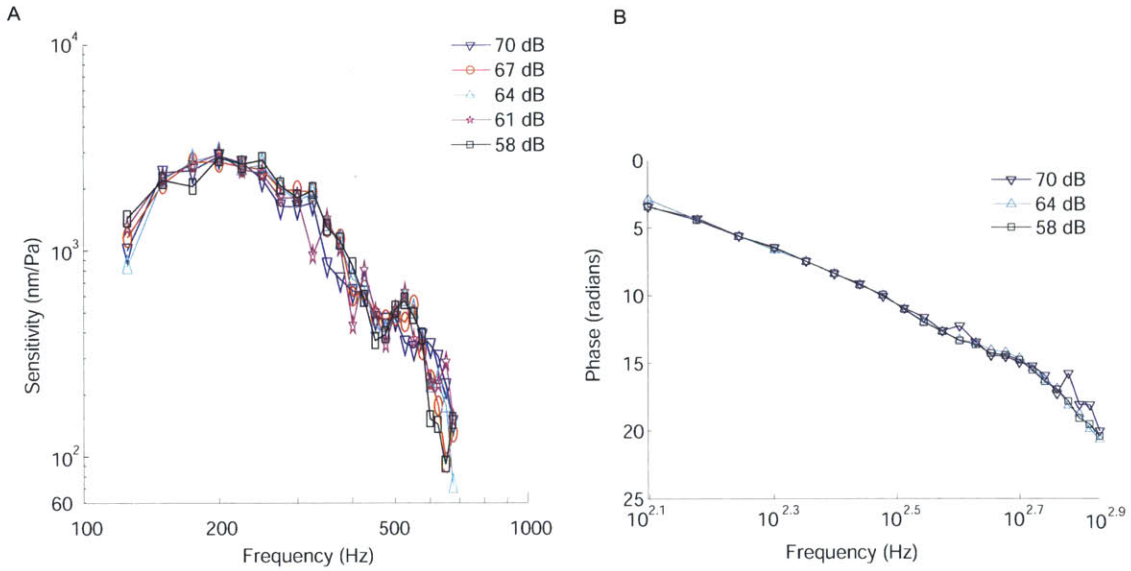

Figure 5-21: (A) Level-dependent sensitivity (motion/input sound pressure) and (B) stimulus-referenced phase as a function of frequency in the *in vivo* guinea pig (GP6756) apex (~200 Hz characteristic frequency) in response to ~70 dB equivalent sound pressure level (SPL) sinusoidal acoustic stimulation.

the resulting image exhibits a change in slope of Reissner's membrane shortly after death. Figure 5-24D-F shifts structures after death to account for the change of fluid depth traversed by the measurement beam (see discussion).

Applying the differential analysis method used previously, the white line in figure 5-25A represents the reference motion and the red arrows the reference axis. Average magnitude of axial motion along the reference line is shown in figure 5-25D, while figures 5-25B and C show the relative magnitude and phase of relative axial motion, respectively.

Figure 5-25E shows that the mean of differential motion within the OHC region is ~4.3±2.2 nm p-p compared to the mean of absolute motion of 47.9±5.19 nm p-p for a ratio of ~$\frac{1}{9}$ of differential to absolute axial OHC motion. The OHC region does not appear to be moving with a uniform differential phase (figure 5-25F).

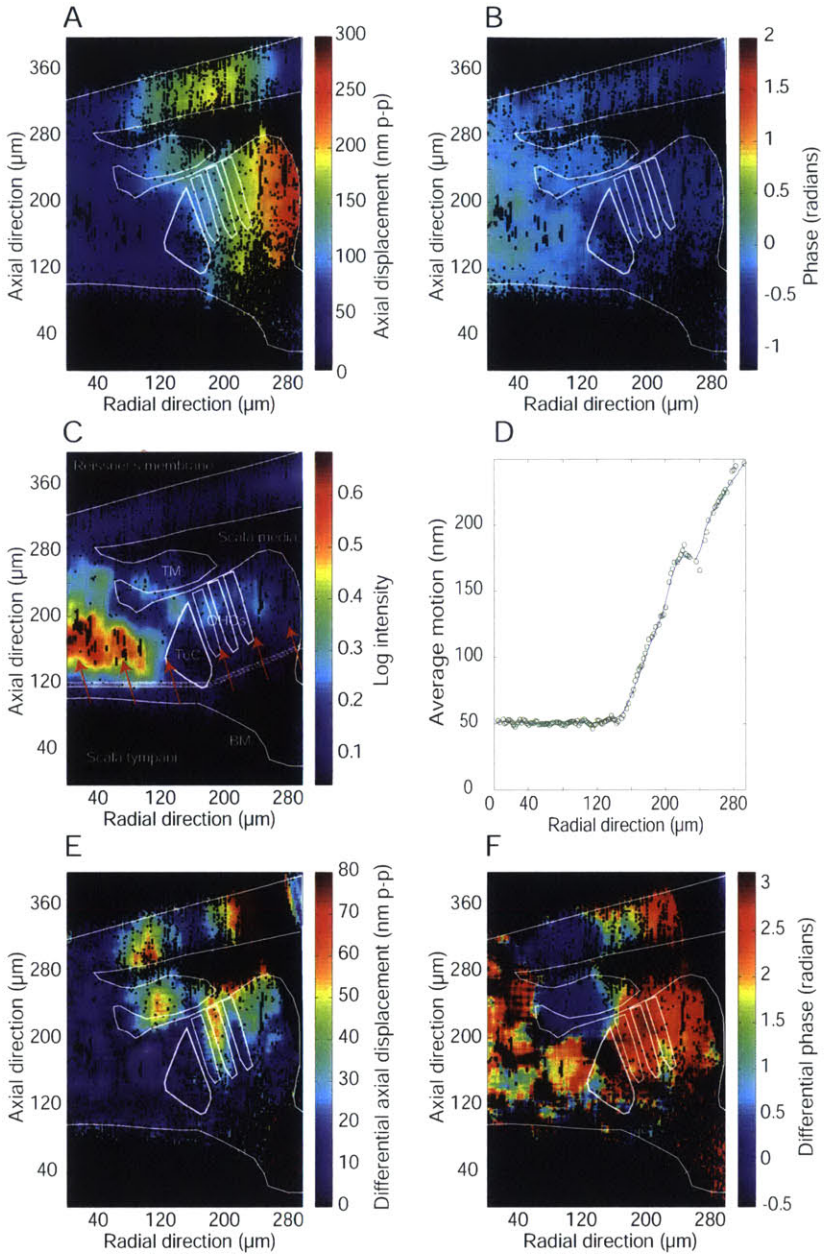

Figure 5-22: DOCT (10 ×, 0.13 NA, 2μm× 2μm resolution) (A) magnitude of axial motion map, (B) stimulus-referenced phase map, and (C) image in the apex (200 Hz characteristic frequency) of an *in vivo* guinea pig (GP6756) in response to ~70 dB SPL sinusoidal acoustic stimulation at 200 Hz. Differential complex axial motion, referenced to the average complex motion along the lower portion of the organ of Corti [white line in (C)], is found by subtracting that motion along lines that parallel the outer pillar cells (red arrows). (D) Magnitude of the complex axial motion along the reference line. The solid blue line represents the magnitude of a 6-point running complex average. (E) Magnitude of axial differential motion referenced to the lower portion of the organ of Corti [white line from (C)] with colorbar range of 0–80 nm p-p. (F) Axial differential phase referenced to the lower portion of the organ of Corti [white line from (C)]

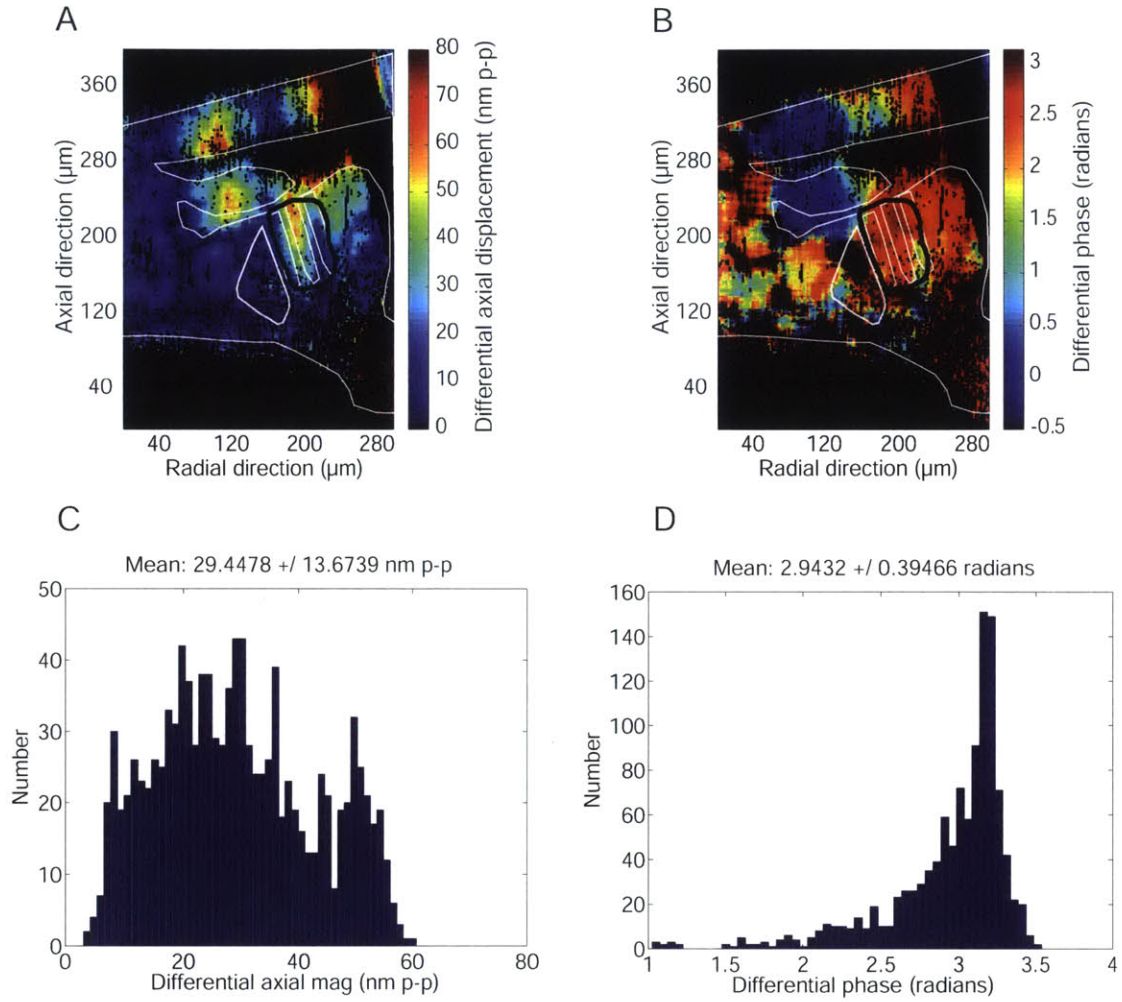

Figure 5-23: DOCT (10 ×, 0.13 NA, 2μm× 2μm resolution) measurements of an *in vivo* guinea pig (GP6756, 200 Hz characteristic frequency) in response to ~70 dB SPL sinusoidal acoustic stimulation at 200 Hz. (A) Magnitude of axial differential motion with colormap range of 0–80 nm p-p and (B) differential phase referenced to the lower portion of the organ of Corti [white line from figure 5-22(C)]. Histograms in the region of the OHCs [black outline in (A)] of (C) differential magnitude of motion and (D) differential phase.

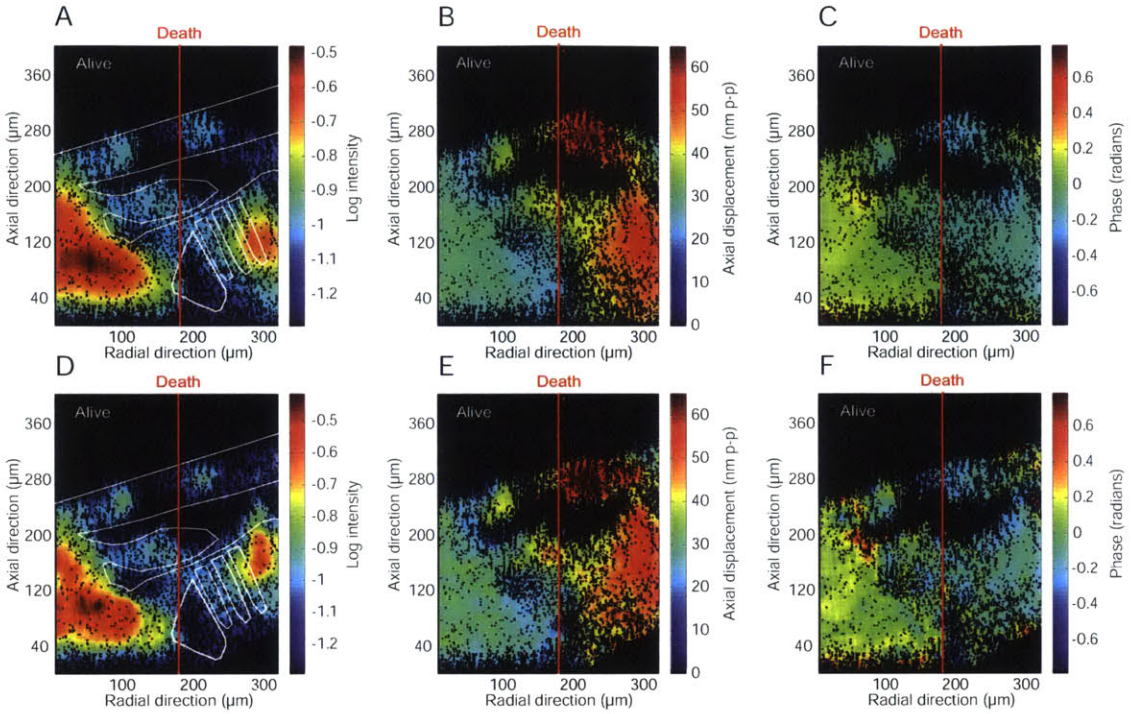

Figure 5-24: Post-mortem motion. DOCT (10 ×, 0.13 NA, 2μm× 2μm resolution) (A) Apical image, (B) magnitude of axial motion, and (C) stimulus-referenced phase map in the *in vivo* guinea pig (GP6756, ~200 Hz characteristic frequency) in response to ~61 dB equivalent sound pressure level (SPL) sinusoidal acoustic stimulation at 200 Hz. Death occurred 36 minutes into the experiment between 178 - 184 μm along the radial axis. (D) Image, (E) magnitude of axial motion, and (F) stimulus-referenced phase maps corrected for the change of fluid depth traversed by the measurement beam after death.

5.3 Discussion

Sound-induced *in vitro* and *in vivo* preparations exhibit axial motion increase as a function of radial position throughout the organ of Corti as well as a relatively constant phase (figure 5-9 & 5-17). This constant phase suggests that the organ is moving together, with the outer radial end moving with greater magnitude. This is consistent with pivoting under pressure differentials between the scalae [25]. Figure 5-19 shows that radial motion dependence and constant phase are maintained over a large frequency range. Furthermore, reducing sound pressure level reduces the amount of motion, but has no effect on phase across frequency (figure 5-20).

Reticular lamina displacements are scaled by sound pressure level to determine

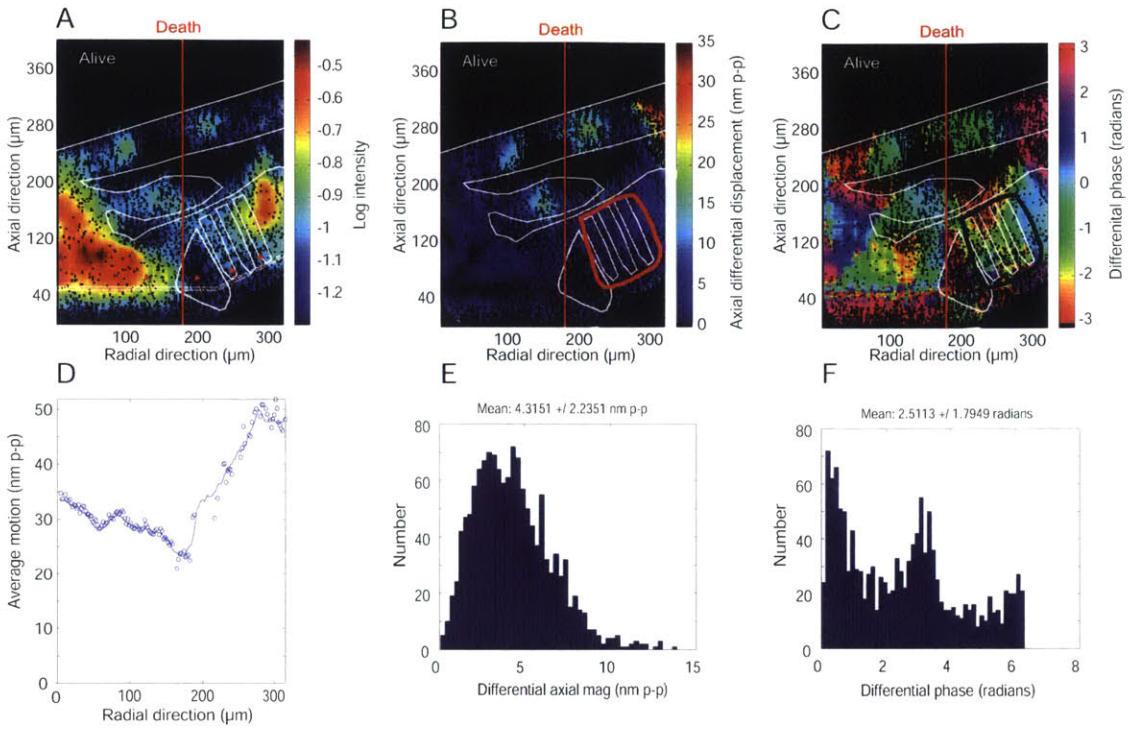

Figure 5-25: Post-mortem differential motion. DOCT (10 ×, 0.13 NA, 2μm× 2μm resolution) measurements of the *in vivo* guinea pig (GP6756, ~200 Hz characteristic frequency) in response to ~61 dB equivalent sound pressure level (SPL) sinusoidal acoustic stimulation at 200 Hz. (A) Apical image, (B) differential axial motion magnitude map and (F) differential phase map referenced to motion along white line in the direction parallel to the outer pillar cells [denoted by red arrows in (A)] corrected for the change of fluid depth traversed by the measurement beam after death. (D) Average magnitude of axial motion along the white line from (A). Histograms in the region of the OHCs [red outlines in (B) and (C)] of (E) differential magnitude of motion and (F) differential phase.

sensitivity as a function of frequency and compared to previously published [95] studies of apical guinea pig and chinchilla sensitivity curves in figure 5-26. Delivered sound pressures ranged from 58 dB to 70 dB. Although peak frequency differs as a function of study location, we find similar order of magnitude sensitivity curves to those found by Zinn et al. [121]. The shape of the sensitivity curves are similar to those of the Reissner's membrane measurements of Cooper et al. and Khanna et al. [19, 63].

Nonlinear growth of cochlear responses with sound intensity is critical for compressing the enormous dynamic range of audible sounds across low and high frequen-

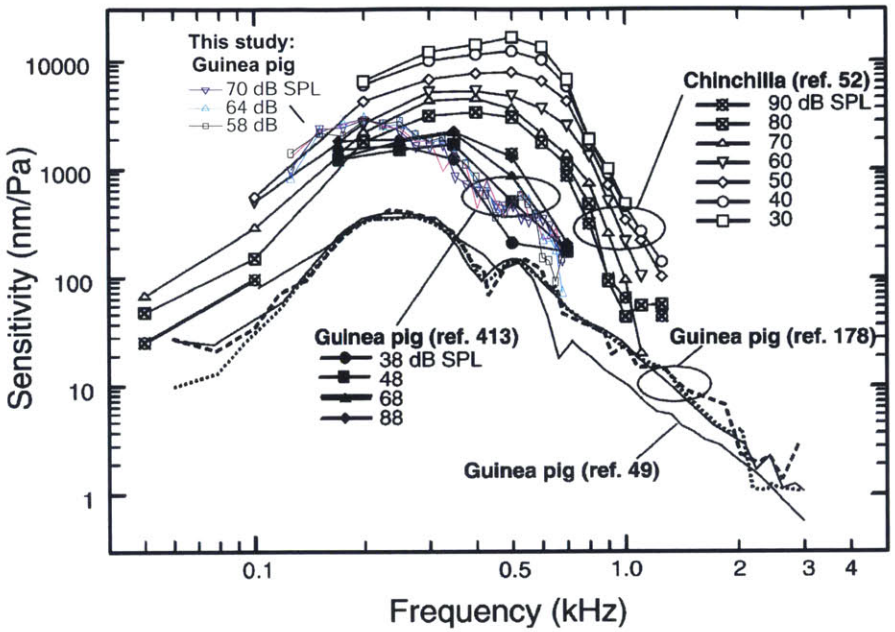

Mechanics of the Mammalian Cochlea
Luis Robles, Mario A. Ruggero
Physiological Reviews Published 1 July 2001 Vol. 81 no. 3, 1305-1352

Figure 5-26: Apical sensitivity in the *in vivo* guinea pig (GP6756, ~200 Hz characteristic frequency) in response to sinusoidal 58 – 70 dB sound pressure levels of acoustic stimulation as a function of frequency compared with previously published results. Guinea pig (ref. 413) is reference [121] measures the organ of Corti through Reissner's membrane with LDV. Guinea pig (ref. 49) is reference [19], which measures with LDV. Guinea pig (ref. 178) is [63], which measures the reticular lamina with confocal interferometry.

cies. However, sensitivity curves measured in the apical region of the *in vivo* guinea pig [95, 121, 19, 63] (figure 5-26) show very little apical non-linearity below 90 dB SPL compared to that seen in the base [64]. Sensitivity levels of the reticular lamina from this study correlate well with those measurements of the organ of Corti made by Zinn et al. [121]. The overall shape of reticular lamina sensitivity observed in this study closely resembled those of Cooper et al. and Khanna et al. [19, 63], both of whom measured apical Reissner's membrane vibration and observed a notch above the best frequency. This notch is shown by Cooper [17] to be an artifact of an unsealed cochlea. The notch above the best frequency in this study, shown in figures 5-21 and 5-26, is likely due to the optical access hole in the apical temporal bone.

Although sensitivity curves appear constant below 90 dB SPL, the apex of the

in vivo cochlea is reported to exhibit unusual non-linear behaviors above 90 dB SPL (not tested in this study) with significantly different tuning curves compared to the cochlear base. The presence of apical harmonic motion above 90 dB SPL has been previously reported by Khanna et al. and Gummer et al. [64, 62, 50].

Various models make differing predictions about the frequency dependence of the reticular lamina. In positive feedback models, somatic motility increases the motion of the reticular lamina, so that the system may be more sensitive. Khanna et al. concluded that nonlinear behavior exists in the apex and it must function under negative feedback to linearize the response of the fundamental frequency [62, 61]. Zinn et al. measured the frequency response of Hensen's cells through Reissner's membrane using LDV and concluded that the linear behavior of apical sensitivity curves below 90 dB SPL is due to an active nonlinear negative feedback damping mechanism at low intensities [121].

In order for somatic motility to contribute to cochlear amplification, it is necessary that it is effective at audio frequencies. Experiments with isolated OHCs have convincingly demonstrated the necessary bandwidth when the cells are excited electrically. However, the generation of electrical responses at audio frequencies is a topic of current controversy. It has been suggested that the membrane time constant of OHCs limits the highest frequencies of receptor potentials to kilohertz [23, 71]. Although a variety of mechanisms have been proposed to overcome this limitation [22, 86, 60] there are few direct observations of OHC length changes at audio frequencies *in vivo* [14, 120].

Table 5.1 summarizes the differential motion observed in the OHC region across the apical low frequency ($<$ 1kHz CF) preparations from this study. In the *in vitro* preparation G6039, it was observed that the OHC region was moving counterphasic to the region of the organ of Corti beneath the OHCs at $\sim\frac{1}{6}$ the magnitude. Counterphasic motions were largest near the reticular lamina. This is surprising, given that this is an *in vitro* preparation with no expected endocochlear potential. It may indicate that with Reissner's membrane intact and no hair cell blebbing observed, the cells are healthy enough (i.e. have maintained a negative resting potential) to

Animal	SPL (dB)	CF Hz	Diff. mean (nm p-p)	Abs. mean (nm p-p)	Ratio Diff.-Abs.	Diff. phase (rad)
in vitro @450Hz						
G6039	90	460	5.6±1.9	31.2±5.5	$\frac{1}{6}$	3.0±0.28
G6627	78	450	10.8±6.0	95.0±23	$\frac{1}{9}$	3.99±1.66
in vivo @200Hz						
GP6756	70	200	29.4±13.7	131.0±15	$\frac{1}{4}$	2.94±0.39
in vivo @200Hz post mortem						
GP6756	61	200	4.3±2.2	47.9±5.2	$\frac{1}{9}$	2.5±1.8

Table 5.1: Differential axial motion of the OHCs compared to absolute axial motion across preparations.

contract without the presence of an endocochlear potential.

In vitro preparation G6627 also shows differential motion, however the phase is noisy and has a wide standard deviation. This could support the previous argument as the reticular lamina in this preparation was broken. This could have allowed perilymph to come into contact with scala media and destroy the health of the outer hair cells. An alternative reason for the noisy phase could be the low resolution (4 μm$\times$ 4 μm) at which the measurements were taken.

The *in vivo* preparation GP6756 shows counterphasic motion of the OHC region relative to the region of the organ of Corti beneath the OHCs at ~$\frac{1}{4}$ the magnitude. Upon death, the differential motion drops to ~$\frac{1}{9}$ that of the absolute motion and the phase becomes noisy, which could indicate lower than measured differential displacements.

ASSR responses to low frequencies (below the lowest delivered sound pressure level) were verified after jaw removal and the opening of the bulla, but before the opening of the apical temporal bone. Due to the untimely death of the animal, no follow-up ASSR could be performed to verify cochlear health. This means that axial displacements of the cochlear partition, and the somatic motility of the OHCs measured here in the apex of the *in vivo* cochlea were not verified to have been communicating with the brain.

5.4 Summary

This chapter has demonstrated the use of DOCM and DOCT to characterize stapes-induced and sound-induced motions of cochlear structures in the apex. Sensitivities and frequency tuning are similar to previous studies and appear to be nearly constant as a function of sound pressure level over frequency. Both *in vitro* and *in vivo* preparations exhibit rotation about a pivot point in response to stapes or acoustic stimulation.

Relative motions in the *in vivo* low frequency ($<$ 1kHz) organ of Corti are shown to exhibit somatic motility on the order of ~60 nm (in response to 70 dB SPL), which reduces in relative magnitude upon death. Relative motions of the reticular lamina are counterphasic to that of the basilar membrane and tectorial membrane. This supports the argument for negative feedback of the reticular lamina within the low frequency apical region ($<$ 1kHz) [62, 121, 61], through outer hair cell contraction as the basilar membrane moves towards scala vestibuli.

Bibliography

[1] Allen, J. B. Cochlear micromechanics–a physical model of transduction. *The Journal of the Acoustical Society of America*, 68(6):1660–1670, 1980.

[2] Anderson, J. R., Chiu, D. T., Wu, H., Schueller, O. J., and Whitesides, G. M. Fabrication of microfluidic systems in poly (dimethylsiloxane). *Electrophoresis*, 21(1):27–40, 2000.

[3] Aranyosi, A. J. and Freeman, D. M. Media dependence of bleb growth in cochlear hair cells. *Assoc. Res. Otolaryngol. Abs*, 159, 1999.

[4] Aranyosi, A. J. and Freeman, D. M. Sound-induced motions of individual cochlear hair bundles. *Biophysical journal*, 87(5):3536–3546, 2004.

[5] Ashmore, J. Cochlear outer hair cell motility. *Physiological Reviews*, 88(1):173–210, 2008.

[6] Beurg, M., Fettiplace, R., Nam, J-H., and Ricci, A. J. Localization of inner hair cell mechanotransducer channels using high-speed calcium imaging. *Nature neuroscience*, 12(5):553–558, 2009.

[7] Billone, M. and Raynor, S. Transmission of radial shear forces to cochlear hair cells. *The Journal of the Acoustical Society of America*, 54(5):1143–1156, 1973.

[8] Breneman, K. D., Brownell, W. E., and Rabbitt, R. D. Hair cell bundles: flexoelectric motors of the inner ear. *PLoS One*, 4(4):e5201, 2009.

[9] Brownell, W. E., Bader, C. R., Bertrand, D., and De Ribaupierre, Y. Evoked mechanical responses of isolated cochlear hair cells. *Science*, 227:194–196, 1985.

[10] Bullock, T. H. Electroreception. *Annual review of neuroscience*, 5(1):121–170, 1982.

[11] Buschmann, M. D. and Grodzinsky, A. J. A molecular model of proteoglycan-associated electrostatic forces in cartilage mechanics. *Journal of biomechanical engineering*, 117(2):179–192, 1995.

[12] Chan, D. K. and Hudspeth, A. J. Mechanical responses of the organ of corti to acoustic and electrical stimulation in vitro. *Biophysical journal*, 89(6):4382–4395, 2005.

[13] Chen, F., Zha, D., Fridberger, A., Zheng, J., Choudhury, N., Jacques, S. L., Wang, R. K., Shi, X., and Nuttall, A. L. A differentially amplified motion in the ear for near-threshold sound detection. *Nature Neuroscience*, 14:770–775, 2011.

[14] Chen, F., Zha, D., Fridberger, A., Zheng, J., Choudhury, N., Jacques, S. L., Wang, R. K, Shi, X., and Nuttall, A. L. A differentially amplified motion in the ear for near-threshold sound detection. *Nature neuroscience*, 14(6):770–774, 2011.

[15] Choe, Y., Magnasco, M. O., and Hudspeth, A. J. A model for amplification of hair-bundle motion by cyclical binding of Ca^{2+} to mechanoelectrical-transduction channels. *Proceedings of the National Academy of Sciences*, 95(26):15321–15326, 1998.

[16] Choudhury, N., Chen, F., Matthews, S. K., Tschinkel, T., Zheng, J., Jacques, S., and Nuttall, A. L. Low coherence interferometry of the cochlear partition. *Hear Res*, 220:1–9, 2006.

[17] Cooper, N. P. Mid-band sensitivity notches in apical cochlear mechanics. *Diversity in Auditory Mechanics*, pages 298–304, 1997.

[18] Cooper, N. P. and Rhode, W. S. Basilar membrane mechanics in the hook region of cat and guinea-pig cochleae: sharp tuning and nonlinearity in the absence of baseline position shifts. *Hearing research*, 63(1):163–190, 1992.

[19] Cooper, N. P. and Rhode, W. S. Nonlinear mechanics at the apex of the guinea-pig cochlea. *Hearing Research*, 82(2):225–243, 1995.

[20] Cooper, N. P. and Rhode, W. S. Mechanical responses to two-tone distortion products in the apical and basal turns of the mammalian cochlea. *Journal of neurophysiology*, 78(1):261–270, 1997.

[21] Dallos, P., Billone, N. C., Durrant, J. D., Wang, C-Y, and Raynor, S. Cochlear inner and outer hair cells: functional differences. *Science*, 177(4046):356–358, 1972.

[22] Dallos, P. and Evans, B. N. High-frequency motility of outer hair cells and the cochlear amplifier. *Science*, 267(5206):2006–2009, 1995.

[23] Dallos, P., Evans, B. N., and Hallworth, R. Nature of the motor element in electrokinetic shape changes of cochlear outer hair cells. *Nature*, 350:155–157, 1991.

[24] Davis, C. Q. and Freeman, D. M. Using a light microscope to measure motions with nanometer accuracy. *Optical Engineering*, 37(4):1299–1304, 1998.

[25] Davis, H. Biophysics and physiology of the inner ear. *Physiol Rev*, 37(1):1–49, 1957.

[26] Edge, R. M., Evans, B. N., Pearce, M., Richter, C. P., Hu, X., and Dallos, P. Morphology of the unfixed cochlea. *Hearing Research*, 124(1):1–16, 1998.

[27] Farrahi, S., Ghaffari, R., and Freeman, D. M. Lowered pH alters decay but not speed of tectorial membrane waves. In *WHAT FIRE IS IN MINE EARS: PROGRESS IN AUDITORY BIOMECHANICS: Proceedings of the 11th International Mechanics of Hearing Workshop*, volume 1403, pages 403–404. AIP Publishing, 2011.

[28] Farris, H. E., LeBlanc, C. L., Goswami, J., and Ricci, A. J. Probing the pore of the auditory hair cell mechanotransducer channel in turtle. *The Journal of physiology*, 558(3):769–792, 2004.

[29] Fay, R. R. and Popper, A. N. *Comparative Hearing: Mammals* in *Springer Handbook of Auditory Research*. Springer-Verlag, New York, NY, 1994.

[30] Fettiplace, R. and Hackney, C. M. The sensory and motor roles of auditory hair cells. *Nature reviews neuroscience*, 7(1):19–29, 2006.

[31] Fettiplace, R. and Kim, K. X. The physiology of mechanoelectrical transduction channels in hearing. *Physiological Reviews*, 94(3):951–986, 2014.

[32] Frank, E. H. and Grodzinsky, A. J. Cartilage electromechanics–I. electrokinetic transduction and the effects of electrolyte pH and ionic strength. *Journal of Biomechanics*, 20(6):615–627, 1987.

[33] Freeman, D. M., Hattangadi, S. M., and Weiss, T. F. Osmotic responses of the isolated mouse tectorial membrane to changes in pH. *Auditory Neuroscience*, 3(4):363–375, 1997.

[34] Freeman, D. M., Masaki, K., McAllister, A. R., Wei, J. L., and Weiss, T. F. Static material properties of the tectorial membrane: a summary. *Hearing research*, 180(1):11–27, 2003.

[35] Freitas, R., Zhang, G., Albert, J. S., Evans, D. H., and Cohn, M. J. Developmental origin of shark electrosensory organs. *Evolution & development*, 8(1):74–80, 2006.

[36] Gale, J. E. and Ashmore, J. F. An intrinsic frequency limit to the cochlear amplifier. *Nature*, 389(6646):63–66, 1997.

[37] Gao, S. S., Xia, A., Yuan, T., Raphael, P. D., Shelton, R. L., Applegate, B. E., and Oghalai, J. S. Quantitative imaging of cochlear soft tissues in wild-type and hearing-impaired transgenic mice by spectral domain optical coherence tomography. *Opt Express*, 19:15415–15428, 2011.

[38] Gavara, N. and Chadwick, R. S. Collagen-based mechanical anisotropy of the tectorial membrane: implications for inter-row coupling of outer hair cell bundles. *PLoS One*, 4(3):e4877, 2009.

[39] Gavara, N., Manoussaki, D., and Chadwick, R. S. Auditory mechanics of the tectorial membrane and the cochlear spiral. *Current opinion in otolaryngology & head and neck surgery*, 19(5):382, 2011.

[40] Ghaffari, R. Electrically evoked motions of the isolated mouse tectorial membrane. Master's thesis, Massachusetts Institute of Technology, 2003.

[41] Ghaffari, R. *The functional role of the mammalian tectorial membrane in the cochlear mechanics.* PhD thesis, Massachusetts Institute of Technology, 2008.

[42] Ghaffari, R., Aranyosi, A. J., and Freeman, D. M. Longitudinally propagating traveling waves of the mammalian tectorial membrane. *Proceedings of the National Academy of Sciences*, 104(42):16510–16515, 2007.

[43] Ghaffari, R., Aranyosi, A. J., Richardson, G. P., and Freeman, D. M. Tectorial membrane travelling waves underlie abnormal hearing in Tectb mutant mice. *Nature communications*, 1:96, 2010.

[44] Ghaffari, R., Page, S. L., Farrahi, S., Sellon, J. B., and Freeman, D. M. Electrokinetic properties of the mammalian tectorial membrane. *Proceedings of the National Academy of Sciences*, 110(11):4279–4284, 2013.

[45] Grodzinsky, A. J. Electromechanical and physicochemical properties of connective tissue. *Critical reviews in biomedical engineering*, 9(2):133–199, 1982.

[46] Gueta, R., Barlam, D., Shneck, R. Z., and Rousso, I. Measurement of the mechanical properties of isolated tectorial membrane using atomic force microscopy. *Proceedings of the National Academy of Sciences*, 103(40):14790–14795, 2006.

[47] Guinan Jr., J. J. How are inner hair cells stimulated? Evidence for multiple mechanical drives. *Hearing research*, 292(1):35–50, 2012.

[48] Guinan Jr., J. J. and Cooper, N. P. Medial olivocochlear efferent inhibition of basilar-membrane responses to clicks: evidence for two modes of cochlear mechanical excitation. *The Journal of the Acoustical Society of America*, 124(2):1080–1092, 2008.

[49] Guinan Jr., J. J., Lin, T., and Cheng, H. Medial-olivocochlear-efferent inhibition of the first peak of auditory-nerve responses: Evidence for a new motion within the cochlea. *The Journal of the Acoustical Society of America*, 118(4):2421–2433, 2005.

[50] Gummer, A. W., Hemmert, W., Morioka, I., Reis, P., Reuter, G., and Zenner, H. P. Cellular motility measured in the guinea-pig cochlea. *Biophysics of hair cell sensory systems*, pages 229–239, 1993.

[51] Harrison, R. V. and Hunter-Duvar, I. M. An anatomical tour of the cochlea. In *Physiology of the Ear*, pages 159–171, New York, 1988. Raven Press.

[52] Hong, S. and Freeman, D. M. Doppler optical coherence microscopy for studies of cochlear mechanics. *Biomed Opt*, 11(5):054014, 2006.

[53] Hudspeth, A. J. Extracellular current flow and the site of transduction by vertebrate hair cells. *The Journal of Neuroscience*, 2(1):1–10, 1982.

[54] Hudspeth, A. J. The cellular basis of hearing: the biophysics of hair cells. *Science*, 230(4727):745–752, 1985.

[55] Hudspeth, A. J. How the ear's works work. *Nature*, 341(6241):397–404, 1989.

[56] Hudspeth, A. J. Making an effort to listen: mechanical amplification in the ear. *Neuron*, 88(1):530–545, 2008.

[57] Johnson, S. L., Beurg, M., Marcotti, W., and Fettiplace, R. Prestin-driven cochlear amplification is not limited by the outer hair cell membrane time constant. *Neuron*, 70(6):1143–1154, 2011.

[58] Karavitaki, K. D. and Mountain, D. C. Imaging electrically-evoked micromechanical motion within the organ of corti. *Biophys J*, 92:3294–3316, 2006.

[59] Keiler, S. and Richter, C. P. Cochlear dimensions obtained in hemicochleae of four different strains of mice: CBA/CaJ, 129/CD1, 129/SvEv and C57BL/6J. *Hearing research*, 162(1):91–104, 2001.

[60] Kennedy, H. J., Crawford, A. C., and Fettiplace, R. Force generation by mammalian hair bundles supports a role in cochlear amplification. *Nature*, 433(7028):880–883, 2005.

[61] Khanna, S. M. The response of the apical turn of cochlea modeled with a tuned amplifier with negative feedback. *Hearing Research*, 194(1):97–108, 2004.

[62] Khanna, S. M. and Hao, L. F. Nonlinearity in the apical turn of living guinea pig cochlea. *Hearing Research*, 135(1):89–104, 1999.

[63] Khanna, S. M. and Hao, L. F. Reticular lamina vibrations in the apical turn of a living guinea pig cochlea. *Hearing Research*, 132(1):15–33, 1999.

[64] Khanna, S. M., Ulfendahl, M., and Flock, A. Dependence of cellular responses on signal level. *Acta oto-laryngologica. Supplementum*, 467:195–203, 1989.

[65] Kim, Y-J, Bonassar, L. J., and Grodzinsky, A. J. The role of cartilage streaming potential, fluid flow and pressure in the stimulation of chondrocyte biosynthesis during dynamic compression. *Journal of biomechanics*, 28(9):1055–1066, 1995.

[66] Kössl, M. M. and Russell, I. J. Basilar membrane resonance in the cochlea of the mustached bat. *Proceedings of the National Academy of Sciences*, 92(1), 1995.

[67] Kronester-Frei, A. Sodium dependent shrinking properties of the tectorial membrane. *Scanning electron microscopy*, 2:943–948, 1978.

[68] Legan, P. K., Lukashkina, V. A., Goodyear, R. J., Kössl, M., Russell, I. J., and Richardson, G. P. A targeted deletion in α-tectorin reveals that the tectorial membrane is required for the gain and timing of cochlear feedback. *Neuron*, 28(1):273–285, 2000.

[69] Legan, P. K., Lukashkina, V. A., Goodyear, R. J., Lukashkin, A. N., Verhoeven, K., Van Camp, G., Russell, I. J., and Richardson, G. P. A deafness mutation isolates a second role for the tectorial membrane in hearing. *Nature neuroscience*, 8(8):1035–1042, 2005.

[70] Lin, T. and Guinan Jr., J. J. Auditory-nerve-fiber responses to high-level clicks: Interference patterns indicate that excitation is due to the combination of multiple drives. *Acoustical Society of America*, 107:2615–2630, 2000.

[71] Mammano, F. and Ashmore, J. F. Differential expression of outer hair cell potassium currents in the isolated cochlea of the guinea-pig. *The Journal of Physiology*, 496(3):639–646, 1996.

[72] Mammano, F. and Nobili, R. Biophysics of the cochlea: linear approximation. *The Journal of the Acoustical Society of America*, 93(6):3320–3332, 1993.

[73] Masaki, K., Ghaffari, R., Gu, J. W., Richardson, G. P., Freeman, D. M., and Aranyosi, A. J. Tectorial membrane material properties in TectaY 1870C/+ heterozygous mice. *Biophysical journal*, 99(10):3274–3281, 2010.

[74] Masaki, K., Weiss, T. F., and Freeman, D. M. Poroelastic bulk properties of the tectorial membrane measured with osmotic stress. *Biophysical journal*, 91(6):2356–2370, 2006.

[75] McGuirt, W. T., Prasad, S. D., Griffith, A. J., Kunst, H. P., Green, G. E., Shpargel, K. B., Runge, C., Huybrechts, C., Mueller, R. F., Lynch, E., and King, M. C. Mutations in COL11A2 cause non-syndromic hearing loss (DFNA13). *Nature genetics*, 23(4):413–419, 1999.

[76] Meaud, J. and Grosh, K. The effect of tectorial membrane and basilar membrane longitudinal coupling in cochlear mechanics. *The Journal of the Acoustical Society of America*, 127(3):1411–1421, 2010.

[77] Narayan, S. S., Temchin, A. N., Recio, A., and Ruggero, M. A. Frequency tuning of basilar membrane and auditory nerve fibers in the same cochleae. *Science*, 282(5395):1882–1884, 1998.

[78] Neely, S. T. and Kim, D. O. An active cochlear model showing sharp tuning and high sensitivity. *Hearing Research*, 9(2):123–130, 1983.

[79] Neely, S. T. and Kim, D. O. A model for active elements in cochlear biomechanics. *The journal of the acoustical society of America*, 79(5):1472–1480, 1986.

[80] Nowotny, M. and Gummer, A. W. Nanomechanics of the subtectorial space caused by electromechanics of cochlear outer hair cells. *Proc Natl Acad Sci USA*, 103(7):2120–2125, 2006.

[81] Nuttall, A., Dolan, D., and Avinash, G. Laser doppler velocimetry of basilar membrane vibration. *Hear Res*, 51:203–213, 1991.

[82] Nuttall, A. L. and Fridberger, A. Instrumentation for studies of cochlear mechanics: from von békésy forward. *Hear Res*, 293:3–11, 2012.

[83] Page, S., Ghaffari, R., and Freeman, Dennis M. Doppler optical coherence microscopy and tomography applied to inner ear mechanics. In *Mechanics of Hearing: Protein to Perception*, page 040002, Melville, NY, 2015. Karavitaki KD, Corey DP (eds). American Insitute of Physics.

[84] Popesco, P., Rajtova, V., and Horak, J. *A Colour Atlas of Anatomy of Small Laboratory Animals, Volume one: Rabbit, Guinea pig*. Wolfe publishing, London, UK, 1992.

[85] Rabbitt, R. D., Boyle, R., and Highstein, S. M. Mechanical amplification by hair cells in the semicircular canals. *Proceedings of the National Academy of Sciences*, 107(8):3864–3869, 2010.

[86] Rabbitt, R. D., Clifford, S., Breneman, K. D., Farrell, B., and Brownell, W. E. Power efficiency of outer hair cell somatic electromotility. *Comput Biol*, 5(7):e1000444, 2009.

[87] Ravicz, M. E., Olson, E. S., and Rosowski, J. J. Sound pressure distribution and power flow within the gerbil ear canal from 100 hz to 80 khz. *J Acoust Soc Am*, 122:2154–73, 2007.

[88] Recio, A., Rich, N. C., Narayan, S. S., and Ruggero, M. A. Basilar-membrane responses to clicks at the base of the chinchilla cochlea. *The Journal of the Acoustical Society of America*, 103(4):1972–1989, 1998.

[89] Ren, T. Longitudinal pattern of basilar membrane vibration in the sensitive cochlea. *Proc Natl Acad Sci USA*, 99:17101–17106, 2002.

[90] Rhode, W. S. Observations of the vibration of the basilar membrane using mossbauer technique. *Acoust Soc Am*, 49:1218–1231, 1971.

[91] Rhode, W. S. and Cooper, N. P. Nonlinear mechanics in the apical turn of the chinchilla cochlea in vivo. *Auditory Neuroscience*, 3(2), 1996.

[92] Richardson, G. P., Lukashkin, A. N., and Russell, I. J. The tectorial membrane: one slice of a complex cochlear sandwich. *Current opinion in otolaryngology & head and neck surgery*, 16(5):458, 2008.

[93] Richardson, G. P., Russell, I. J., Duance, V. C., and Bailey, A. J. Polypeptide composition of the mammalian tectorial membrane. *Hearing research*, 25(1):45–60, 1987.

[94] Richter, C. P., Emadi, G., Getnick, G., Quesnel, A., and Dallos, P. Tectorial membrane stiffness gradients. *Biophysical journal*, 93(6):2265–2276, 2007.

[95] Robles, L. and Ruggero, M. A. Mechanics of the mammalian cochlea. *Physiol Rev*, 81:1305–1352, 2001.

[96] Robles, L., Ruggero, M. A., and Rich, N. C. Two-tone distortion in the basilar membrane of the cochlea. *Nature*, 349:413–414, 1991.

[97] Robles, L., Ruggero, M. A., and Rich, N. C. Two-tone distortion on the basilar membrane of the chinchilla cochlea. *Journal of neurophysiology*, 77(5):2385–2399, 1997.

[98] Ruggero, M.A., Rich, N. C., Nola, C., Recio, A., Narayan, S. S., and Robles, L. Basilar-membrane responses to tones at the base of the chinchilla cochlea. *The Journal of the Acoustical Society of America*, 101(4):2151–2163, 1997.

[99] Russell, I. J. and Kössl, M. M. Micromechanical responses to tones in the auditory fovea of the greater mustached bat's cochlea. *Journal of neurophysiology*, 82(2):676–686, 1999.

[100] Russell, I. J., Legan, P. K., Lukashkina, V. A., Lukashkin, A. N., Goodyear, R. J., and Richardson, G. P. Sharpened cochlear tuning in a mouse with a genetically modified tectorial membrane. *Nature neuroscience*, 10(2):215–223, 2007.

[101] Russell, I. J. and Nilsen, K.E. The location of the cochlear amplifier: spatial representation of a single tone on the guinea pig basilar membrane. *Proceedings of the National Academy of Sciences*, 94(6):2660–2664, 1997.

[102] Scherer, M. P. and Gummer, A. W. Vibration pattern of the organ of corti up to 50 kHz: evidence for resonant electromechanical force. *Proceedings of the National Academy of Sciences of the United States of America*, 101(51):17652–17657, 2004.

[103] Schwander, M., Kachar, B., and Müller, U. The cell biology of hearing. *Journal of Cell Biology*, 190:9–20, 2010.

[104] Sellick, P. M., Patuzzi, R. B., and Johnstone, B. M. Measurement of basilar membrane motion in the guinea pig using the mössbauer technique. *J Acoust Soc Am*, 72(1):131–141, 1982.

[105] Shah, D. M., Freeman, D. M., and Weiss, T. F. The osmotic response of the isolated, unfixed mouse tectorial membrane to isosmotic solutions: effect of Na^+, K^+, and Ca^{2+} concentration. *Hearing research*, 87(1):187–207, 1995.

[106] Steel, K. P. Donnan equilibrium in the tectorial membrane. *Hearing research*, 12(2):265–272, 1983.

[107] Suzuki, N., Asamura, K., Kikuchi, Y., Takumi, Y., Abe, S., Imamura, Y., Hayashi, T., Aszodi, A., Fässler, R., and Usami, S. Type IX collagen knock-out mouse shows progressive hearing loss. *Neuroscience research*, 51(3):293–298, 2005.

[108] Szalda, K. K. and Burkard, R. R. The effects of nembutal anesthesia on the auditory steady-state response (assr) from the inferior colliculus and auditory cortex of the chinchilla. *Hear Res*, 203:32–44, 2005.

[109] Teudt, I. U. and Richter, C. P. The hemicochlea preparation of the guinea pig and other mammalian cochleae. *Journal of neuroscience methods*, 162(1):187–197, 2007.

[110] Thalmann, I. Collagen of accessory structures of organ of corti. *Connective tissue research*, 29(3):191–201, 1993.

[111] Thalmann, I., Machiki, K., Calabro, A., Hascall, V. C., and Thalmann, R. Uronic acid-containing glycosaminoglycans and keratan sulfate are present in the tectorial membrane of the inner ear: functional implications. *Archives of biochemistry and biophysics*, 307(2):391–396, 1993.

[112] Thalmann, I., Thallinger, G., Comegys, T. H., Crouch, E. C., Barrett, N., and Thalmann, R. Composition and supramolecular organization of the tectorial membrane. *The Laryngoscope*, 97(3):357–367, 1987.

[113] Timoshenko, S. P. and Goodier, J. N. Theory of elasticity. *International Journal of Bulk Solids Storage in Silos*, 1(4), 2014.

[114] von Békésy, G. *Experiments in Hearing*. McGraw Hill, New York, NY, 1960.

[115] Weiss, T. F. and Freeman, D. M. Equilibrium behavior of an isotropic polyelectrolyte gel model of the tectorial membrane: effect of ph. *Hearing research*, 111(1):55–64, 1997.

[116] Weiss, T. F. and Freeman, D. M. Equilibrium behavior of an isotropic polyelectrolyte gel model of the tectorial membrane: The role of fixed charges. *Aud. Neurosci*, 3:351–361, 1997.

[117] Wong, B. J., deBoer, J. F., Park, B. H., Chen, Z., and Nelson, J. S. Optical coherence tomography of the rat cochlea. *Journal of Biomedical Optics*, 5:367–370, 2000.

[118] Wong, B. J., Zhao, Y., Yamaguchi, M., Nassif, N., Chen, Z., and deBoer, J. F. Imaging the internal structure of the rat cochlea using optical coherence tomography at 0.827 micron and 1.3 micron. *Otalaryngol Head Neck Surg*, 130:458, 2004.

[119] Xue, S., Mountain, D. C., and Hubbard, A. E. Electrically evoked basilar membrane motion. *The Journal of the Acoustical Society of America*, 97(5):3030–3041, 1995.

[120] Zha, D., Chen, F., Ramamoorthy, S., Fridberger, A., Choudhury, N., Jacques, S. L., Wang, R. K., and Nuttall, A. L. In vivo outer hair cell length changes expose the active process in the cochlea. *PLoS One*, 7(4):e32757, 2012.

[121] Zinn, C., Maier, H., Zenner, H. P., and Gummer, A. W. Evidence for active, nonlinear, negative feedback in the vibration response of the apical region of the in-vivo guinea-pig cochlea. *Hearing Research*, 142(1):159–183, 2000.

[122] Zwislocki, J. J. Tectorial membrane: a possible sharpening effect on the frequency analysis in the cochlea. *Acta oto-laryngologica*, 87(3-6):267–269, 1979.

[123] Zwislocki, J. J. Five decades of research on cochlear mechanics. *The Journal of the Acoustical Society of America*, 67(5):1679–1685, 1980.